Rotational quantum friction in superfluids: Radiation from object rotating in superfluid vacuum

A. Calogeracos
Low Temperature Laboratory, Helsinki University of Technology, P. O. Box 2200, FIN-02015, Finland;
NCA Research Associates, PO Box 61147, Maroussi 151 01, Athens, Greece

G. E. Volovik
Low Temperature Laboratory, Helsinki University of Technology, P. O. Box 2200, FIN-02015, Finland;
L. D. Landau Institute of Theoretical Physics, 117940 Moscow, Russia

(Submitted 20 January 1999)
Pis'ma Zh. Éksp. Teor. Fiz. **69**, No. 4, 257–262 (25 February 1999)

The friction experienced by a body rotating in a superfluid liquid at $T=0$ is discussed. The effect is analogous to the amplification of electromagnetic radiation and spontaneous emission by a body or black hole rotating in the quantum vacuum, first discussed by Zel'dovich and Starobinsky. The friction is caused by the interaction of the part of the liquid which is rigidly connected with the rotating body and thus represents a comoving detector, with the ''Minkowski'' superfluid vacuum outside the body. The emission process is the quantum tunneling of quasiparticles from the detector to the ergoregion, where the energy of quasiparticles is negative in the rotating frame. This quantum rotational friction caused by the emission of quasiparticles is estimated for phonons and rotons in superfluid ^{4}He and for Bogoliubov fermions in superfluid ^{3}He. © *1999 American Institute of Physics.* [S0021-3640(99)00104-8]

PACS numbers: 03.65.−w, 67.40.−w

INTRODUCTION

A body moving in vacuum with a linear acceleration a is believed to radiate a thermal spectrum with the Unruh temperature $T_U=\hbar a/2\pi c$ (Ref. 1). The comoving observer sees the vacuum as a thermal bath with $T=T_U$, so that the matter of the body gets heated to T_U (see references cited in Ref. 2). Linear motion at constant proper acceleration (hyperbolic motion) leads to a velocity arbitrarily close to the speed of light. On the other hand uniform circular motion features constant centripetal acceleration while being free of the above mentioned pathology (see the latest references in Refs. 3–5). The latter motion is stationary in the rotating frame, which is thus a convenient frame for study of the radiation and thermalization effects for uniformly rotating body.

Zel'dovich[6] was the first to predict that a rotating body (say, a dielectric cylinder) amplifies those electromagnetic modes which satisfy the condition

 © 1999 American Institute of Physics

$$\omega - L\Omega < 0. \tag{1}$$

Here ω is the frequency of the mode, L is its azimuthal quantum number, and Ω is the angular velocity of the rotating cylinder. This amplification of the incoming radiation is referred to as superradiance.[7] Another aspect of this phenomenon is that, on account of quantum effects, a cylinder rotating in the quantum vacuum spontaneously emits the electromagnetic modes satisfying Eq. (1).[6] The same occurs for any rotating body, including a rotating black hole,[8] if the above condition is satisfied.

Unlike the case of a linearly accelerated body, the radiation by a rotating body does not look thermal. Also, the rotating observer does not see the Minkowski vacuum as a thermal bath. This means that the matter of the body, though excited by interaction with the quantum fluctuations of the Minkowski vacuum, does not necessarily acquire an intrinsic temperature depending only on the angular velocity of rotation. Moreover the vacuum of the rotating frame is not well defined because of the ergoregion, which exists at a distance $r_e = c/\Omega$ from the axis of rotation.

The problems related to the response of a quantum system in its ground state to rotation,[3] such as radiation by an object rotating in vacuum[6,9,8,7] and the vacuum instability caused by the existence of the ergoregion,[10] etc., can be simulated in superfluids, where the superfluid ground state plays the part of the quantum vacuum. We discuss the quantum friction due to spontaneous emission of phonons and rotons in superfluid ^{4}He and Bogoliubov fermions in superfluid ^{3}He.

ROTATING FRAME

Let us consider a cylinder of radius R rotating with angular velocity Ω in an (infinite) superfluid liquid. In bosonic superfluids the quasiparticles are phonons and rotons; in fermi superfluids these are the Bogoliubov fermions. The phonons are ''relativistic'' quasiparticles: Their energy spectrum is $E(p) = cp + \mathbf{p}\cdot\mathbf{v}_s$, where c is the speed of sound and $\mathbf{v}_s$ is the superfluid velocity (the velocity of the superfluid vacuum); this phonon dispersion is represented by the Lorentzian metric (the so-called acoustic metric):[11,12]

$$g^{\mu\nu}p_\mu p_\nu = 0, \quad g^{00} = -1, \quad g^{0i} = v_s^i, \quad g^{ik} = c^2\delta^{ik} - v_s^i v_s^k. \tag{2}$$

When the body rotates, the energy of quasiparticles is not well defined in the laboratory frame because of the time dependence of the potential, caused by the rotation of the body. But it is defined in the rotating frame, where the potential is stationary. Hence it is simpler to work in the rotating frame. If the body is rotating surrounded by a stationary superfluid, i.e., if $\mathbf{v}_s = 0$ in the laboratory frame, then in the rotating frame one has $\mathbf{v}_s = -\mathbf{\Omega}\times\mathbf{r}$. Substituting this $\mathbf{v}_s$ in Eq. (2), we get the interval $ds^2 = g_{\mu\nu}dx^\mu dx^\nu$, which determines the propagation of phonons in the rotating frame:

$$ds^2 = -(c^2 - \Omega^2 r^2)dt^2 - 2\Omega r^2 d\phi dt + dz^2 + r^2 d\phi^2 + dr^2. \tag{3}$$

The azimuthal motion of the quasiparticles in the rotating frame can be quantized in terms of the angular momentum L, while the radial motion can be treated in the quasiclassical approximation. Then the energy spectrum of the phonons in the rotating frame is

$$E = c\sqrt{\frac{L^2}{r^2} + p_z^2 + p_r^2} - \Omega L. \tag{4}$$

ERGOREGION IN SUPERFLUIDS

The radius $r_e = c/\Omega$, where $g_{00} = 0$, marks the position of the ergoplane. In the ergoregion, i.e., at $r > r_e = c/\Omega$, the quasiparticle energy in Eq. (4) can become negative for any rotation velocity and $\Omega L > 0$. We assume that the angular velocity of rotation Ω is small enough that the linear velocity on the surface of the cylinder ΩR is less than $v_L = c$ (the Landau velocity for nucleation of phonons). Thus phonons cannot be nucleated at the surface of the cylinder. However in the ergoplane the velocity $v_s = \Omega r$ in the rotating frame reaches c, so that quasiparticles can be created in the ergoregion $r > r_e$.

The process of creation is, however, determined by the dynamics, i.e., by the interaction with the rotating body; there is no radiation in the absence of the body. If $\Omega R \ll v_L = c$ one has $r_e \gg R$, i.e., the ergoregion is situated far from the cylinder; thus the interaction of the phonon state in the ergoregion with the rotating body is small. This results in a small emission rate and thus in a small value of the quantum friction, as will be discussed below.

Let us now consider other excitations: rotons and Bogoliubov fermions. Their spectra in the rotating frame are

$$E(p) = \Delta + \frac{(p - p_0)^2}{2m_0} - \Omega L, \tag{5}$$

$$E(p) = \sqrt{\Delta^2 + v_F^2 (p - p_0)^2} - \Omega L. \tag{6}$$

Here p_0 marks the roton minimum in superfluid ^{4}He and the Fermi momentum in a Fermi liquid, while Δ is either a roton gap or the gap in superfluid ^{3}He-B. The Landau critical velocity for the emission of these quasiparticles is $v_L = \min(E(p)/p) \sim \Delta/p_0$. In ^{4}He the Landau velocity for emission of rotons is smaller than that for the emission of phonons, $v_L = c$. That is why the ergoplane for rotons, $r_e = v_L/\Omega$, is closer to the cylinder. However, for the rotating body the emission of the rotons is exponentially suppressed due to the large value of the allowed angular momentum for emitted rotons: the Zel'dovich condition (1) for the roton spectrum is satisfied only for $L > \Delta/\Omega \gg 1$ (see Fig. 1b).

ROTATING DETECTOR

Let us consider a system which is rigidly connected to the rotating body and thus comprises a comoving detector. In superfluids the simplest model for such a detector consists of the layer near the surface of the cylinder within which the superfluid velocity follows the rotation of the cylinder, i.e., $\mathbf{v}_s = \mathbf{\Omega} \times \mathbf{r}$ in the laboratory frame, and thus $\mathbf{v}_s = 0$ in the rotating frame. This means that, as distinct from the superfluid outside the cylinder, in such a layer the quasiparticle spectrum has no $-\Omega L$ shift of the energy levels.

Since in the detector matter, i.e., in the surface layer, the vorticity in the laboratory frame is nonzero, $\nabla \times \mathbf{v}_s = 2\mathbf{\Omega} \neq 0$, this layer either contains vortices or is represented by normal (nonsuperfluid) liquid which is rigidly rotating with the body. Actually the whole rotating cylinder can be represented by a rotating normal liquid. The equilibrium state of a rotating normal liquid viewed in the rotating frame is the same as that of a stationary normal liquid viewed in the laboratory frame.

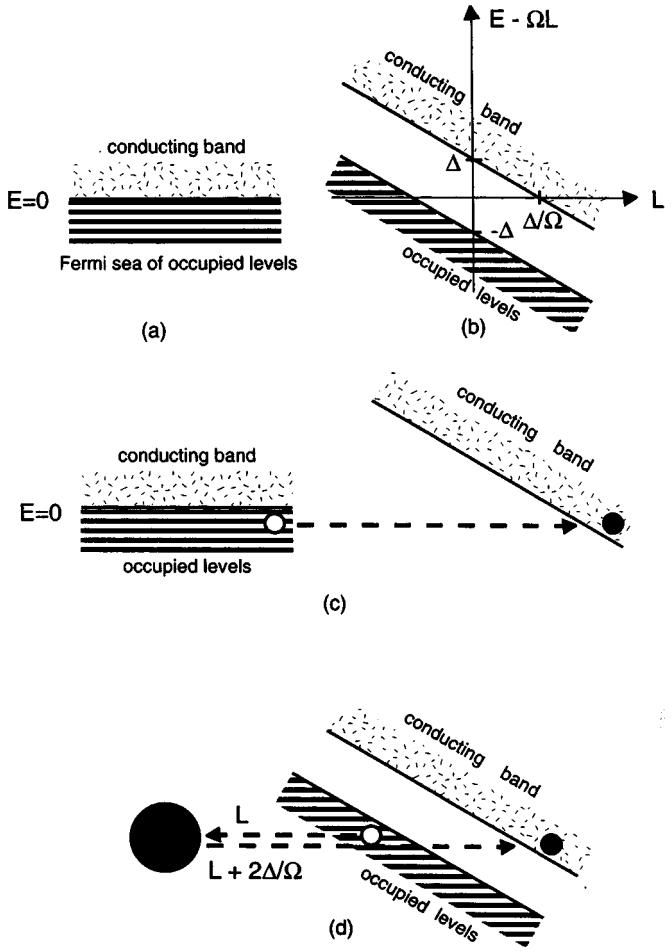

FIG. 1. a — Vacuum of the Fermi liquid within the rotating body at $r<R$. This vacuum is rotating together with the body and thus plays the role of the comoving detector. b — ''Minkowski'' vacuum of superfluid outside the rotating body as viewed in rotating frame. In the ergoregion, i.e., at $r>r_e=v_L/\Omega$, where v_L is the Landau critical velocity, the conduction band crosses the zero energy level. c — Tunneling of particles from the vacuum of the detector matter to the ''Minkowski'' vacuum in the ergoregion produces radiation from rotating body and excitation of the comoving detector. d — Transition between the states in the ''Minkowski'' vacuum due to interaction with the rotating detector.

The rotating cylinder can also be represented by a cluster of quantized vortices. The average superfluid velocity within the cluster is $\langle \mathbf{v}_s \rangle = 0$ in the rotating frame. Thus within the cluster the superfluid is in the ground state in the rotating frame, while outside the cluster the superfluid is in the ground state in the laboratory frame. Such rigidly rotating clusters of vortices have been investigated experimentally in superfluid ^{3}He (see, e.g.,, Ref. 13).

Thus we can discuss the complete system as consisting of two parts, each in its own ground state (see Figs. 1a and 1b for the case of Fermi liquid): (1) The detector matter in its ground state as seen in the rotating frame; (2) the superfluid outside the cylinder in its

ground state (the ''Minkowski'' vacuum) in the laboratory frame. The radiation of fermions by the rotating cylinder is described by the rotating observer as a tunneling process (Fig. 1c): fermions tunnel from the occupied negative energy levels in the detector to the unoccupied negative energy state in the ergoregion. The same can be considered as the spontaneous nucleation of pairs: a particle is nucleated in the ergoregion and its partner hole is nucleated in the comoving detector. This process causes the radiation from the rotating body and also the excitation of the detector. From the point of view of the Minkowski (stationary) observer this is described as the excitation of the superfluid system by time-dependent perturbations.

RADIATION OF PHONONS TO THE ERGOREGION

For the Bose case the radiation of phonons can be also considered as a process in which a particle in the normal Bose liquid in the detector tunnels to the scattering state at the ergoplane, where also the energy is $E=0$. In the quasiclassical approximation the tunneling probability is e^{-2S}, where at $p_z=0$:

$$S=\mathrm{Im}\int dr\, p_r = L\int_R^{r_e} dr\, \sqrt{\frac{1}{r^2}-\frac{1}{r_e^2}} \approx L\ln\frac{r_e}{R}. \tag{7}$$

Thus all the particles with $L>0$ are radiated, but the radiation probability decreases at higher L. If the linear velocity at the surface is much less than the Landau critical velocity $\Omega R \ll c$, the probability of radiation of phonons with energy (frequency) $\omega=\Omega L$ is

$$w\propto e^{-2S}=\left(\frac{R}{r_e}\right)^{2L}=\left(\frac{\Omega R}{c}\right)^{2L}=\left(\frac{\omega R}{cL}\right)^{2L}, \quad \Omega R\ll c. \tag{8}$$

If c is replaced by the speed of light, Eq. (8) is proportional to the superradiant amplification of electromagnetic waves by a rotating dielectric cylinder, derived by Zel'dovich.[7,9]

The number of phonons of frequency $\omega=\Omega L$ emitted per unit time can be estimated as $\dot{N}=We^{-2S}$, where W is the attempt frequency $\sim\hbar/ma^2$ multiplied by the number of localized modes $\sim RZ/a^2$, where Z is the height of the cylinder and a is the thickness of the normal fluid layer, of the order of the interatomic spacing. Since each phonon carries angular momentum L, a cylinder rotating in superfluid vacuum (at $T=0$) loses angular momentum, which means the presence of quantum rotational friction.

RADIATION OF ROTONS AND BOGOLIUBOV QUASIPARTICLES

The minimal L value of radiated quasiparticles having a gap Δ is determined by this gap: $L_{\min}=\Delta/\Omega p_0=v_L/\Omega$, where $v_L=\Delta/p_0$ is the Landau critical velocity. Since the tunneling rate decreases exponentially with L, only the lowest possible L must be considered. In this case the tunneling trajectory with $E=0$ is determined by the equation $p=p_0$ both for rotons and Bogoliubov quasiparticles. For $p_z=0$ the classical tunneling trajectory is thus given by $p_r=i\sqrt{|p_0^2-L^2/r^2|}$. This gives for the tunneling exponent e^{-2S} the equation

$$S=\mathrm{Im}\int dr\, p_r = L\int_R^{r_e} dr\, \sqrt{\frac{1}{r^2}-\frac{1}{r_e^2}} \approx L\ln\frac{r_e}{R}. \tag{9}$$

Here the position of the ergoplane is $r_e = L/p_0 = v_L/\Omega$. Since the rotational velocity Ω is always much smaller than the gap, L is very large. That is why the radiation of rotons and Bogoliubov quasiparticles with a gap is exponentially suppressed.

FRICTION DUE TO TRANSITIONS IN ''MINKOWSKI VACUUM''

Radiation can occur without excitation of the detector vacuum, via direct interaction of the particles in the Minkowski vacuum with the rotating body. In the rotating frame the states in the occupied band and in the conduction band have the same energy, if they have opposite momenta L. Then a transition between the two levels is energetically allowed and will occur if the Hamiltonian has a nonzero matrix element between the states L and $-L$. The necessary interaction is provided by any breaking of the axial symmetry of the rotating body, e.g., by roughness on the surface (thus the interaction is localized at $r \sim R$). A wire moving along a circular orbit is another practical example. In the case of a rotating vortex cluster the axial symmetry is always broken.

In the quasiclassical approximation the process of radiation is as follows (see Fig. 1d). A particle from the occupied band in the ergoregion tunnels to the surface of the rotating body, where after interaction with a nonaxisymmetric disturbance it changes its angular momentum. After that it tunnels back to the ergoregion to the conduction band. In this process both a particle and a hole are produced in the Minkowski vacuum, and as a result the tunneling exponent is twice as large as in Eqs.(8) and (9).

DISCUSSION

The rotational friction experienced by a body rotating in superfluid vacuum at $T=0$ is caused by the spontaneous quantum emission of quasiparticles from the rotating object to the ''Minkowski'' vacuum in the ergoregion. The emission is not thermal and depends on the details of the interaction of the radiation with the rotating body. In the quasiclassical approximation it is mainly determined by the tunneling exponent, which can be approximately characterized by an effective temperature $T_{\rm eff} \sim \hbar\Omega(2/\ln(v_L/\Omega R))$. The vacuum friction of the rotating body can be observed only if the effective temperature exceeds the temperature of the bulk superfluid, $T_{\rm eff} > T$. For a body rotating with $\Omega = 10^3$ rad/s, T must be below 10^{-8} K. However, a high rotational velocity can be obtained in a system of two like vortices rotating around their center of mass with $\Omega = \kappa/4\pi R^2$ (κ is the circulation around each vortex, and R is the radius of the circular orbit).

The process discussed in the paper occurs only if there is an ergoplane in the rotating frame. For a superfluid confined within the external cylinder of radius $R_{\rm ext}$, this process occurs at high enough rotation velocity, $r_e(\Omega) = v_L/\Omega < R_{\rm ext}$, when the ergoplane is within the superfluid. On the instability of the ergoregion in quantum vacuum towards emission, see, e.g., Ref. 10.

If $r_e(\Omega) > R_{\rm ext}$ and the ergoregion is not present, then the interaction between the coaxial cylinders via the vacuum fluctuations becomes the main mechanism for dissipation. This causes the dynamic Casimir forces between the walls moving laterally (see review[14]). As in Ref. 14 the nonideality of the cylinders is the necessary condition for quantum friction.

The case of a rotating body is not the only case in which the ergoregion is important in superfluids. The ergoregion also appears for linearly moving textures when the speed of the order-parameter texture exceeds the local ''speed of light.''[15]

One of us (A.C.) wishes to thank the Low Temperature Laboratory of Helsinki University of Technology for the hospitality and EU Training and Mobility of Researchers Program Contract # ERBFMGECT980122 for its support.

[1] W. G. Unruh, Phys. Rev. D **14**, 870 (1976).
[2] J. Audretsch and R. Müller, Phys. Rev. A **50**, 1755 (1994).
[3] P. C. W. Davies, T. Dray, and C. A. Manogue, Phys. Rev. D **53**, 4382 (1996).
[4] J. M. Leinaas, http://xxx.lanl.gov/abs/hep-th/9804179.
[5] W. G. Unruh, http://xxx.lanl.gov/abs/hep-th/9804158.
[6] Ya. B. Zel'dovich, JETP Lett. **14**, 180, (1971).
[7] J. D. Bekenstein and M. Schiffer, Phys. Rev. D **58**, 064014 (1998).
[8] A. A. Starobinskii, Zh. Éksp. Teor. Fiz. **64**, 48 (1973) [Sov. Phys. JETP **37**, 28 (1973)].
[9] Ya. B. Zel'dovich, Zh. Éksp. Teor. Fiz. **62**, 2076 (1971) [Sov. Phys. JETP **35**, 1085 (1971)].
[10] G. Kang, Phys. Rev. D **55**, 7563 (1997).
[11] W. G. Unruh, Phys. Rev. Lett. **46**, 1351 (1981).
[12] M. Visser, Class. Quantum Grav. **15**, 1767 (1998).
[13] Ü. Parts, V. M. H. Ruutu, J. H. Koivuniemi *et al.*, Europhys. Lett. **31**, 449 (1995).
[14] M. Kardar and R. Golestanian, http://xxx.lanl.gov/abs/cond- mat/9711071.
[15] T. A. Jacobson and G. E. Volovik, Phys. Rev. D **58**, 064021 (1998); JETP Lett. **68**, 874 (1998).

Published in English in the original Russian journal. Edited by Steve Torstveit.

Azimuthal modulation of the event rate of cosmic-ray extensive air showers by the geomagnetic field

A. A. Ivanov,[1)] V. P. Egorova, V. A. Kolosov, A. D. Krasil'nikov, M. I. Pravdin, and I. E. Sleptsov

Institute of Cosmophysical Research and Aeronomy, Siberian Branch of the Russian Academy of Sciences, 677891 Yakutsk, Russia

(Submitted 29 December 1998)
Pis'ma Zh. Éksp. Teor. Fiz. **69**, No. 4, 263–267 (25 February 1999)

The effect of the Earth's magnetic field on the azimuthal distribution of the number of extensive air showers is measured using data obtained from many years of observations at the Yakutsk array. A uniform azimuthal distribution of the event rates of these showers is rejected at a 10^{-14} significance level. The amplitude of the harmonic of the distribution depends on the zenith angle as $A_1 \approx 0.2 \sin^2\theta$ and is virtually independent of the primary-particle energy, while the phase coincides with the magnetic meridian. From the magnitude of the measured effect a correction factor for the particle density is determined which depends on the geomagnetic parameter of the shower. © *1999 American Institute of Physics.* [S0021-3640(99)00204-2]

PACS numbers: 96.40.Pq

The trajectories of charged particles of an extensive air shower (EAS) developing in the atmosphere from primary cosmic-ray particles are curved in the Earth's magnetic field. As a result, the spatial distribution of the particles is broadened in a plane perpendicular to the shower axis, in the direction of the Lorentz force. The observation of this effect[1] at the Yakutsk EAS array in strongly inclined showers with zenith angles $\theta > 60°$ showed the presence of a pronounced asymmetry of the spatial distribution function (SDF) of the particles due to the deflection of the muons; this asymmetry is proportional to the geomagnetic parameter of the shower, which is determined by the angle between the shower axis and the field vector: $g = \sin\chi/\cos^2\theta$, where $\chi = \cos^{-1}(\cos\theta\cos\theta_H + \sin\theta\sin\theta_H\cos(\alpha+20))$, where $\theta_H = 14°$, and α is the azimuthal angle. The influence of the geomagnetic field on the spatial distribution of the particles has been confirmed by observations[2] for showers with zenith angles $20° < \theta < 60°$. The results of calculations of the expected effect in the GZK model was used to analyze the shower with the highest energy detected at the Yakutsk EAS array, $E_0 > 10^{20}$ eV (Ref. 3), and in Ref. 4 it was shown that showers from ultrahigh energy γ rays should exhibit north–south asymmetry. But for the latter effect there is a threshold with respect to the energy of the primary γ rays, $E_\gamma > 3 \times 10^{19}$ eV.

In the present letter we call attention to the fact that since the asymmetry of the SDF depends on the relative arrangement of the field vector and the particle velocity, by selecting showers with the same energy and zenith angles we should obtain modulation

 © 1999 American Institute of Physics

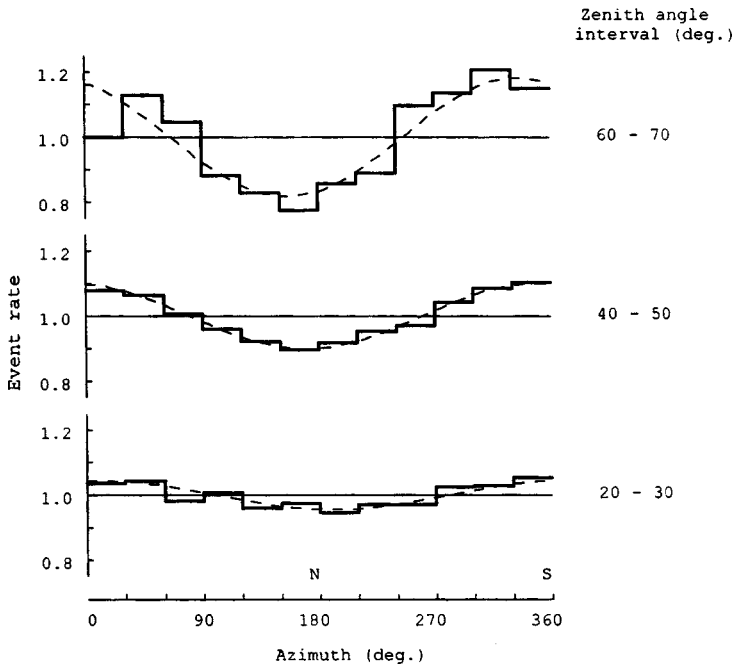

FIG. 1. Normalized numbers of EAS events in the zenith-angle intervals (shown on the right side) as a function of the azimuthal angle for showers with $E_0 > 5\times10^{16}$ eV. The dashed line shows the function $1+A_1\cos(\alpha-\alpha_1)$. The amplitude and phase of the first harmonic as functions of θ and E_0 are presented in Figs. 2 and 3.

of the EAS event rate with respect to the azimuthal angle because of the different broadening of the SDF, which changes the observed energy of the primary particles and the associated primary cosmic-ray flux intensity.

Figure 1 shows the distribution of the number of EAS events with energy exceeding 5×10^{16} eV measured at the Yakutsk array in the period 1974–1995 in the zenith-angle intervals 20–30°, 40–50°, and 60–70°. The numbers of EAS events in the θ intervals that were used in the analysis are presented in Table I.

The dependence of the amplitude and phase of the first three harmonics of the distribution on the zenith angle and energy of the primary EAS particle is shown in Figs. 2 and 3. The amplitudes of the second and third harmonics correspond to the expected value for a uniform distribution of azimuthal angles, shown by the dashed line, for the measured number of showers in each interval. The short-dash lines show the error corridor for the expected amplitudes. The amplitude of the first harmonic is substantially different from zero in the zenith-angle intervals Nos. 3–7 from Table I. In these intervals

TABLE I. Number n of EAS events in θ intervals.

No.	1	2	3	4	5	6	7	8
θ, deg	0–10	10–20	20–30	30–40	40–50	50–60	60–70	70–80
n	25924	69114	83226	66649	37575	16384	6609	1749

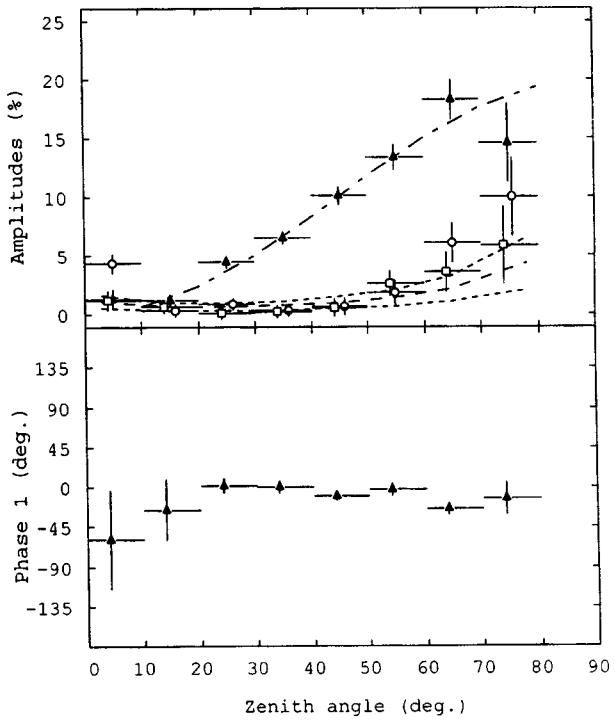

FIG. 2. Amplitudes of the first three harmonics and phase of the first harmonic as functions of the zenith angle. The vertical bars show the statistical error and the horizontal bars show the angular intervals. Notations: ▲ — first, ○ — second, □ — third harmonics. The dot-and-dash line shows the function $0.2\sin^2\theta$. The dashed curve shows the expected amplitudes of the harmonics for a uniform azimuthal distribution; the dotted curves show the variance of the expected amplitudes (1σ).

a uniform distribution over the azimuthal angle can be rejected with a probability of error of less than 10^{-14}, based on the probability that for the uniform distribution the amplitude of the first harmonic is greater than A_1: $P(>A_1)=\exp(-n\cdot A_1^2/4)$. The phase of the first harmonic coincides with the magnetic meridian at Yakutsk. As a result of the small slope of the magnetic field vector in the region of the array ($\theta_H=14°$), the first harmonic of the distribution of azimuthal angles predominates for $20<\theta<70°$. The picture could be different for other arrays. For example, for the Tibet array, where the direction of the field is inclined by 45° relative to the vertical, the first and second harmonics should be pronounced for angles $\theta>50°$, while for the Chakaltaĭ array ($\theta_H=88°$) the second harmonic will predominate.

To determine the effect of the array geometry on the magnitude of the modulation, we constructed the azimuthal-angle distribution of the event rate in the sample of showers detected using detectors arranged in a circle 1.5 km in radius around the center of the array (azimuthally symmetric part of the setup). We found that the amplitude and phase of the first harmonic in the sample are different from the corresponding values for the initial distribution by amounts that are certainly smaller than the statistical errors. We therefore assumed the azimuthal modulation to be independent of the array geometry.

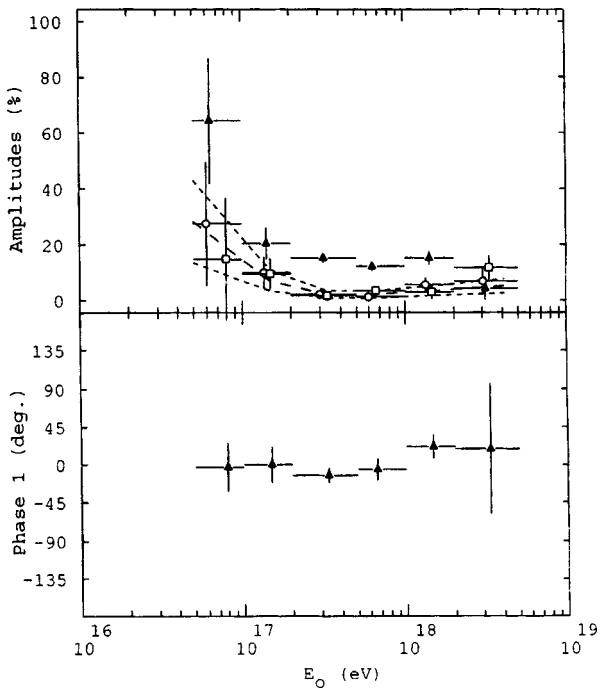

FIG. 3. Amplitudes of the first three harmonics and phase of the first harmonic versus the energy of the primary particle of an EAS. The notation is the same as in Fig. 2.

The showers at the Yakutsk array are analyzed by adjusting the parameters of an axisymmetric function used to fit the charged-particle density in the detectors. The particle density ρ_{300} found 300 m from the shower axis according to this function is converted to the energy of the primary particle of the EAS. Let us see how ρ_{300} varies as a result of the geomagnetic scattering of the particles for an SDF of the form $\rho_r = cr^{-\eta}$, where r is the distance from the shower axis in a plane perpendicular to the EAS axis. The positive- and negative-particle density functions shift relative to the shower axis by a certain distance

$$\rho_r^g = c[((r\cos\varphi + d)^2 + r^2\sin^2\varphi)^{-\eta/2} + ((r\cos\varphi - d)^2 + r^2\sin^2\varphi)^{-\eta/2}]/2,$$

where d is the displacement of the charges and $\varphi \subset (0° - 360°)$.

For $d \ll r$ we obtain, averaging over a circle of radius $r = 300$ m, $\rho_{300}^g \approx \rho_{300}^{g=0}(1 + (\eta \cdot d_{300}/2)^2)$. Here $\eta \approx 3$,[1] and $d_{300} = d/300$ m. On average the particle densities in the detectors are higher than the density expected with no geomagnetic field (i.e., $g = 0$). For showers arriving from the north the observed particle densities in the detectors are higher than in the ''southern'' showers of equal energy and the same zenith angle.

When we select showers with the same densities ρ_{300}, the primary-particle energy is lower for showers arriving from the north. This decreases the corresponding EAS event rate, as is evident from Fig. 1, since in the range $10^{16} < E_0 < 10^{18}$ eV the number of

TABLE II. Correction factors for the measured density ρ_{300}.

	θ, deg	20	30	40	50	60
$\rho_{300}^{g=0}/\rho_{300}^{g}$	northern showers	0.94	0.92	0.88	0.82	0.72
	southern showers	0.99	0.96	0.93	0.87	0.78

showers detected at the Yakutsk array decreases with energy. The amplitude of the first harmonic is determined by the relative change in the density ρ_{300} measured for southern and northern showers:

$$2A_1 = \Delta J/J = \gamma(\Delta\rho_{300}/\rho_{300}),$$

where J is the EAS event rate and $\gamma = \ln J/\ln \rho_{300}$. The zenith-angle dependence of the amplitude A_1 is described well by the function $0.2\sin^2\theta$ (Fig. 2), but the variation of γ with increasing zenith angle has the effect that $\Delta\rho_{300}/\rho_{300}$ cannot be described by such a simple function. It is known[5] that the maximum zenith angle separating showers in which the electron–photon and muon components of the shower predominate at sea level for $r = 300$ m is about 50°. Figure 2 shows that the geomagnetic effect in an EAS is observed in both of these regions.

The asymmetry of the SDF due to the geomagnetic field is determined by the displacement of the charges. Let ξ be the ratio of the longest to the shortest distance corresponding to a fixed particle density $\rho_{300}^{g=0}$. Then

$$\xi \approx 1 + \frac{\eta+2}{2} d_{300}^2 \approx 1 + \Delta\rho_{300}/\rho_{300}$$

for $\eta = 3$. Therefore the measurements of the ''ovalness'' of the SDF can be used to estimate the variation of ρ_{300} due to the geomagnetic field. In Ref. 1 it is shown that the coefficient of linear proportionality between the degree of asymmetry of the SDF and the geomagnetic parameter of strongly inclined showers is $d\xi/dg = 0.1 \pm 0.04$. Using this value in the entire region of zenith angles, we obtain the correction factors to the density ρ_{300} that depend on the zenith angle θ (see Table II).

As one can see from Fig. 3, the amplitude of the first harmonic is virtually independent of E_0 in the energy range containing an adequate number of events. Therefore the energy dependence of the factors can be neglected.

At the Yakutsk array ρ_{300} is converted to E_0 using a method that relates ρ_{300} in inclined and vertical showers via a line of equal intensity in spectra at different zenith angles. Since these intensities correspond to the same primary-particle energy of an EAS and since geomagnetic corrections can be neglected in vertical showers, in estimating E_0 its zenith-angle dependence is taken into account correctly but the variation of the energy with the azimuth is averaged. This produces a small systematic error, proportional to A_1, in the estimate of the primary-particle energy. The absorption range of ρ_{300} determined according to the lines of equal intensity is overestimated by $\approx 10\%$ relative to the value for $g = 0$.

The exponent of the EAS spectrum for ρ_{300} (ρ_{600} for showers recorded by the ''Grandmaster,'' with 1 km between the detectors) increases when geomagnetic correc-

tions are introduced. This is because the fraction of inclined showers detected by the array increases with ρ_{300}. Thus for showers with zenith angles less than 60° and energies of 10^{18}, 3×10^{18}, and 10^{19} eV the change in the exponent in the power-law spectrum of the EAS is 0.01, 0.07, and 0.24 and the relative intensity change $\Delta J/J$ is 0.16, 0.19, and 0.28, respectively.

This work was supported by the Russian Ministry of Science (Program for Support of Unique Devices) and the Russian Fund for Fundamental Research (Grant No. 98-07-90315).

[1)]e-mail: a.a.ivanov@sci.yakutia.ru

---

[1] M. N. D'yakonov, T. A. Egorov, N. N. Efimov *et al.*, *Extremely High-Energy Cosmic Rays* [in Russian], Nauka, Novosibirsk, 1991.
[2] T. A. Egorov, B. N. Afanasiev, M. N. Dyakonov *et al.*, in *Proceedings of the International Workshop on Techniques for the Study of EHECR*, Tokyo, 1993, p. 35.
[3] E. E. Antonov, A. V. Glushkov, L. G. Dedenko *et al.*, JETP Lett. **68**, 185 (1998).
[4] S. Karakula and W. Bednarek, in *24th International Conference on Cosmic Rays*, Rome, 1995, Vol. 1, p. 266; K. Kasahar, in *Proceedings of the International Symposium on EHECR: Astrophysics and Future Observatories*, Tokyo, 1996, p. 221.
[5] A. A. Ivanov, Yad. Fiz. **51**, 1820 (1990) [Sov. J. Nucl. Phys. **51**, 1147 (1990)].

Translated by M. E. Alferieff

Diffractive *S* and *D* wave vector mesons in deep inelastic scattering

I. P. Ivanov
IKP(Theorie), KFA Jülich, D-52428 Jülich, Germany;
Novosibirsk University, 630090 Novosibirsk, Russia

N. N. Nikolaev
IKP(Theorie), KFA Jülich, D-52428 Jülich, Germany;
L. D. Landau Institute of Theoretical Physics, Russian Academy of Sciences,
117334 Moscow, Russia

(Submitted 13 January 1999)
Pis'ma Zh. Éksp. Teor. Fiz. **69**, No. 4, 268–273 (25 February 1998)

Helicity amplitudes for diffractive leptoproduction of the *S* and *D* wave states of vector mesons are derived. A dramatically different spin dependence for production of the *S* and *D* wave vector mesons is predicted. It is found that $R=\sigma_L/\sigma_T$ is very small and that the higher twist effects in the production of longitudinally polarized *D* wave vector mesons are abnormally large. © *1999 American Institute of Physics.* [S0021-3640(99)00304-7]

PACS numbers: 13.60.Le, 13.88.+e

Diffractive vector meson production $\gamma^*+p\to V+p'$ in deep inelastic scattering (DIS) at small $x=(Q^2+m_V^2)/(W^2+Q^2)$ is a testing ground of ideas on the QCD pomeron exchange and light-cone wave function (LCWF) of vector mesons (Refs. 1–5; for a recent review see Ref. 6; for the kinematics see Fig. 1; $Q^2=-q^2$ and $W^2=(p+q)^2$ are standard DIS variables). The ground state vector mesons, $V=\rho^0$, $\omega^0,\varphi^0,J/\Psi,\Upsilon$ are usually supposed to be the *S* wave spin-triplet $q\bar{q}$ states. However, all the previous theoretical calculations have used the $Vq\bar{q}$ vertex $\phi_V V_\mu \bar{q}\Gamma_\mu q$ with the simplest choice $\Gamma_\mu=\gamma_\mu$, which corresponds to a certain mixture of the *S* and *D* wave states, and there has been no discussion of the impact of the *D* wave admixture in the literature (here V_μ is the vector meson polarization vector and ϕ_V is the vertex function, which is related to the vector meson LCWF as specified below).

We report here a derivation of helicity amplitudes for diffractive production of pure *S* and *D* wave $q\bar{q}$ systems for small to moderate momentum transfer $\mathbf{\Delta}$ within the diffraction cone. Understanding production of *D* wave states is a topical issue for several reasons. First, the *D* wave admixture may affect predictions for the ratio $R=\sigma_L/\sigma_T$, in which there is a persistent departure of the theory from experiment. To this end we recall that the nonperturbative long-range pion exchange between light quarks and antiquarks[7] is a natural source of S–D mixing in the ground-state ρ^0 and ω^0 mesons. Second, different spin properties of *S* and *D* wave production may facilitate the as yet unresolved

 © 1999 American Institute of Physics

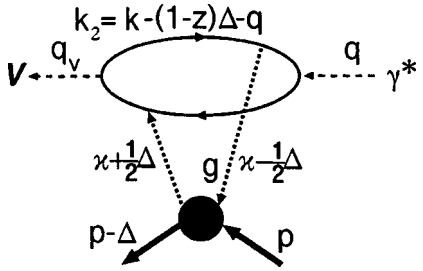

FIG. 1. One of the four Feynman diagrams for the vector meson production $\gamma^* p \to V p'$ via QCD two-gluon pomeron exchange.

D wave versus $2S$ wave assignment of the $\rho'(1480)$ and $\rho'(1700)$ mesons and the $\omega'(1420)$ and $\omega'(1600)$ mesons.

In our analysis we rely heavily upon the derivation[8] of the amplitudes of the s-channel helicity-conserving (SCHC) and nonconserving (SCHNC) transitions, albeit in a slightly different notation. We predict a dramatically different spin dependence for production of the S and D wave states, especially the Q^2 dependence of $R=\sigma_L/\sigma_T$ which derives from the anomalously large higher twist effects in the SCHC amplitude for production of longitudinally polarized vector mesons. Our technique can be readily generalized to higher excited states, 3^- etc., leptoproduction of which is interesting for the fact that they cannot be formed in e^+e^- annihilation.

A typical leading $\log(1/x)$ (LL$(1/x)$) pQCD diagram for vector meson production is shown in Fig. 1. We use the standard Sudakov expansion of all the momenta in the two light-cone vectors

$$p'=p-q\frac{p^2}{s}, \quad q'=q+p'\frac{Q^2}{s}$$

such that $q'^2=p'^2=0$ and $s=2p'\cdot q'$, and the two-dimensional transverse component: $k=zq'+yp'+k_\perp, \kappa=\alpha q'+\beta p'+\kappa_\perp, \Delta=\gamma p'+\delta q'+\Delta_\perp$ (with the exception of $\mathbf{r}$ which is a three-dimensional vector, see below, hereafter $\mathbf{k},\mathbf{\Delta},\ldots$ always stand for two-dimensional vectors $k_\perp,\Delta_\perp$ etc.). The diffractive helicity amplitudes take the form

$$A^{S,D}_{\lambda_V\lambda_\gamma}(x,Q^2,\mathbf{\Delta})=is\frac{C_F N_c c_V\sqrt{4\pi\alpha_{em}}}{2\pi^2}\int_0^1\frac{dz}{z(1-z)}\int d^2\mathbf{k}\psi_{S,D}(z,\mathbf{k})$$
$$\times\int\frac{d^2\boldsymbol{\kappa}}{\kappa^4}\alpha_S(\max\{\kappa^2,\mathbf{k}^2+\overline{Q}^2\})I^{S,D}_{\lambda_V\lambda_\gamma}(\gamma^*\to V)\Bigg(1$$
$$+i\frac{\pi}{2}\frac{\partial}{\partial\log x}\Bigg)\mathcal{F}(x,\boldsymbol{\kappa},\mathbf{\Delta}), \qquad (1)$$

where λ_V,λ_γ stand for helicities, m is the quark mass, $C_F=(N_c^2-1)/2N_c$ is the Casimir operator, $N_c=3$ is the number of colors, $c_V=1/\sqrt{2},1/3\sqrt{2},1/3,2/3$ for the $\rho^0,\omega^0,\phi^0,J/\Psi$ mesons, α_{em} is the fine structure constant, α_S is the strong coupling, and $\overline{Q}^2=m^2$

$+z(1-z)Q^2$ is the relevant hard scale. To the LL($1/x$) the lower blob is related to the unintegrated gluon density matrix $\mathcal{F}(x,\kappa,\mathbf{\Delta})$ (Refs. 5,9,10). For small $\mathbf{\Delta}$ within the diffraction cone

$$\mathcal{F}(x,\kappa,\mathbf{\Delta})=\frac{\partial G(x,\kappa^2)}{\partial\log\kappa^2}\exp\left(-\frac{1}{2}B_{3\mathbb{P}}\mathbf{\Delta}^2\right), \tag{2}$$

where $\partial G/\partial\log\kappa^2$ is the conventional unintegrated gluon structure function and, modulo to a slow Regge growth, the diffraction cone $B_{3\mathbb{P}}\sim 6\,\mathrm{GeV}^{-2}$ (Ref. 5).

In the light-cone formalism[11] one first computes the production of an on-mass shell $q\bar{q}$ pair of invariant mass M and total momentum q_M. This amplitude is projected onto the state $(q\bar{q})_J$ of total angular momentum $J=1$ using the running longitudinal and the usual transverse polarization vectors

$$V_L=\frac{1}{M}\left(q'+\frac{\mathbf{\Delta}^2-M^2}{s}p'+\Delta_\perp\right),\quad V_T=V_\perp+\frac{2(\mathbf{V}_\perp\cdot\mathbf{\Delta})}{s}(p'-q'), \tag{3}$$

such that $(V_TV_L)=(V_Tq_M)=(V_Lq_M)=0$. Then the resulting upper blob $I(\gamma^*\to V)$ is contracted with the radial LCWF of the $q\bar{q}$ Fock state of the vector meson,

$$\psi_{S,D}(z,\mathbf{k})=\psi_{S,D}(\mathbf{r}^2)=\frac{\phi_{S,D}(\mathbf{r}^2)}{M^2-m_V^2}. \tag{4}$$

Here $r=1/2(k_2-k_1)$, which in the rest frame is the relative 3-momentum in the $q\bar{q}$ pair, $r=(0,\mathbf{r})=(0,\mathbf{k},k_z)$, $r^2=-\mathbf{r}^2$, and

$$M^2=4(m^2+\mathbf{r}^2)=\frac{m^2+\mathbf{k}^2}{z(1-z)}.$$

To conform to this procedure, all the occurrences of the vector meson mass m_V in $I_{\lambda_V\lambda_\gamma}$ of Ref. 8 must be replaced by M.

A useful normalization of the radial LCWF's $\psi_{S,D}(\mathbf{r}^2)$ is provided by the $V\to e^+e^-$ decay constant, $\langle 0|J^{em}_\mu|V\rangle=fc_V\sqrt{4\pi\alpha_{em}}V_\mu$:

$$f_S=\frac{N_c}{(2\pi)^3}\int d^3\mathbf{r}\frac{8}{3}(M+m)\psi_S(\mathbf{r}^2),\quad f_D=\frac{N_c}{(2\pi)^3}\int d^3\mathbf{r}\frac{32}{3}\frac{\mathbf{r}^4}{M+2m}\psi_D(\mathbf{r}^2). \tag{5}$$

The nice observation is that we need not go again through all the calculations of helicity amplitudes. Indeed, the spinor vertices $\Gamma^{S,D}_\mu$ for the pure S and D wave states can be readily obtained from the simplest $\Gamma_\mu=\gamma_\mu$ used in Ref. 8. Following Ref. 11, it can be easily shown that

$$\Gamma^S_\mu=\gamma_\mu-\frac{2r_\mu}{M+2m}=\mathcal{S}_{\mu\nu}\gamma_\nu;\quad \mathcal{S}_{\mu\nu}=g_{\mu\nu}-\frac{2r_\mu r_\nu}{m(M+2m)}. \tag{6}$$

Here we have made use of $r^\mu\gamma_\mu=m$ and $(q_M\cdot r)=0$. Once the S wave is constructed, the spinor structure for a D wave state can be readily obtained by contracting the S wave vertex with $3r_\mu r_\nu+g_{\mu\nu}\mathbf{r}^2$, with the result

$$\Gamma^D_\mu = \mathbf{r}^2\gamma_\mu + (M+m)r_\mu = \mathcal{D}_{\mu\nu}\gamma_\nu; \quad \mathcal{D}_{\mu\nu} = \mathbf{r}^2 g_{\mu\nu} + \frac{M+m}{m} r_\mu r_\nu . \tag{7}$$

Consequently, the answers for either S or D wave production amplitudes can be immediately obtained from the expressions given in Ref. 8 by substitutions $V^*_\mu \to V^*_\nu \mathcal{S}_{\nu\mu}$, $V^*_\mu \to V^*_\nu \mathcal{D}_{\nu\mu}$ for S and D wave states respectively.

In terms of diffractive amplitudes $\mathbf{\Phi}_1$ and $\mathbf{\Phi}_2$ defined in Ref. 8, we find for S wave vector mesons (here T stands for the transverse polarization)

$$I^S_{0L} = -4QMz^2(1-z)^2\Phi_2\left[1 + \frac{(1-2z)^2 m}{2z(1-z)(M+2m)}\right],$$

$$I^S_{TT} = \left\{(\mathbf{V}^*\cdot\mathbf{e})[m^2\Phi_2 + (\mathbf{k}\cdot\mathbf{\Phi}_1)] + (1-2z)^2(\mathbf{V}^*\cdot\mathbf{k})(\mathbf{e}\cdot\mathbf{\Phi}_1)\frac{M}{M+2m} - (\mathbf{e}\cdot\mathbf{k})\right.$$
$$\left.\times(\mathbf{V}^*\cdot\mathbf{\Phi}_1) + \frac{2m}{M+2m}(\mathbf{V}^*\cdot\mathbf{k})(\mathbf{e}\cdot\mathbf{k})\Phi_2\right\},$$

$$I^S_{0T} = -2z(1-z)(2z-1)M(\mathbf{e}\cdot\mathbf{\Phi}_1)\left[1 + \frac{(1-2z)^2 m}{2z(1-z)(M+2m)}\right] + \frac{Mm}{M+2m}(2z-1)$$
$$\times(\mathbf{e}\cdot\mathbf{k})\mathbf{\Phi}_2,$$

$$I^S_{TL} = 2Qz(1-z)(2z-1)(\mathbf{V}^*\cdot\mathbf{k})\mathbf{\Phi}_2\frac{M}{M+2m}. \tag{8}$$

Because the difference between Γ^S_μ and γ_μ is a relativistic correction, the results for the S wave vector mesons differ from those found in Ref. 8 only by a small relativistic corrections $\propto \mathbf{r}^2/M^2$. The exceptional case is suppression of I^S_{TL} by factor $M/(2m+M) \sim 0.5$.

We skip the twist expansion for S wave amplitudes, which can easily be done following Ref. 8, and proceed to the much more interesting case of D wave mesons, for which

$$I^D_{0L} = -QMz(1-z)\left(\mathbf{k}^2 - \frac{4m}{M}k_z^2\right)\mathbf{\Phi}_2,$$

$$I^D_{TT} = \{(\mathbf{V}^*\cdot\mathbf{e})\mathbf{r}^2[m^2\mathbf{\Phi}_2 + (\mathbf{k}\cdot\mathbf{\Phi}_1)] + (1-2z)^2(\mathbf{r}^2+m^2+Mm)(\mathbf{V}^*\cdot\mathbf{k})(\mathbf{e}\cdot\mathbf{\Phi}_1) - \mathbf{r}^2$$
$$\times(\mathbf{e}\cdot\mathbf{k})(\mathbf{V}^*\cdot\mathbf{\Phi}_1) - m(M+m)(\mathbf{V}^*\cdot\mathbf{k})(\mathbf{e}\cdot\mathbf{k})\mathbf{\Phi}_2\},$$

$$I^D_{0T} = -\frac{2z-1}{2}M\left\{(\mathbf{e}\cdot\mathbf{\Phi}_1)\left(\mathbf{k}^2 - \frac{4m}{M}k_z^2\right) + m(M+m)(\mathbf{e}\cdot\mathbf{k})\mathbf{\Phi}_2\right\},$$

$$I^D_{TL} = 2Qz(1-z)(2z-1)(\mathbf{V}^*\cdot\mathbf{k})(\mathbf{r}^2+m^2+Mm)\mathbf{\Phi}_2. \tag{9}$$

The novel features of these amplitudes are best seen in the twist expansion in inverse powers of the hard scale $\overline{Q}^2$. As it was noted in Ref. 8, in all cases but the double helicity flip the dominant twist amplitudes come from the leading $\log\overline{Q}^2$ (LL$\overline{Q}^2$) region of $\mathbf{k}^2 \sim R_V^{-2}, \mathbf{\Delta}^2 \ll \boldsymbol{\kappa}^2 \ll \overline{Q}^2$. A closer inspection of our $I^D_{\lambda_V\lambda_\gamma}$ shows that the seemingly leading

interference with the dominant S wave component in the photon always appears in the quadrupole combination $2k_z^2-\mathbf{k}^2$. Since the integration over the quark loop can be cast in the form $d^3\mathbf{r}$, such quadrupole combinations vanish after angular integration. As a result, abnormally large higher twist contributions $\propto M^2/(M^2+Q^2)$, with large numerical factors, come into play and significantly modify the Q^2 dependence of the amplitudes for production of longitudinally polarized vector mesons:

$$I^D_{0L}=-\frac{Q}{M}\,\frac{32\mathbf{r}^4}{15(M^2+Q^2)^2}\left(1-8\frac{M^2}{M^2+Q^2}\right)\boldsymbol{\kappa}^2, \tag{10}$$

$$I^D_{\pm\pm}=(\mathbf{V}^*\cdot\mathbf{e})\,\frac{32\mathbf{r}^4}{15(M^2+Q^2)^2}\left(15+4\frac{M^2}{M^2+Q^2}\right)\boldsymbol{\kappa}^2, \tag{11}$$

$$I^D_{\pm L}=-\frac{32\mathbf{r}^4}{15(M^2+Q^2)^2}\,\frac{24Q(\mathbf{V}^*\cdot\boldsymbol{\Delta})}{M^2+Q^2}\,\boldsymbol{\kappa}^2, \tag{12}$$

$$I^D_{L\pm}=\frac{32\mathbf{r}^4}{15(M^2+Q^2)^2}\,\frac{8(\mathbf{e}\cdot\boldsymbol{\Delta})}{M}\left(1+3\frac{M^2}{M^2+Q^2}\right)\boldsymbol{\kappa}^2, \tag{13}$$

$$I^D_{\pm\mp}=(\mathbf{V}^*\cdot\boldsymbol{\Delta})(\mathbf{e}\cdot\boldsymbol{\Delta})\,\frac{32\mathbf{r}^4}{15(M^2+Q^2)^2}\left(1-\frac{96}{7}\,\frac{\boldsymbol{\kappa}^2\mathbf{r}^2}{M^2(M^2+Q^2)}\right). \tag{14}$$

In close similarity to the S wave case,[8] the leading twist double-helicity flip amplitude is dominated by soft gluon exchange, and the $\mathrm{LL}\overline{Q^2}$ component is of higher twist.

In order to emphasize striking difference between the D wave and S wave state amplitudes, we focus on nonrelativistic heavy quarkonia, where $M^2\approx m_V^2$, although all the qualitative results hold for light vector mesons, too. For purposes of illustration, we evaluate the ratios of helicity amplitudes, $\rho_{D/S}=f_SA^D/f_DA^S$, for the the harmonic oscillator wave functions:

$$\rho_{0L}(D/S)=\frac{1}{5}\left(1-8\frac{m_V^2}{Q^2+m_V^2}\right),$$

$$\rho_{\pm\pm}(D/S)=3\left(1+\frac{4}{15}\,\frac{m_V^2}{Q^2+m_V^2}\right),$$

$$\rho_{0\pm}(D/S)=-\frac{1}{5}(m_Va_S)^2\left(1+3\frac{m_V^2}{Q^2+m_V^2}\right),$$

$$\rho_{\pm L}(D/S)=\frac{3}{40}(m_Va_S)^4. \tag{15}$$

First, A_{0L} changes the sign at $Q^2\sim 7m_V^2$. The ratio $R^D=\sigma_L/\sigma_T$ has thus a nonmonotonic Q^2 behavior and $R^D\ll R^S$. Furthermore, $R^D\lesssim 1$ in a broad range of $Q^2\lesssim 225m_V^2$. Whereas in heavy quarkonia the S–D mixing is arguably weak,[12] in light ρ^0,ω^0 even a relatively weak S–D mixing could have a substantial impact on R. Second, all the D

wave amplitudes, SCHC and SCHNC alike, with exception of the higher twist component of double-helicity flip, are proportional to $\mathbf{r}^4$ and, in view of Eq. (5), to the decay constant f_D. In contrast to that, in the S wave case the spin-flip amplitudes for heavy quarkonia are suppressed by nonrelativistic Fermi motion.[8] The relevant suppression parameter is $\sim 1/(a_S m_V)^2$, where a_S is the radius of the $1S$ state. For this reason, for D wave states the SCHNC effects are much stronger. For instance, for charmonium $(m_V a_S)^2 \approx 27$ (see Ref. 12).

To summarize, we have found dramatically different spin properties of diffractive leptoproduction of the S and D wave states of vector mesons. We predict a very small $R^D = \sigma_L/\sigma_T$ and a very strong breaking of the s-channel helicity conservation in the production of D wave states. Higher twist effects in the production of longitudinally polarized D wave vector mesons are found to be abnormally large. Consequently, the distinct spin properties of D wave vector mesons in diffractive DIS offer an interesting way to discern S and D wave meson states, which are indistinguishable at e^+e^- colliders.

The fruitful discussions with B. G. Zakharov and V. R. Zoller are gratefully acknowledged. I.P.I. thanks Prof. J. Speth for hospitality at the Institut für Kernphysik, Forschungszentrum Jülich. The work of I.P.I. has been partly supported by the Russian Fund for Fundamental Research.

[1] N. N. Nikolaev, Comments Nucl. Part. Phys. **21**, 41 (1992); B. Z. Kopeliovich, J. Nemchik, N. N. Nikolaev, and B. G. Zakharov, Phys. Lett. B **309**, 179 (1993); B. Z. Kopeliovich, J. Nemchik, N. N. Nikolaev, and B. G. Zakharov, Phys. Lett. B **324**, 469 (1994).
[2] J. Nemchik, N. N. Nikolaev, and B. G. Zakharov, Phys. Lett. B **341**, 228 (1994).
[3] D. Yu. Ivanov, Phys. Rev. D **53**, 3564 (1996); I. F. Ginzburg and D. Yu. Ivanov, Phys. Rev. D **54**, 5523 (1996); I. Ginzburg, S. Panfil, and V. Serbo, Nucl. Phys. B **284**, 685 (1987); **296**, 569 (1988).
[4] J. Nemchik, N. N. Nikolaev, E. Predazzi, and B. G. Zakharov, Z. Phys. C **75**, 71 (1997).
[5] J. Nemchik, N. N. Nikolaev, E. Predazzi *et al.*, JETP **86**, 1054 (1998).
[6] J. Crittenden, Springer Tracts Mod. Phys., Vol. **140**, Springer, Berlin, Heidelberg, 1997; ZEUS Collaboration, DESY No. 98-107; H1 Collaboration, Phys. Lett. B **421**, 385 (1998).
[7] D. O. Riska, Acta Phys. Pol. B **29**, 2389 (1998); L. Ya. Glozman and D. O. Riska, Phys. Rep. **268**, 263 (1996).
[8] E. V. Kuraev, N. N. Nikolaev, and B. G. Zakharov, JETP Lett. **68**, 667 (1998).
[9] N. N. Nikolaev and B. G. Zakharov, Phys. Lett. B **332**, 177 (1994); Z. Phys. C **53**, 331 (1992).
[10] L. N. Lipatov, Sov. Phys. JETP **63**, 904 (1986); L. N. Lipatov, in *Perturbative Quantum Chromodynamics*, edited by A. H. Mueller, World Scientific, 1989; E. A. Kuraev, L. N. Lipatov, and S. V. Fadin, Sov. Phys. JETP **44**, 443 (1976); **45**, 199 (1977).
[11] M. V. Terent'ev, Yad. Fiz. **24**, 207 (1976) [Sov. J. Nucl. Phys. **24**, 106 (1976)]; V. B. Berestetskii and M. V. Terent'ev, Yad. Fiz. **25**, 653 (1977) [Sov. J. Nucl. Phys. **25**, 347 (1977)]; L. A. Kondratyuk and M. V. Terent'ev, Yad. Fiz. **31**, 1087 (1980) [Sov. J. Nucl. Phys. **31**, 561 (1980)]; W. Jaus, Phys. Rev. D **41**, 3394 (1990); Phys. Rev. D **44**, 2851 (1991).
[12] V. A. Novikov *et al.*, Phys. Rep. **41**, 1 (1978).

Published in English in the original Russian journal. Edited by Steve Torstveit.

Generation of the second optical harmonic in porous-silicon-based structures with a photonic band gap

L. A. Golovan', A. M. Zheltikov,* P. K. Kashkarov,[1)] N. I. Koroteev, M. G. Lisachenko, A. N. Naumov, D. A. Sidorov-Biryukov, V. Yu. Timoshenko, and A. B. Fedotov

Department of Physics and International Laser Center, M. V. Lomonosov Moscow State University, 119899 Moscow, Russia

(Submitted 13 January 1999)
Pis'ma Zh. Éksp. Teor. Fiz. **69**, No. 4, 274–279 (25 February 1999)

Efficient generation of the second optical harmonic is observed experimentally in a multilayer periodic structure based on porous silicon. The second-harmonic signal is much stronger than the signal from a uniform porous silicon layer or from the single-crystal silicon substrate. The orientational dependence of the second-harmonic signal is isotropic. The second-harmonic intensity as a function of the reflection angle reaches a maximum in the direction corresponding to the minimum phase detuning in a multilayer periodic structure. © *1999 American Institute of Physics.* [S0021-3640(99)00404-1]

PACS numbers: 42.70.Qs, 42.65.Ky

Porous silicon (PS) has been the object of intense study in the last ten years (see, e.g., the review[1]). The interest in this material is due to the fact that nanometer-size clusters can form in it under certain preparation conditions. This and the fact that PS possesses an extended surface make PS a promising material for various technological applications.

New applications of porous silicon are opening up in connection with the possibility of using this material to make one- and two-dimensional microstructures and submicrostructures with a periodically varying index of refraction (see reviews[2,3]). Specifically, PS superlattices open up wide possibilities for producing optical filters with controllable characteristics. The idea of using periodic structures consisting of PS layers with periodically varying porosity as Bragg reflectors and microresonators is discussed in Ref. 4. In this connection it is important to understand the possibilities of using periodic PS structures for controlling not only linear but also nonlinear optical processes. As was shown in Ref. 5, the dispersion properties of periodic structures can be used for this purpose. An increase in the second-harmonic generation efficiency in structures with photonic band gaps created from materials with a bulk quadratic nonlinearity has been observed in a number of experimental works (see, e.g., Ref. 6). The development of PS-based structures with photonic band gaps is important in connection with the possibility of solving a variety of important applied and fundamental problems, including the

 © 1999 American Institute of Physics

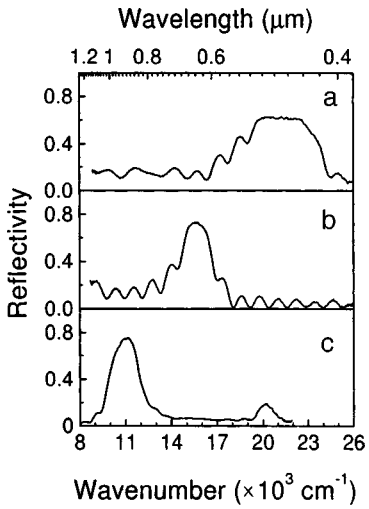

FIG. 1. Reflection spectra of the superlattices *A* (a), *B* (b), and *C* (c) for normal incidence of light.

control of the parameters of short light pulses,[7] the development of new types of Bragg reflectors and chirped mirrors,[8] and the development of compact optical delay lines.[9]

It has been established previously that second-harmonic generation (SHG) in PS is very inefficient. The second-harmonic signal in PS is at least an order of magnitude weaker than the signal from the crystalline-silicon substrate.[10] This fact is explained by the optical isotropy of PS on scales of the order of a wavelength. Second-harmonic generation in PS becomes appreciable only after thermovacuum treatment of the silicon, which is accompanied by the appearance of new surface states and stresses in a subsurface layer.[11] The basic idea of increasing the SHG efficiency in PS implemented in the present work is to decrease the phase detuning for the SHG process by producing a periodic multilayer structure consisting of PS. As we show in the present letter, this approach makes it possible to increase the SHG efficiency substantially in superlattices based on silicon nanostructures as compared with the second-harmonic signals both from a uniform PS layer and from the single-crystal silicon that serves as a substrate for this structure.

Porous-silicon-based multilayer structures were produced by electrochemical etching of single-crystalline silicon wafers in a 1:1 solution of HF in ethanol. The substrate consisted of *p*-type silicon with (100) surface orientation and resistivity $\sim 10\ \Omega\cdot$cm. Electrochemical etching was performed by successively applied current pulses. The current densities were 5 and 105 mA/cm^2. The thickness of layers with different porosity could be controlled by varying the duration of the pulses. Three multilayer structures (*A*,*B*, and *C*) with different PS layer thicknesses were produced. Each structure contained 12 pairs of layers with porosities of about 70 and 80%. The samples prepared luminesce in the region 550–800 nm, indicating the formation of nanocluste rs in the PS layers.[1] The superlattices obtained act as Bragg reflectors. The reflection spectra for them are displayed in Fig. 1. Changing the angle of incidence of light on the sample shifts the reflection maxima (see Fig. 2). This makes it possible to adjust the dispersion of the

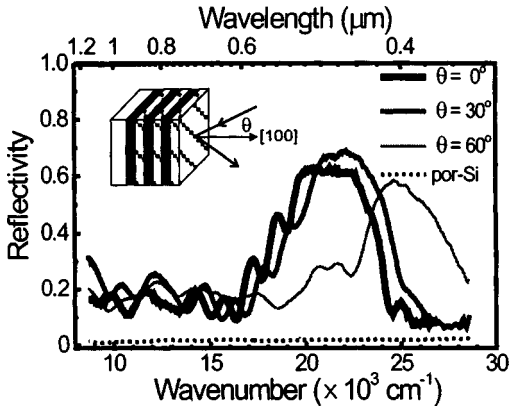

FIG. 2. Reflection spectra of superlattice *A* for light incident in the direction of the normal and at angles of 30° and 60° (solid lines). The dotted line shows the reflection spectrum of a uniform layer of porous silicon with 80% porosity for normal incidence of the light. Inset: Schematic diagram of the experimental structure.

structure for the SHG process. Satisfactory agreement between the experimental data and the computational results obtained by the matrix method was achieved for refractive indices of the layers $n_1 \sim 1.4$ and $n_2 \sim 1.2$. The thicknesses of the low- and high-porosity layers were $d_1 = 87$ nm and $d_2 = 95$ nm for the *A* structure, $d_1 = 111$ nm and $d_2 = 137$ nm for the *B* structure, and $d_1 = 178$ nm and $d_2 = 150$ nm for the *C* structure.

The apparatus developed for investigating SHG in reflection from a multilayer PS structure consists of a picosecond laser system and an automated detection system. The picosecond laser system includes a Nd:YAG master oscillator with passive mode locking and Q switching, and a system for extracting single pulses using an electrooptic shutter and two amplification cascades.[12] The laser pulse at the exit of the amplifying cascades has a duration of about 35 ps and energy up to 3 mJ with a Gaussian spatial distribution of the intensity in the cross section of the beam of amplified radiation. The repetition frequency of the generation pulses was 1 Hz. Radiation at 1.06 μm is used as the pump wave in the second-harmonic generation scheme in reflection from a periodic PS structure. The pump radiation is linearly polarized. The second-harmonic signal was detected with an FEU-106 photomultiplier. Acquisition and processing of the experimental data were performed with a boxcar integrator and a personal computer.

The dependence of the second-harmonic intensity on the angle of rotation of the sample around the normal to its surface for the superlattice *A* is presented in Fig. 3. The second-harmonic signal is seen to be virtually independent of the azimuthal rotation angle. The second-harmonic radiation was completely *p* polarized. The SHG efficiency with pumping by *p*-polarized radiation is higher than for *s*-polarized radiation at the fundamental frequency. The intensity of the second harmonic generated in the PS-based superlattice is more than an order of magnitude higher not only than the second-harmonic signal from a uniform PS layer of high or low porosity but also than that of the crystalline silicon, with (100) surface orientation, on which the superlattice was formed.

Figure 4 displays the dependences of the second-harmonic intensity on the angle of incidence for the superlattices A, B, and C. The superlattice A made it possible to achieve

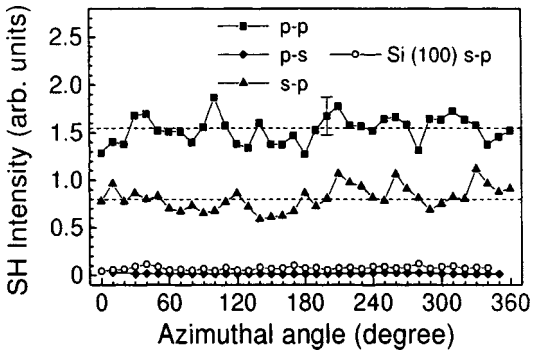

FIG. 3. Orientational dependences for second-harmonic signal generated in superlattice *A* for different polarizations of the radiation at the fundamental and second-harmonic frequencies: $p-p$(■),$p-s$(♦), and $s-p$(▲). The orientational dependence (○) of the second-harmonic signal for the (100) single-crystalline silicon serving as the substrate for the superlattice.

the maximum second-harmonic intensity. The dependence of the second-harmonic intensity on the angle of incidence is nonmonotonic: The second-harmonic intensity is very low at an angle of incidence θ close to normal incidence and reaches its maximum value at $\theta = 55°$. The second-harmonic signal for the superlattices B and C is much weaker, and the maxima of these signals are reached at larger angles of incidence.

To explain the experimental data we consider first the fact that there is no orientational dependence when the *p* polarization of the second harmonic predominates (Fig. 3). This effect as well as the high SHG intensity for pumping with *p*-polarized radiation are apparently explained by the characteristic structural features of the porous layer. As is well known, pores grow in the (100) direction,[1,2] i.e., in a direction normal to the superlattice. Thus silicon nanoclusters exhibit anisotropy (of the ellipsoidal type[1,13]), and their linear susceptibility in a direction normal to the structure is much higher than in perpendicular directions. Treating the silicon nanoclusters as an elementary dipole, one would expect the most efficient excitation and reemission to correspond to *p* polarization of the wave. Evidently, the orientational dependence vanishes because of the optical isotropy of

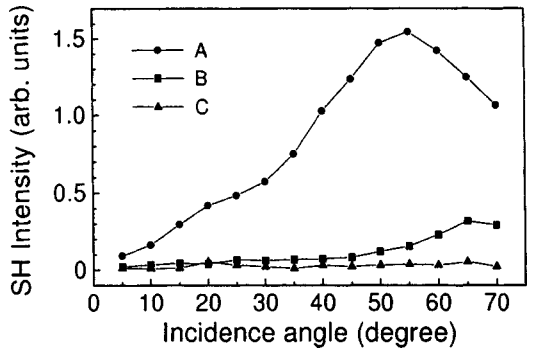

FIG. 4. Second-harmonic intensity versus the angle of incidence of the radiation at the fundamental frequency for superlattices A, B, and C.

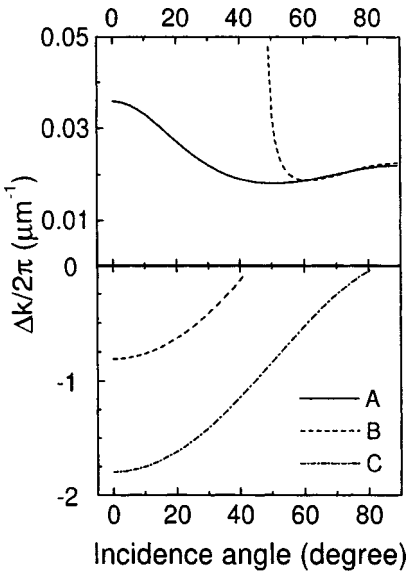

FIG. 5. Calculated detuning Δk of the wave numbers versus the angle of incidence of the radiation at the fundamental frequency for superlattices A, B, and C.

the experimental structure in directions perpendicular to the normal direction. The difference of the intensities of the second harmonic for the superlattices A, B, and C attests to the fact that SHG generation is not associated with stresses that could arise in the structure or at its interface with the substrate.

The most interesting effect observed is the dependence of the second-harmonic generation efficiency on the angle of incidence of the pump radiation on the sample (Fig. 4). The dependence of the detuning of the wave numbers k_1 and k_2 of the radiation at the fundamental and doubled frequencies on the angle of incidence of the radiation was analyzed taking into account the dispersion of the multilayer periodic structure (see, for example, Ref. 14) and the material dispersion of the PS. Based on the measurements of the reflection, the difference of the refractive indices at 1.064 μm and 0.532 μm was estimated to be 0.01 for the high-porosity layer and 0.005 for the low-porosity layer, in agreement with the data presented in Fig. 3. The dependence of the detuning $\Delta k = k_2 - 2k_1$ of the wave vectors on the angle of incidence of the radiation, calculated for periodic structures with the parameters indicated above in the direction of propagation of the pump radiation, is presented in Fig. 5. The detuning Δk reaches its minimum value for definite angles of incidence of the radiation. According to the calculations for the structure *A* this angle is 50°, which is close to the angle corresponding to the experimentally observed maximum efficiency of SHG. The small difference between the values of these angles can be explained by the role of Fresnel factors, which decrease the pump intensity because of an increase in the reflection coefficient with increasing angle of incidence.

In summary, we have established experimentally that in a multilayer periodic structure based on porous silicon the SHG efficiency is much higher than in a uniform layer of

porous silicon and on the surface of single-crystal silicon. The SHG efficiency depends strongly on the thicknesses of the layers. The radiation at the second-harmonic frequency is *p* polarized, and its intensity does not depend on the angle of rotation of the structure in a plane perpendicular to the normal. The intensity of the second harmonic was found to be a nonmonotonic function of the angle of incidence of the pump radiation on the sample. The effects observed are attributed to the fact that at a definite angle of incidence the phase detuning for the SHG process reaches a minimum value in the structure.

This work was supported in part by the State Scientific and Technical Programs ''Atomic Surface Structures'' (Project No. 96-1.33) and ''Physics of Solid-State Nanostructures'' (Project No. 1-066/3) and by the Russian Fund for Fundamental Research (Project No. 97-02-17351). We thank I. Ziber and G. M. Zaĭtsev for assisting in this work.

*e-mail: zhelt@ilc.phys.msu.su
[1)]Deceased.

[1] A. G. Gullis, L. T. Canham, and P. D. J. Calcott, J. Appl. Phys. **82**, 909 (1997).
[2] L. Pavesi, Riv. Nuovo Cimento **20**, Ser. 4, No. 10, 1 (1997).
[3] W. Theiß, Surf. Sci. Rep. **29**, 91 (1997).
[4] G. Mattei, A. Marucci, V. A. Yakovlev, and M. Pagannone, Laser Phys. **8**, 755 (1998).
[5] N. Bloembergen and A. J. Sievers, Appl. Phys. Lett. **17**, 483 (1970).
[6] J. P. van der Ziel and M. Illegems, Appl. Phys. Lett. **28**, 437 (1976).
[7] A. M. Zheltikov, N. I. Koroteev, S. A. Magnitskiĭ, and A. V. Tarasishin, Kvant. Elektron. (Moscow) **25**, 885 (1998).
[8] A. Stingl, M. Lenzner, Ch. Spielmann *et al.*, Opt. Lett. **20**, 602 (1995).
[9] M. Scalora, R. J. Flynn, S. B. Reinhardt *et al.*, Phys. Rev. E **54**, R1078 (1996).
[10] L. A. Golovan', A. V. Zoteev, P. K. Kashkarov, and V. Yu. Timoshneko, Pis'ma Zh. Tekh. Fiz. **20**(8), 66 (1994) [Tech. Phys. Lett. **20**, 334 (1994)].
[11] M. Cavanagh, J. R. Power, J. F. McGilp *et al.*, Thin Solid Films **255**, 146 (1995).
[12] A. M. Zheltikov, N. I. Koroteev, and A. B. Fedotov, Laser Phys. **4**, 569 (1994).
[13] Al. L. Efros, M. Rosen, B. Averboukh *et al.*, Phys. Rev. B **56**, 3875 (1997).
[14] A. Yariv and P. Yeh, *Optical Waves in Crystals*, Wiley, New York, 1984.

Translated by M. E. Alferieff

Trapping of Langmuir waves inside an extended inhomogeneity of magnetized plasma

V. V. Vas'kov*
Institute of Terrestrial Magnetism, the Ionosphere, and Propagation of Radio Waves, Russian Academy of Sciences, 142092 Troitsk, Moscow Region, Russia

A. V. Kostrov,† G. A. Luchinin, and A. A. Shaĭkin‡
Institute of Applied Physics, Russian Academy of Sciences, 603600 N. Novgorod, Russia

(Submitted 15 December 1998)
Pis'ma Zh. Éksp. Teor. Fiz. **69**, No. 4, 280–283 (25 February 1999)

The trapping of Langmuir waves in a cylindrical plasma resonator with a negative density perturbation is observed experimentally. © *1999 American Institute of Physics.* [S0021-3640(99)00504-6]

PACS numbers: 94.20.Bb, 41.20.Jb, 94.20.Ww

1. It is well known that a small-scale structure consisting of thermal inhomogeneities in the form of cylindrical regions with a depressed electron density ($\delta N<0$) which and extended along the magnetic field **H** develops in ionospheric plasma in the field of a high-power radio wave. Such inhomogeneities form as a result of nonuniform heating of the plasma by the field due to potential oscillations excited by the high-power radio wave near the upper-hybrid resonance $N_0 \approx N_R = m(\omega^2-\omega_{He}^2)/4\pi e^2$ as a result of polarization of the perturbations δN. Here N_0 is the electron density in the undisturbed plasma, N_R is the resonance value of the electron density, ω is the frequency of the radio wave, and $\omega_{He}=eH/mc$ is the electron gyrofrequency. The mechanism leading to the intensification of the local heating of inhomogeneities as a result of the excitation and trapping of short-wavelength plasma oscillations — upper-hybrid plasma waves which easily give up their energy to the electrons — in their interior volume was investigated theoretically in Refs. 1–3. This process appears under conditions such that the electron density $N=N_0+\delta N(r)$ inside an inhomogeneity at some point $r=r_R$ crosses the upper-hybrid resonance level $N=N_R$ (here r is the radial coordinate measured from the axis of the prolate inhomogeneity). When a plasma wave with frequency $\omega>2\omega_{He}$ is propagating nearly orthogonally to the magnetic field **H**, then short-wavelength plasma waves propagate inside the inhomogeneity ($r<r_R$, where the density $N<N_R$), with a transverse wave number $k_{p\perp}$ that depends on the electron temperature T_e as $k_{p\perp}=\sqrt{m(\omega^2-4\omega_{He}^2)(N_R-N)/3T_eN}$. In the region outside the inhomogeneity ($r>r_R$, where $N>N_R$), plasma waves with high longitudinal wave numbers $k_\parallel=\mathbf{k}\cdot\mathbf{H}/H>\omega/c$ can propagate in addition to the longer-wavelength waves of the cold Z mode, which is directly excited by a high-power radio wave. Near the upper hybrid resonance $N=N_R$ the cold and plasma oscillations with small $k_\parallel$ interact with and transform into one another. The mechanism leading to trapping of plasma waves inside an inhomogeneity δN depends on the value of the unperturbed electron density N_0 in the background plasma. For

 © 1999 American Institute of Physics

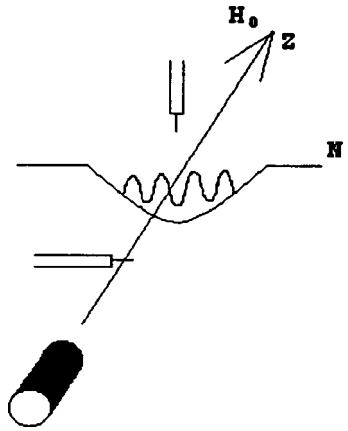

FIG. 1. Layout of the experiment.

$N_0 > N_{PR} \equiv m\omega^2/4\pi e^2$ modes with quite large wave numbers $k_\parallel \geqslant \omega/c$ become trapped inside the plasma waveguide. These waves are reflected near the plasma resonance level $N = N_{PR}$. Wave trapping in a plasma with density $N_0 < N_{PR}$ is due to the breakdown of the geometrical-optics approximatio n for cold oscillations. It occurs for inhomogeneities with a sufficiently small radius $r_0 < k_{Z\perp}^{-1}$, where $k_{Z\perp} = (\omega_{He}/c)(1 + k_\parallel^2 c^2/\omega^2)^{1/2}\sqrt{N_R/(N_0 - N_R)} \geqslant \omega/c$ is the transverse wave number of the cold Z mode in the undisturbed plasma. In this case it can be assumed that a plasma wave is reflected from the upper-hybrid resonance level $N = N_R$ (this is the situation realized in ionospheric experiments). We note also that for $\omega < 2\omega_{He}$ a prolate inhomogeneity δN with a depressed density does not confine plasma waves, i.e., trapping does not occur (for $\omega < 2\omega_{He}$ the plasma waves, like the as cold oscillations, propagate only in the region $N > N_R$).

In the present work the trapping of plasma waves in an initially prescribed cylindrical plasma inhomogeneity with a small radius $r_0 < c/\omega$ is investigated under laboratory conditions.

2. The experiments were performed on the Ionosfera device, made from a vacuum chamber 150 cm long and 80 cm in diameter. The plasma was produced in a uniform magnetic field **H**, directed along the axis of the device, by a pulsed plasma source. The working gas was helium at pressure $P \approx 10^{-2}$ torr. The measurements were performed in a decaying plasma with a characteristic decay time $\tau_N \approx 2 \times 10^{-3}$ s. The electron and ion temperatures in the decay stage had equalized, $T_e \approx T_i \approx 0.5$ eV. The characteristic diameter of the plasma column with a nearly parabolic transverse distribution was 40 cm.

The layout of the experiment is shown in Fig. 1. A depressed-density plasma channel was produced using a dielectric target (10 mm long and 10 mm in diameter, with a dielectric constant $\epsilon = 1$), placed at the center of the plasma column. As a result of the diffusion of the plasma onto the target and subsequent recombination, at the surface of the dielectric the density along the magnetic field was depleted and a highly elongated cylindrical inhomogeneity with reduced density was formed (see Fig. 2a). The relative

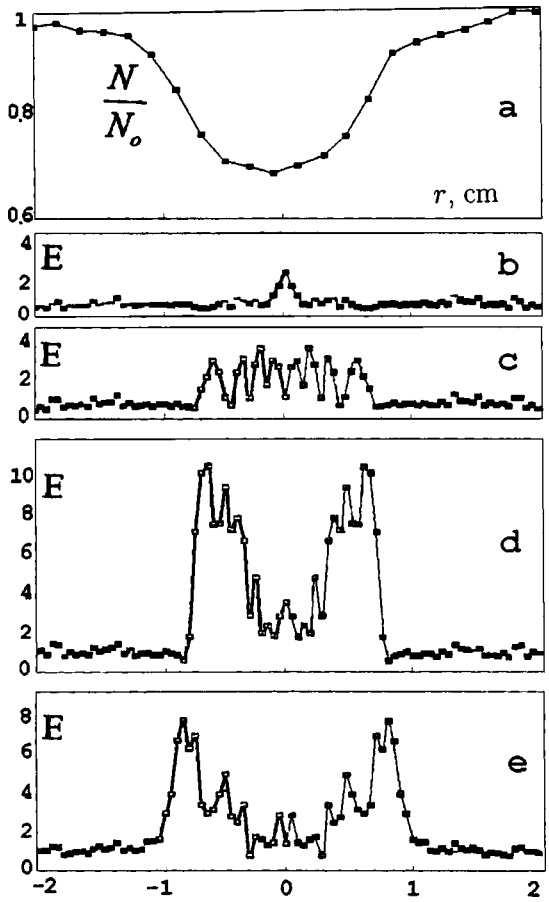

FIG. 2. a) Variation of the relative electron density inside the channel; b–e) results of measurements of the radial component of the electric field E of trapped waves for various values of the unperturbed density N_0.

variation $N(r)/N_0$ of the electron density in the channel produced remained constant in a wide range of variation of $N_0(t)$.

An electric stub antenna of length $L \approx 3$ mm was placed on the channel axis 1 cm from the target. The antenna was oriented perpendicular to the magnetic field. An rf signal with frequency $f = \omega/2\pi = 2.4$ GHz was fed continuously to the antenna. The transverse structure of the radial component $E(r)$ of the electric field in the plasma inhomogeneity was measured at various distances z from the emitting antenna using miniature mobile antennas (length $l \sim 1$ mm). The experimental curves presented below correspond to a magnetic field $H = 420$ Oe ($\rho_{Hi} \approx 0.34$ cm), for which the pump frequency was just slightly greater than twice the electron gyrofrequency $f_{He} = \omega_{He}/2\pi = 1.17$ GHz. The relative density distributio n $N(r)/N_0$ in the wave channel is shown in Fig. 2a. The maximum channel depth at the center of the inhomogeneity was $|\delta N(r=0)|/N_0 = 0.4$, and the channel radius $r_0 \approx 1$ cm was twice the target radius.

The experiments performed make it possible to conclude that the formation of

trapped modes of plasma oscillations occurred when the electron density inside the channel crossed a resonance level (upper hybrid or plasma), which determined the position of the reflection point $N=N_{\rm ref}$ of the plasma wave. The evolution of the structure of the electric field of the trapped waves, with the electron density $N_0(t)$ decreasing in time, at a distance $z=2$ cm from the emitting antenna is displayed in Figs. 2b–2e. Figure 2b shows the structure of the electric field at the moment when the density on the channel axis is $N_{\rm ref}$. Figure 2c shows the distribution of the radial component of the electric field at the moment when the point $N_{\rm ref}$ is 6 mm from the axis of the wave channel. One can see that the structure of the electric field during this period has the form of a standing wave with an almost constant amplitude. The displacement of the reflection point of the wave along the slope of the inhomogeneity in time was accompanied by intensification of the field at the boundary of the trapping region and weakening of the field at the center of the inhomogeneity (Fig. 2d). Pronounced oscillations of $E(r)$, which are characteristic for a standing wave, were not observed in this case. It can be supposed that the suppression of spatial oscillations and the substantial decrease in the amplitude E near the center of the inhomogeneity are due to the fact that the wavelength of the plasma oscillations decreases with distance from the reflection point, and, correspondingly, the plasma oscillations are detected less efficiently by a measuring antenna with a finite length $l \sim 1$ mm. We call attention also to the sharp decrease in the amplitude of the plasma waves outside the transparency region, in the vicinity of which their electric field is intensified. As the density $N_0(t)$ decreased further, the amplitude of the trapped waves decreased (Fig. 2e) and subsequently approached its background value outside the channel.

We underscore that the above-described behavior of trapped waves was observed only for $\omega > 2\omega_{He}$. As the magnetic field was increased to values such that $\omega_{He} > \omega/2$, the amplitude of the electric field inside the channel decreased substantially, in complete agreement with the theoretical assumption that trapping of plasma waves should not occur under these conditions.

3. In summary, our experiments have revealed trapping and amplificati on of plasma oscillations confined inside an elongated inhomogeneity with a depressed electron density ($\delta N<0$), oriented along the magnetic field **H**. The accumulation of energy of plasma oscillations in the resonator causes additional local heating of the inhomogeneities observed in ''active'' experiments on the effect of high-power radio radiation on the ionospheric plasma.

This work was supported by the Russian Fund for Fundamental Research (Grant No. 97-02-17809).

*e-mail: vaskov@izmiran.rssi.ru
†e-mail: kstr@appl.sci-nnov.ru
‡e-mail: shaykin@appl.sci-nnov.ru

[1] K. B. Dysthe, E. Mjolhus, H. Perseli, and K. Rypdal, Phys. Scr. T **2/2**, 548 (1982).
[2] V. V. Vas'kov and A. V. Gurevich, Geomagn. Aeron. **23**, 544 (1983).
[3] V. V. Vas'kov and A. V. Gurevich, Geomagn. Aeron. **23**, 901 (1983).

Translated by M. E. Alferieff

Expansion of matter heated by an ultrashort laser pulse

N. A. Inogamov,* Yu. V. Petrov, and S. I. Anisimov
L. D. Landau Institute of Theoretical Physics, Russian Academy of Sciences, 142432 Chernogolovka, Moscow Region, Russia

A. M. Oparin
Institute of Computer-Aided Design, Russian Academy of Sciences, 123056 Moscow, Russia

N. V. Shaposhnikov
Institute of High Temperatures, Russian Academy of Sciences, 127412 Moscow, Russia

D. von der Linde
Institut für Laser-und Plasmaphysik, Universität-GHS-Essen, D-45117 Essen, Germany

J. Meyer-ter-Vehn
Max-Planck-Institut für Quantenoptik, Hans-Kopfermann-Strasse 1, D-85748 Garching, Germany

(Submitted 28 January 1999)
Pis'ma Zh. Éksp. Teor. Fiz. **69**, No. 4, 284–289 (25 February 1999)

Recent experiments have utilizied high-power subpicosecond laser pulses to effect the ultrafast heating of a condensed material to temperatures far above the critical temperature. Using optical diagnostics it was established that a complicated density profile with sharp gradients, differing substantially from an ordinary rarefaction wave, forms in the expanding heated matter. The present letter is devoted to the analysis of the expansion of matter under the conditions of the experiments reported by D. von der Linde, K. Sokolowski-Tinten, and J. Bialkowski, Appl. Surf. Science **109/110,** 1 (1996); K. Sokolowski-Tinten, J. Bialkowski, A. Cavalleri *et al.*, Proc. Soc. Photo-Opt. Instum. Eng. **3343,** 46 (1998); and, K. Sokolowski-Tinten, J. Bialkowski, A. Cavalleri *et al.*, Phys. Rev. Lett. **81**, 224 (1998). It is shown that if the unloading adiabat passes through the two-phase region, a thin liquid shell filled with low-density two-phase matter forms in the expanding material. The shell moves with a constant velocity. The velocity in the two-phase material is a linear function of the coordinate (flow with uniform deformation), and the density is independent of the coordinate and decreases with time as t^{-1}. © *1999 American Institute of Physics.* [S0021-3640(99)00604-0]

PACS numbers: 52.50.Jm, 65.70.+y

The vaporization of solids by nanosecond and longer pulses of moderate intensity is described well by a surface-vaporization model based on the assumption that the con-

 © 1999 American Institute of Physics

densed and gas phases are separated by a sharp boundary — the vaporization front — on which certain boundary conditions hold[1–3] which relate the solution of the heat-conduction problem for the condensed phase with the solution of the gas-dynamics problem for the vapor. This model is applicable if the vapor density is much lower than the condensed-phase density, i.e., if the temperature on the vaporization front is much lower than the critical temperature of the material. The motion of the vapor is described in this case by a centered rarefaction wave with a smooth density profile.

Recent experiments[4–6] have made it possible to conclude that the character of the motion of the vaporized material is qualitatively different for ultrashort (subpicosecond) laser pulses. The density profile becomes nonmonotonic, and sections with large density gradients form in it. In the present letter the dynamics of the expansion of the matter heated by an ultrashort pulse is studied, and an attempt is made to explain certain effects observed in Refs. 4–6.

In metals and semiconductors, which were used as targets in Refs. 4–6, laser radiation is absorbed mainly by the conduction electrons. The absorbed energy propagates into the interior of the sample by electronic heat conduction and is slowly (because of the large difference between the electron and ion masses) transferred to the crystal lattice. At this stage the hydrodynamic motion can be neglected. The motion of the matter comes into play at times of the order of the characteristic electron–ion energy transfer time, when the rarefaction wave overtakes the electronic heat wave (see, for example, Ref. 7). In normal-density metals this time is ordinarily 1–10 ps. On this basis, it is obvious that by the onset of hydrodynamic motion a surface layer of thickness $l \sim \max(\delta, \sqrt{\chi \tau_{ei}})$ in the target is heated to temperature $T_0 \sim Q/lc_V$, where δ is the skin depth, χ is the electronic thermal conductivity, τ_{ei} is the electron–lattice relaxation time, Q is the absorbed energy (per unit surface area), and c_V is the specific heat per unit volume. Under the experimental conditions of Refs. 4–6, the heated layer was $\sim$100 nm thick, and the temperature was of the order of several thousands of degrees. Therefore for ultrashort pulses it is necessary to solve the problem of the adiabatic expansion of a preheated layer instead of the standard problem of the propagation of a vaporization front. As will become evident below, the solution of this problem depends strongly on the equation of state of the material and the initial entropy of the layer. If the entropy is such that the unloading adiabat lies in the two-phase region in the phase diagram, the flow becomes qualitatively different from the standard rarefaction wave in an ideal gas. Specifically, a layer of liquid with very sharp boundaries, whose thicknesses are much smaller than the optical wavelength, forms in the expanding matter. Such a flow structure agrees qualitatively with the experiments of Refs. 4–6.

Let us examine in greater detail a very simple model of the flow. Let a layer of thickness l, uniformly heated to temperature T_0, be deposited on a rigid undeformable substrate. The initial matter density ρ_0 equals the initial solid-state density, and the initial pressure is determined by the equation of state. We shall assume that local thermodynamic equilibrium in the matter is not destroyed during the expansion process (some remarks about the possible influence of nonequilibrium conditions will made below). For estimates and numerical calculations we shall employ wide-range tables of the thermodynamic functions, constructed by the method developed in Ref. 8. The change in the state of the matter during the expansion process follows an adiabat passing through the initial point (p_0, ρ_0). We shall be interested in the case where the expansion adiabat

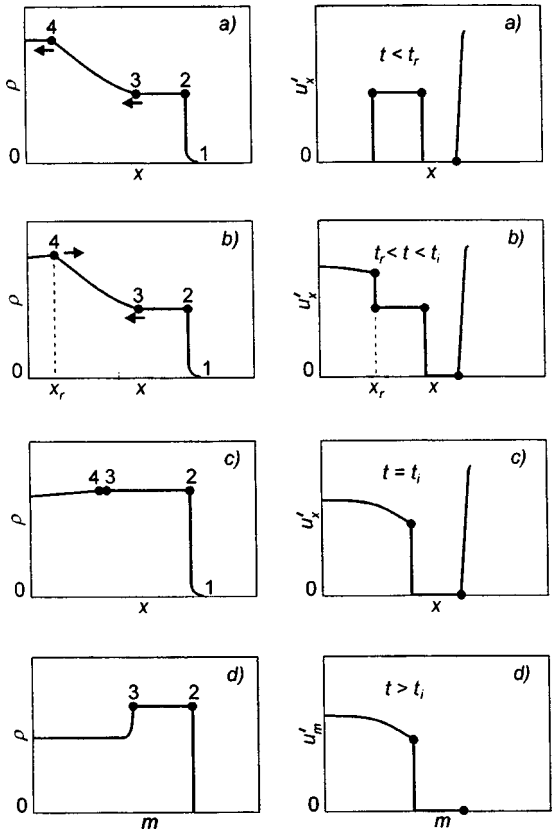

FIG. 1. Stages in the evolution of the profile of ρ (left-hand column) and of the rarefaction velocities u'_x or u'_m (right-hand column) in the process of expansion of a heated layer. a) A rarefaction wave with a uniform layer *2–3* that expands in proportaion to t is traveling toward the boundary with the substrate ($x=0$). b) The acoustic characteristic $x_r(t)$ reflected from the boundary $x=0$ bounds the region of interference of the incident and reflected waves. The rarefaction in the region of two waves $0<x<x_r$ is greater than in the region of one wave. c) The characteristic $x_r(t)$ overtakes the layer *3–2*. d) ''Freezing'' of the expansion (coasting).

intersects the binodal at a certain point (p_1,ρ_1) in the (p,ρ) plane and enters a two-phase region. The most important feature of this case is the sharp decrease in the sound velocity at the point of intersection of the adiabat and the binodal. Calculating the derivative $\gamma(\rho)=(d\ln p/d\ln\rho)_S$ using the tables of thermodynamic functions, it is easy to see that near the binodal one has $\gamma(\rho)\gg 1$ in the one-phase region and $\gamma(\rho)\ll 1$ in the two-phase region. The abrupt decrease in the sound velocity radically changes the structure of the rarefaction wave.

A qualitative picture of the flow is shown in Fig. 1. Initially, the heated layer occupied the segment $0<x<l$. The rigid substrate occupies the region $x<0$. A self-similar rarefaction wave (RW) is present on the right-hand edge. The acoustic family of characteristics moving from right to left through the material form in the (x,t) plane a fan of straight lines $\xi=(x-l)/c_0t$, where c_0 is the initial sound velocity.[9] Matching the self-similar solutions on both sides of the point (p_1,ρ_1), at which the function $\gamma(\rho)$ has

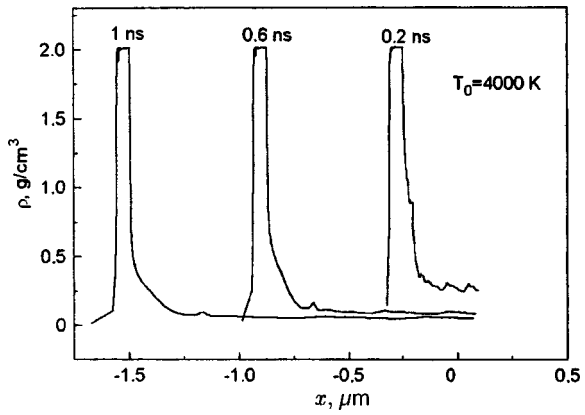

FIG. 2. Evolution of the density distributions.

a discontinuity, it is easy to verify that this point is mapped onto the finite segment *2–3* in the (ξ,ρ) plane. The density on this segment is $\rho(\xi)\equiv\rho_1=\text{const}$. All other points of the adiabat $p(\rho)$ are in a one-to-one correspondence with the points of the function $\rho(\xi)$. The single-valuedness of the mapping at the point of intersection of the isentrope and binodal breaks down because of the uniformity of the initial data and the degeneracy of the RW (all lines $\xi=\text{const}$ are characteristics). For initial data of a general form the strict uniformity of the flow in the region *2–3* will break down.

At time $t_r=l/c_0$ the rarefaction wave reflects from the rigid substrate. For $t>t_r$ a reflected wave, whose front is located at the point $x_r(t)$ (see Fig. 1b), is superposed on the leftward traveling RW. The arrows in Figs. 1a and 1b indicate the direction of motion of the fronts. For $t_r<t<t_i$ the fronts *3* and *4* move toward each other. The front *2* moves with a very low velocity relative to the material. At $t=t_i$ the reflected characteristic *4* overtakes the point *3* (see Fig. 1c) and ''sticks'' to it, since the sound velocity, with which it moves relative to the material, decreases abruptly to a very low value. For $t>t_f(t_f\approx t_i)$ the sound velocity becomes low in the entire material. A ''freezing'' of the acoustic disturbances occurs, and a hypersonic expansion regime is established. The distribution $u(m,t)$ of the velocity over the Lagrangian particles becomes time-independent. The region *0–3* expands with time $(u'_m>0)$, and the density in it decreases. In the layer *2–3* (the ''shell'') the density remains constant and equal to ρ_1, since in this layer $u'_m\equiv 0$. Therefore the nonmonotonicity of the density profile first appears at $t=t_i$ and then increases with time (see Fig. 1d).

The numerical solution of the gas-dynamics equations confirms the flow scheme described above. The computational results for aluminum are displayed in Figs. 2–4. A semiempirical equation of state was used.[8] The initial thickness l of the heated layer was 100 nm, and the initial temperature was 4000 K. Figure 2 shows the evolution of the density profile for $t>t_f$ after the main elements of the structure are formed (expansion occurs in the negative direction along the x axis). A liquid shell approximately 70 nm thick moves in front. The density ρ_1 and the velocity of the shell remain constant for a long time (much longer than the formation time of the shell). The matter inside the shell is in a two-phase state, and its density ρ_2 is virtually independent of the coordinate and

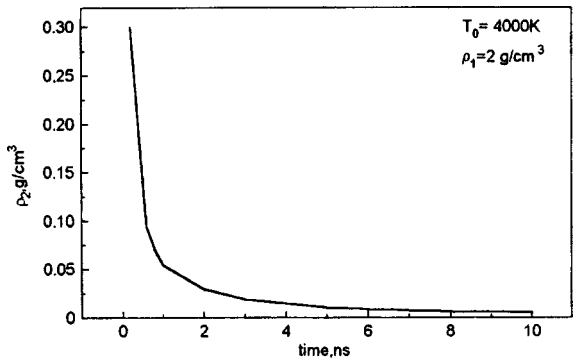

FIG. 3. Decrease of the density of the two-phase matter in time.

decreases in time as $1/t$ (Fig. 3). Figure 4 shows the velocity profiles at various times. One can see that the shell moves without appreciable deformation with a velocity of approximately 1.5 km/s, and the matter inside it undergoes uniform expansion (the velocity depends linearly on the coordinate).

The calculation described above was performed under the assumption that local thermodynamic equilibrium holds in the expanding matter. The equation of state employed was constructed following Maxwell's rule.[10] In this connection, there arises the question of the possible effect of the metastable states and their decay kinetics on the above-described picture of the expansion. In our case, as one can readily appreciate, the fluctuation-nucleation kinetics of the transition from the one-phase to the two-phase state, while determining the microstructure of the medium, will not greatly influence the density and velocity profiles. The reason is that the differences between the equilibrium and nonequilibrium descriptions become substantial at pressures of the order of p_1, while the velocity field is formed at pressures of the order of p_0, several orders of magnitude greater than p_1. This qualitative reason is confirmed by a direct numerical calculation similar to that described above but using an equation of state that takes the metastable states into account. The average density and mass-velocity profiles obtained in this cal-

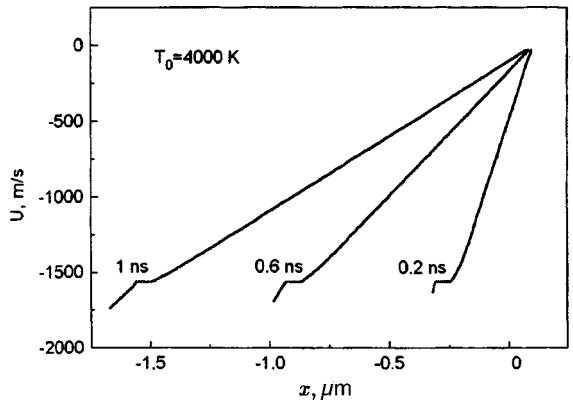

FIG. 4. Evolution of the velocity distributions.

culation are virtually identical to the results of equilibrium calculations. It is interesting to note that a flow structure similar to that described above is also obtained by molecular-dynamics simulation of the vacuum expansion of a superheated Lennard-Jones liquid. Thus, the formation of a structure consisting of a liquid shell filled with a low-density two-phase material is a characteristic feature of the expansion of a uniform layer of instantaneously heated liquid.

The Newton's rings observed in the experiments of Refs. 4–6 are caused by the interference of waves reflected from the outer boundary of the shell and from the unvaporized part of the target. Hence it follows that the shell weakly absorbs the probe radiation. The calculations show that in the case of aluminum the shell density ρ_1 is 1.5–2 times less, depending on the initial temperature T_0, than the initial density (higher values of T_0 correspond to lower values of ρ_1). If it is assumed that the free-electron density in the shell material remains proportional to the density, the plasma frequency under typical conditions is much higher than the frequency of the probe radiation ($\lambda = 620$ nm, $\omega = 3\times 10^{15}$ s^{-1}). In the example presented in Fig. 2, the shell density is 2 g/cm^3 and the shell thickness is 70 nm. Assuming that in the shell material, just as in solid aluminum, there are three free electrons per atom, we find that the fraction of the transmitted radiation is only about 1% of the incident flux. It is well known, however, that the number of free electrons per atom in liquid aluminum is less than in solid aluminum and equals 2.45 at the melting point. The expansion of liquid aluminum should further decrease the number of free electrons and increase the number of bound electrons. It is natural to suppose that these bound states have a large radius and high polarizability. Let us estimate the permittivity of such a liquid. The elementary Drude theory gives

$$\varepsilon = \varepsilon' - i\varepsilon'', \quad \varepsilon' = 1 + \frac{\Omega_p^2}{\omega_0^2 - \omega^2} - \frac{\omega_p^2}{\omega^2}, \quad \varepsilon'' = \frac{\Omega_p^2 \omega^2}{(\omega_0^2 - \omega^2)^2 \omega \tau_0} + \frac{\omega_p^2}{\omega^3 \tau}. \tag{1}$$

The last terms in ε' and ε'' describe the contribution of free electrons; all the other terms correspond to a bound state with binding energy $\hbar\omega_0$. The plasma frequencies of the bound and conduction electrons are, respectively,

$$\Omega_p = \sqrt{\frac{4\pi n_0 e^2}{m_0}}, \quad \omega_p = \sqrt{\frac{4\pi n e^2}{m}},$$

where n_0, m_0, n, and m are the corresponding densities and masses. In Eqs. (1) it is assumed that $\omega\tau_0 \gg 1$ and $\omega\tau \gg 1$, so that $\varepsilon' \gg \varepsilon''$ (τ_0 and τ are the relaxation times of the bound and free electrons). Assuming that the frequencies Ω_p and ω_p are of the same order of magnitude, it can be shown that for $\hbar\omega_0 \simeq \sqrt{2}\hbar\omega = 2.8$ eV the refractive index $N \approx \sqrt{\varepsilon'}$ becomes real. Of course, this interpretation is only a rough scheme, which must be refined by further experiments.

We thank the Russian Fund for Fundamental Research (Grants Nos. 98-02-17441 and 97-02-16044) and the Program for Support of the Leading Scientific Schools (No. 96-15-96448).

*e-mail: nail@landau.ac.ru

[1] S. I. Anisimov, Zh. Éksp. Teor. Fiz. **54,** 339 (1968) [Sov. Phys. JETP **27**, 182 (1968)].
[2] A. A. Bubnov and M. N. Libenson, Inzh.-Fiz. Zh. **25**, 125 (1973).
[3] S. I. Anisimov, Ya. A. Imas, G. S. Romanov, and Yu. B. Khodyko, *The Effect of High-Power Radiation on Metals*, Nauka, Moscow, 1970.
[4] D. von der Linde, K. Sokolowski-Tinten, and J. Bialkowski, Appl. Surf. Sci. **109/110**, 1 (1996).
[5] K. Sokolowski-Tinten, J. Bialkowski, A. Cavalleri *et al.*, Proc. SPIE **3343**, 46 (1998).
[6] K. Sokolowski-Tinten, J. Bialkowski, A. Cavalleri *et al.*, Phys. Rev. Lett. **81**, 224 (1998).
[7] S. I. Anisimov, A. M. Prokhorov, and V. E. Fortov, Usp. Fiz. Nauk **142,** 395 (1984) [Sov. Phys. Usp. **27**, 181 (1984)].
[8] A. V. Bushman and V. E. Fortov, Usp. Fiz. Nauk **140,** 177 (1983) [Sov. Phys. Usp. **26**, 465 (1983)].
[9] L. D. Landau and E. M. Lifshitz, *Fluid Mechanics*, 2nd ed., Pergamon Press, New York, 1987 [Russian original, Nauka, Moscow, 1986].
[10] J. O. Hirschfelder, Ch. F. Curtiss, and R. B. Bird, *Molecular Theory of Gases and Liquids*, John Wiley, New York, 1954, Chap. 5.

Translated by M. E. Alferieff

Effect of electron–phonon interaction on the thermoelectric properties of superlattices

Yu. V. Ivanov and M. V. Vedernikov
A. F. Ioffe Physicotechnical Institute, Russian Academy of Sciences, 194021 St. Petersburg, Russia

Yu. I. Ravich
St. Petersburg State Technical University, 195251 St. Petersburg, Russia

(Submitted 10 January 1999)
Pis'ma Zh. Éksp. Teor. Fiz. **69**, No. 4, 290–295 (25 February 1999)

The electron relaxation time on acoustical phonons, the electrical conductivity, and the phonon-drag thermopower of a semiconductor superlattice with quasi-two-dimensional quantum wells are calculated. The inelasticity of the scattering of charge carriers is taken into account. It is shown that the phonon-drag thermopower of a superlattice can be an order of magnitude greater than the corresponding thermopower of a bulk semiconductor. © *1999 American Institute of Physics.* [S0021-3640(99)00704-5]

PACS numbers: 73.50.Lw, 63.20.Kr

It is shown theoretically in Refs. 1–3 that the thermoelectric figure of merit[1)] of a superlattice with sufficiently narrow quantum wells (QWs) can be an order of magnitude greater than the figure of merit of a bulk semiconductor of the same composition as the QW material. This result is a consequence of the nonzero density of states at the bottom of the lower subband of the size-quantized electron spectrum. For a fixed chemical potential the charge-carrier density in the QW and, together with it, the electrical conductivity of the QW are greater than the corresponding parameters of a three-dimensional semiconductor. The possibility of such a large increase in the thermoelectric figure of merit has attracted much attention from investigators and has sharply increased the topicality of research on the thermoelectric properties of low-dimensional structures.

In subsequent works[4–6] a variety of other features of superlattices were studied. Specifically, the effect of decreasing the electron relaxation time in nanostructures with QWs on the thermoelectric properties was investigated.[6] Hicks and Dresselhaus assumed[1–3] that the charge-carrier mobility does not depend on the quantum well width L. However, it has long been known[7] that in the approximation of elastic scattering of electrons by acoustical phonons the relaxation time and the mobility of the carriers are proportional to L. The density of states is inversely proportional to L. Therefore the electrical conductivity of a superlattice with a fixed chemical potential should not depend on the QW width. In other words a decrease in the mobility compensates the predicted[1–3] increase of the thermoelectric figure of merit. Nonetheless, under some conditions certain features of the electron–phonon interaction in superlattices can still substantially improve

 © 1999 American Institute of Physics

the thermoelectric properties of low-dimensional structures. Two such possibilities are examined in this letter.

1. The approximation of elastic scattering of carriers by acoustical phonons, which was employed in the works indicated above, is not always applicable to superlattices. In a three-dimensional semiconductor an electron with wave vector **k** can interact only with a phonon whose wave vector **q** has a length $q \leqslant 2k$. In a two-dimensional QW the component k_z (the z axis is perpendicular to the plane of the QW) is indeterminate in accordance with the uncertainty relation $\Delta k_z \sim 1/L$. Therefore in a QW elastic excitations with $q_z \sim 1/L$ become involved in relaxation processes (we assume that the acoustical phonons remain three-dimensional in the superlattice). As L decreases, the phase volume of ''electronic'' phonons, i.e., phonons interacting with charge carriers, increases. This increases the electron–phonon collision frequency. Moreover, inelastic scattering of carriers can occur through an increase in the energy of the electronic phonons.

We considered the inelastic scattering of electrons by the deformation potential of three-dimensional acoustical phonons in a superlattice with quasi-two-dimensional QWs. For simplicity, the potential barriers separating the QWs were assumed to be extremely narrow and high. Only the case of nondegenerate carriers with an isotropic parabolic spectrum $\varepsilon(k)$ was investigated. The transition probability $W(\mathbf{k},\mathbf{k}')$ was assumed to be an even function of the second argument to the same accuracy with which this is true for quasielastic scattering in a three-dimensional semiconductor. This made it possible to introduce the electron–phonon relaxation time

$$\tau_{ep}^{-1} = \frac{mD^2(k_BT)^2}{2\pi\hbar^4\rho s_l^3}\int_{-y}^{\infty} xI^2(tx)N_0(x)dx, \tag{1}$$

where $N_0(x) = (\exp(x)-1)^{-1}$, $I(u) = 8\sin(\pi u/2)/\pi u(4-u^2)$, $t = k_BTL/\pi\hbar s_l$, $y = \varepsilon(k)/k_BT$, m is the carrier mass, D is the deformation potential constant, ρ is the density of the material, and s_l is the velocity of longitudinal sound.

Using Eq. (1), it is easy to calculate the in-layer electrical conductivity σ^{2D} of a superlattice. The ratio of this electrical conductivity to the electrical conductivity σ^{3D} of a three-dimensional semiconductor with the same composition as that of the QW material has the form

$$\frac{\sigma^{2\mathrm{D}}}{\sigma^{3\mathrm{D}}} = 12\pi^2\frac{\langle\tilde{\tau}_{ep}\rangle_e^{2\mathrm{D}}}{t}, \tag{2}$$

where

$$\langle F\rangle_e^{2\mathrm{D}} = \int_0^{\infty} F(y)e^{-y}y\,dy, \tag{3}$$

and the dimensionless relaxation time $\tilde{\tau}_{ep}$ differs from τ_{ep} by the absence of the factor in front of the integral in Eq. (1). To calculate $\sigma^{3\mathrm{D}}$, and in the calculations presented below, the average electron–phonon relaxation time $\langle\tau_{ep}^{3D}\rangle_e^{3D}$ of a three-dimensional semiconductor was used. The average $\langle\ldots\rangle_e^{3D}$ is obtained from Eq. (3) by multiplying the integrand by $4y^{1/2}/3\pi^{1/2}$, and the relaxation time τ_{ep}^{3D} is well known.[8]

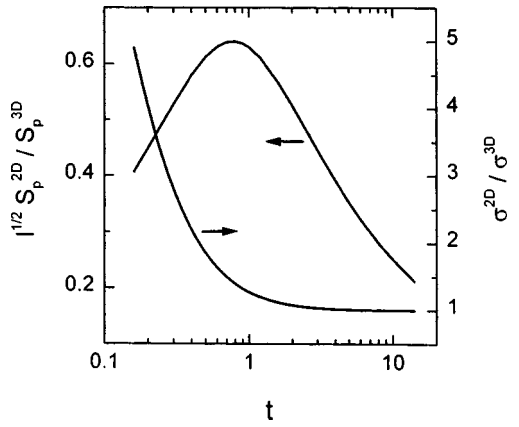

FIG. 1. Reduced thermopower of two-step drag and normalized electrical conductivity of a superlattice versus the reduced temperature t.

The average $\langle \tilde{\tau}_{ep} \rangle_e^{2D}$ is completely determined by the parameter t. The dependence of the ratio (2) on t is presented in Fig. 1. For large values of the product LT the electron scattering is quasielastic, and the ratio of the electrical conductivities is practically unity, as expected. The use of low-dimensiona l structures makes it possible to increase the conductivity only for $t<1$. For example, for a superlattice with $L \approx 2$ nm and $s_l \approx 5$ km/s, this inequality holds for $T<50$ K. This is the temperature range where the qualitative results of the Hicks–Dresselhaus theory hold.[1–3]

2. Another important consequence of an increase in the electron–phonon interaction in superlattices with QWs is the intensificati on of phonon drag, which is manifested as an increase in the phonon component of the thermopower. Such an increase in drag is observed in three-dimensional semiconductors in a quantizing magnetic field.[9–11]

Two drag mechanisms should be distinguished. In pure materials the phonon–phonon interaction predominates, and at low temperatures drag is a two-step process.[9,12,13] The thermal-phonon flux drags electronic phonons, which in turn drag electrons. Scattering by defects and impurities in ''dirty'' semiconductors as well as umklapp processes at sufficiently high temperatures suppress the interaction of thermal and electronic elastic excitations, so that under these conditions only electronic phonons participate in drag.[14]

The processes described above occur in both uniform semiconductors and superlattices. However, in the latter case the electronic phonons have shorter wavelengths. The frequency of their collisions with thermal phonons is high. For this reason two-step drag in superlattices remains dominant at higher defect and impurity densities and at higher temperatures.

In the general case the indicated processes cannot be separated and the description of drag becomes much more complicated. We have examined only the limiting cases indicated above. The calculation of two-step drag was performed in the hydrodynamic approximation.[15] The spectrum of elastic oscillations was assumed to be isotropic and linear. The latter assumption is justified because in the hydrodynamic approximation one

is considering temperatures that are low compared with the Debye temperature. The contribution of two-step drag to the thermopower of the superlattice has the form

$$S_p^{2D}=\frac{m}{eT\langle\tau_{ep}\rangle_e^{2D}\langle\nu_p^R s^{-2}\rangle_p}. \tag{4}$$

Here ν_p^R is the frequency of phonon collisions that the total quasimomentum of the elastic subsystem (umklapp processes, scattering by impurities, and so on), s is the velocity of sound, e is the electron charge, and

$$\langle F\rangle_p=\frac{\sum_j s_j^{-3}\int_0^\infty F_j(x)N_0'(x)x^4dx}{\sum_j s_j^{-3}\int_0^\infty N_0'(x)x^4dx}. \tag{5}$$

The index j enumerates the branches of the phonon spectrum. A prime indicates a derivative with respect to x. The average $\langle\tau_{ep}\rangle_e^{2D}$ in Eq. (4) is easy to calculate numerically using Eqs. (1) and (3). It is more difficult to estimate $\langle\nu_p^R s^{-2}\rangle_p$. Fortunately, in the approximations adopted the second average can be expressed in terms of the lattice thermal conductivity κ. Instead of Eq. (4) we obtain

$$S_p^{2D}=\frac{45m\hbar^3}{2\pi^2 e(\Sigma_j s_j^{-3})(k_BT)^4}\frac{\kappa}{\langle\tau_{ep}\rangle_e^{2D}}. \tag{6}$$

Let us compare the contributions of the two-step drag to the thermopower of a superlattice and a bulk semiconductor. The expression describing the contribution to the thermopower of a three-dimensional semiconductor[12] differs from Eq. (4) only by the average electron–phonon relaxation time.[2)] Therefore

$$\frac{S_p^{2D}}{S_p^{3D}}=\frac{\langle\tau_{ep}^{3D}\rangle_e^{3D}}{\langle\tau_{ep}\rangle_e^{2D}}=\frac{2}{3(2\pi)^{5/2}}\frac{t^{1/2}}{l^{1/2}\langle\tilde{\tau}_{ep}\rangle_e^{2D}}, \tag{7}$$

where $l=ms_lL/\pi\hbar$ is the dimensionless QW width. The right-hand side of this relation is determined by the two parameters t and l. Its dependence on l is monotonic and is contained in the factor $l^{-1/2}$. The combination $l^{1/2}S_p^{2D}/S_p^{3D}$, which is a function of t only, is plotted in Fig. 1. This function determines the temperature dependence of the ratio (7). For a superlattice with a fixed QW width the maximum increase in the thermopower obtains for $k_BT\approx 0.75\pi\hbar s_l/L$. Therefore the smaller the QW width, the higher the temperature to which the maximum of the temperature dependence of the relation (7) shifts.

The curve presented in Fig. 1 can be used to estimate the effect under consideration. If $m\approx 0.01m_0$, $s_l\approx 5$ km/s, and $L\approx 3$ nm, then $\max(S_p^{2D}/S_p^{3D})\approx 30$ at $T\approx 30$ K. Even at $T=100$ K the ratio $S_p^{2D}/S_p^{3D}\approx 20$. It should be noted, however, that in three-dimensional semiconductors at temperatures ~ 100 K two-step drag apparently is not the dominant process, and relation (4) can be used only to estimate an upper bound.

It is more difficult to calculate the second limiting process, whose three-dimensional analog is Herring drag.[14] This type of drag occurs at high temperatures and/or defect densities. So as not to complicate the problem by taking into account the scattering of electrons by defects, we studied only one possible variant, specifically, the case of rela-

tively high temperatures and low impurity-atom densities. This restriction made it possible, specifically, to use the approximation of elastic scattering of carriers by phonons. But even after these simplifications were made, a quite simple result could be obtained only for narrow QWs with $L \ll \pi\hbar\sqrt{2mk_BT}$. This inequality guarantees that the phase volume of the electronic phonons will be highly elongated in the direction of the symmetry axis of the superlattice. Phonon drag in a structure with wide QWs, in which the electronic phonons are localized near the center of the Brillouin zone, is virtually identical to drag in a three-dimensional semiconductor.

The phonon contribution to the thermopower of a superlattice in our limiting case can be written in the form

$$S_p^{2D} = \frac{ms_l^2}{eT} \frac{\langle\langle \tau_l \rangle^{2D}\rangle_e^{2D}}{\langle \tau_{ep} \rangle_e^{2D}}. \tag{8}$$

Here τ_l is the total relaxation time of longitudinal phonons; the average $\langle \ldots \rangle_e^{2D}$ is defined in Eq. (3); and

$$\langle \tau_l \rangle^{2D} = \frac{\int_0^\infty \tau_l(q)\xi^3 I^2(p\xi)D(\xi)\, d\xi}{\int_0^\infty \xi^3 I^2(p\xi)D(\xi)\, d\xi}, \tag{9}$$

where $\xi = q/2k, p = 2kL/\pi, D(\xi) = [K(\xi) - E(\xi)]/\xi^2$ for $\xi \leqslant 1$ and $D(\xi) = [K(1/\xi) - E(1/\xi)]/\xi$ for $\xi > 1$, and $K(\xi)$ and $E(\xi)$ are complete elliptic integrals of the first and second kinds, respectively.

Formula (8) and the formula describing Herring drag in a three-dimensional semiconductor[8] differ only by the average relaxation times. The average relaxation time $\langle \tau_l \rangle^{3D}$ of electronic phonons in a three-dimensional medium is obtained from Eq. (9) by replacing in the integrands the product $I^2(p\xi)D(\xi)$ by a unit ''step'' which vanishes for $\xi > 1$. Averages of the type $\langle \ldots \rangle_e^{3D}$ were discussed above.

Let us once again estimate the ratio S_p^{2D}/S_p^{3D}. Let $\tau_l(q) \propto q^n$ (Ref. 17). Simplifying Eq. (1) with allowance for the elasticity of the electron scattering and performing the integration where possible, we obtain

$$\frac{S_p^{2D}}{S_p^{3D}} = \frac{2(4-n)}{\pi\Gamma((5-n)/2)} \int_0^\infty dy\, e^{-y} y^{(3-n)/2} \int_0^\infty d\xi\, \xi^{3-n} I^2(\sqrt{8\theta y}\,\xi) D(\xi), \tag{10}$$

where $\theta = k_BTL^2m/\pi^2\hbar^2$ and $\Gamma(\ldots)$ is the gamma function. The ratio (10) is a function only of the single variable θ and of the parameter n ($\leqslant 3$), which determines the relaxation mechanism of the elastic subsystem. The family of curves describing this situation is displayed in Fig. 2. One can see that in the present limit the ratio S_p^{2D}/S_p^{3D} for the Simons[18] relaxation mechanism ($n = 1$) is quite large but less than for two-step drag. As we have said above, two-step drag in superlattices, in contrast to the analogous drag in three-dimensional semiconductors, should be manifested even at quite high temperatures. For this reason, the data presented in Fig. 2 determine only a lower bound on the ratio of the phonon contributions to the thermopower.

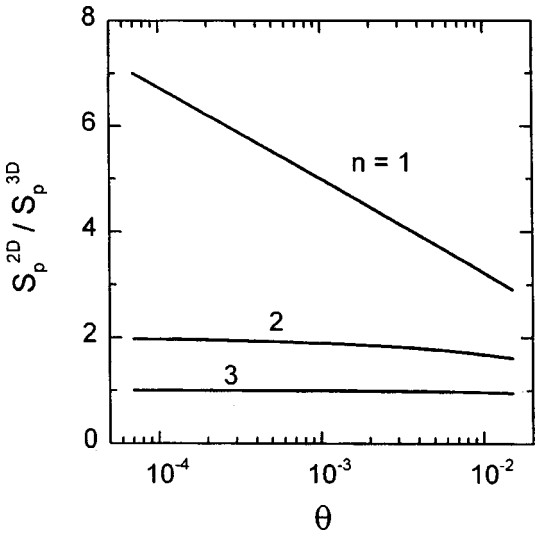

FIG. 2. Reduced thermopower of Herring drag versus the reduced temperature θ for three values of the scattering parameter n.

On this basis it follows that at low temperatures the thermopower, the electrical conductivity, and the thermoelectric figure of merit of a superlattice can be many times greater than the corresponding coefficients of a three-dimensional semiconductor. The ratio (2) differs substantially from 1 only for $T \ll 100$ K. However, phonon drag can improve the thermoelectric properties of a superlattice at liquid-nitrogen temperatures. In addition, materials with a high lattice thermal conductivity could be promising in this case (see Eq. (6)).

An increase in the drag thermopower much greater than that considered above should be observed in nanostructures with one-dimensional QWs because of the expansion of the phase volume of electronic phonons.

This work was supported by the program ''Integratsiya,'' Project No. 75.

[1)]The thermoelectric figure of merit is $Z = S^2\sigma/\kappa$, where S, σ, and κ are, respectively, the thermopower, the electrical conductivity, and the thermal conductivity of the material. This parameter determines the thermoelectric energy conversion efficiency.

[2)]Certain phonon–phonon processes, which are normal in a three-dimensional semiconductor, become umklapp processes in a superlattice (because of the small size of its Brillouin zone) into umklapp processes and can increase ν_p^R (Ref. 16). However, the additional umklapp processes lead to the relaxation only of the component of the total quasimomentum of the phonon subsystem that is transverse to the layers.

[1] L. D. Hicks and M. S. Dresselhaus, Phys. Rev. B **47**, 12727 (1993).
[2] L. D. Hicks and M. S. Dresselhaus, Phys. Rev. B **47**, 16631 (1993).
[3] L. D. Hicks, T. C. Harman, and M. S. Dresselhaus, Appl. Phys. Lett. **63**, 3230 (1993).
[4] J. O. Sofo and G. D. Mahan, Appl. Phys. Lett. **65**, 2690 (1994).
[5] D. A. Broido and T. L. Reinecke, Phys. Rev. B **51**, 13797 (1995).
[6] D. A. Broido and T. L. Reinecke, Appl. Phys. Lett. **70**, 2834 (1997).
[7] B. K. Ridley, J. Phys. C **15**, 5899 (1982).

[8] A. I. Ansel'm, *Introduction to Semiconductor Theory*, Prentice-Hall, Englewood Cliffs, N. J., 1981 [Russian original, Nauka, Moscow, 1978].
[9] L. E. Gurevich and G. M. Nedlin, Fiz. Tverd. Tela (Leningrad) **3**, 2779 (1961) [Sov. Phys. Solid State **3**, 2029 (1961)].
[10] S. M. Puri, Phys. Rev. A **139**, A995 (1965).
[11] P. S. Zyaryanov and G. I. Guseva, Usp. Fiz. Nauk **95**, 565 (1968) [Sov. Phys. Usp. **4**, 338 (1969)].
[12] V. A. Kozlov and É. L. Nagaev, JETP Lett. **13**, 455 (1971).
[13] A. A. Bel'chik and V. A. Kozlov, Fiz. Tekh. Poluprovodn. **20**, 53 (1986) [Sov. Phys. Semicond. **20**, 31 (1986)].
[14] C. Herring, Phys. Rev. **96**, 1163 (1954).
[15] R. N. Gurzhi, Usp. Fiz. Nauk **94**, 689 (1968) [Sov. Phys. Usp. **11**, 255 (1968)].
[16] Shang Yuan Ren and J. D. Dow, Phys. Rev. B **25**, 3750 (1982).
[17] C. Herring, Phys. Rev. **95**, 954 (1954).
[18] S. Simons, Proc. Phys. Soc. **83**, 749 (1964).

Translated by M. E. Alferieff

Atomic-vacancy ordering and magnetic susceptibility of nonstoichiometric hafnium carbide

A. I. Gusev* and A. N. Zyryanova
Institute of Solid-State Chemistry, Urals Branch of the Russian Academy of Sciences, 620219 Ekaterinburg, Russia

(Submitted 11 January 1999)
Pis'ma Zh. Éksp. Teor. Fiz. **69**, No. 4, 296–301 (25 February 1999)

Experimental data on the magnetic susceptibility of nonstoichiometric hafnium carbide $HfC_y (0.6<y<1.0)$ are presented. Anomalies are found in the temperature dependences of the magnetic susceptibility of the carbides $HfC_{0.71}$, $HfC_{0.78}$, and $HfC_{0.83}$ in the temperature range 870–930 K. These anomalies are due to the formation of a superstructural short-range order in their nonmetallic sublattice. It is shown that the short-range order in the carbides $HfC_{0.71}$ and $HfC_{0.78}$ corresponds to the ordered phase Hf_3C_2, while in the carbide $HfC_{0.83}$ it corresponds to the ordered phase Hf_6C_5. It is found that the magnetic susceptibility of the carbide $HfC_{0.78}$ in the temperature interval 910–980 K is zero. © *1999 American Institute of Physics.* [S0021-3640(99)00804-X]

PACS numbers: 75.30.Cr

Hafnium carbide HfC_y ($HfC_y\square_{1-y}$) possesses $B1$-type structure and a wide homogeneity range $0.6\leqslant y\leqslant 1.0$,[1] within which its nonmetallic sublattice can contain up to 40 at. % structural vacancies $\square$. Hafnium carbide is a highly nonstoichiometric compound, one of a group of compounds whose characteristic feature is the formation of a large number of diverse ordered phases.[1,2] The atomic-vacancy ordering of nonstoichiometric carbides MC_y ($MC_y\square_{1-y}$) appreciably influences their specific heat, superconductivity, and magnetic and electric-transport properties. Thus far effects due to ordering have been found in the structure and properties of all cubic nonstoichiometric carbides (TiC_y, ZrC_y, VC_y, NbC_y, TaC_y) except hafnium carbide HfC_y. Even in a recent review,[2] devoted exclusively to the effects of ordering in nonstoichiometric intercalation compounds, hafnium carbide is mentioned only in connection with theoretical calculations of order–disorder transitions.

Indeed, the carbide HfC_y has never been systematically investigated. What information does exist about the composition and temperature dependences of its properties is incomplete and 30 to 40 years old. There are no published experimental data on ordering in HfC_y.

The lack of experimental proofs of ordering of HfC_y is due to the virtual impossibility of studying directly the structure of its ordered phases by diffraction methods: In an x-ray experiment the relative intensity of possible superstructural reflections is very low because of the large difference in the scattering amplitudes of the Hf and C atoms, and in

 © 1999 American Institute of Physics

the case of neutron diffraction the neutron absorption by the massive hafnium nuclei is very large, as a result of which the total intensity of the diffraction spectrum is low and the superstructural reflections are impossible to observe. Nuclear magnetic resonance is inapplicable for investigating the distribution of atoms in the HfC_y lattice, since the nuclei of the most common isotopes ^{180}Hf, ^{176}Hf, ^{174}Hf, and ^{12}C possess zero spin.

At the same time, theoretical calculations[3] show that the disordered state of the carbide HfC_y is a thermodynamically equilibrium state only at temperatures above 800 K, while at lower temperatures the ordered phases Hf_3C_2 and Hf_6C_5 should exist.

Since it is impossible to investigate directly the ordering in nonstoichiometric carbide HfC_y by structural methods, in the present work the order–disorder transitions were studied by an indirect method using the magnetic susceptibility.

Samples of the disordered carbide HfC_y with different carbon contents ($y=0.62$, 0.71, 0.78, 0.80, 0.83, 0.87, 0.90, 0.96) were used for the investigations. The samples were obtained by solid-phase vacuum synthesis at 2200 K followed by quenching from 2200 to 300 K at a rate of 2000 K/min. All samples were homogeneous and contained a single phase with $B1$ structure. The susceptibility was measured with a highly sensitive magnetic balance, used for studying weak para- and diamagnets in fields with intensity 7.2, 8.05, and 8.8 kOe in the temperature interval 300–1250 K in a vacuum no worse than 0.001 Pa. The sensitivity of the magnetic balance is not less than 2×10^{-10} emu/g. The susceptibility of the experimental hafnium carbide samples did not depend on the magnetic field intensity. This indicates that there are no ferromagnetic impurities in them. The relative measurement error did not exceed 3%. The measurements were performed with a 1.5–2.0 h hold at each temperature to establish a constant value of χ, which remained constant in time.

The investigation of the temperature dependences $\chi(T)$ showed that as the temperature increases, the susceptibility of the carbides $HfC_{0.62}$, $HfC_{0.80}$, $HfC_{0.87}$, $HfC_{0.90}$, and $HfC_{0.96}$ increases nonlinearly without any effects attesting to phase transformations. An anomalous decrease of χ at 835–860 K, after which χ once again increases with temperature, is observed in the temperature dependences $\chi(T)$ of the carbides $HfC_{0.71}$, $HfC_{0.78}$, and $HfC_{0.83}$ (Fig. 1). According to the calculation performed in Ref. 3, the ordered phases Hf_3C_2 and Hf_6C_5, for which the transition temperatures T_{trans} are 600–800 K, depending on the composition of the disordered carbide, can form in hafnium carbide. It can be inferred that the observed anomalous decrease, followed by an increase, of the susceptibility of hafnium carbide are due to the ordering and subsequent disordering occurring during the measurements.

The typical change in the susceptibility with increasing and decreasing temperature for samples of the carbide HfC_y exhibiting an anomalous behavior of χ is shown in detail in Fig. 2. As temperature increases to 820–835 K the susceptibility of the disordered carbide $HfC_{0.71}$ increases monotonically and then decreases abruptly at $835<T<860$ K as a result of a nonequilibrium order–disorder transition, increases rapidly at 900–950 K, which corresponds to a transition from an equilibrium ordered state to an equilibrium disordered state, and once again increases slowly at $T>950-970$ K (Fig. 2, curve *1*). The susceptibility decreases monotonically as the temperature decreases from 1250 K to 900 K. In the region 900–870 K the susceptibility χ decreases abruptly as a result of a transition from an equilibrium disordered state to an equilibrium ordered state; as the

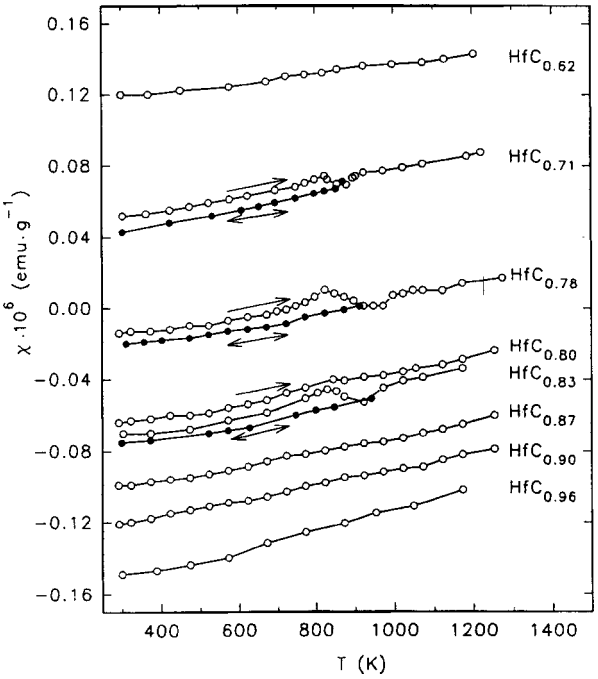

FIG. 1. Temperature dependences of the magnetic susceptibility χ of nonstoichiometric hafnium carbide HfC_y in the disordered (○) and ordered (●) states.

sample is further cooled, χ decreases. The direct and reverse temperature dependences $\chi(T)$ are virtually identical at temperatures $T>900$ K, and at $T<870-900$ K the reverse dependence $\chi(T)$ (Fig. 2, curve *2*) lies below the curve $\chi(T)$ obtained on heating (Fig. 2, curve *1*). Thus, the susceptibility χ of ordered hafnium carbide is less than that of the disordered carbide at the same temperature. During subsequent heat cycling the susceptibility follows the curve *2* (Fig. 1). The abrupt change in χ at 870–900 K corresponds to equilibrium order–disorder (on heating) or disorder–order (on cooling) phase transitions. The existence of a small hysteresis in the region of the transformation shows that the ordering in HfC_y is a first-order phase transition. The temperature dependences $\chi(T)$ of the carbides $HfC_{0.78}$ and $HfC_{0.83}$ are similar to $\chi(T)$ of the carbide $HfC_{0.71}$. The interesting experimental result that the susceptibility of the carbide $HfC_{0.78}$ is zero should be noted. The susceptibility remains zero in the interval from 910 to 980 K (Fig. 1).

Why does the magnetic susceptibility of the carbides $HfC_{0.71}$, $HfC_{0.78}$, and $HfC_{0.83}$ decrease on ordering? The measured susceptibility of nonstoichiometric carbides is a sum of the para- and diamagnetism of the atomic cores, the Pauli paramagnetism χ_p^- and Landau diamagnetism $\chi_d^- = -(m_0/m^*)^2\chi_p^-(0)/3$ of the conduction electrons (m_0 is the free-electron mass; m^* is the effective mass), and the orbital Van Vleck paramagnetism χ_{orb}. Of all the terms, only the Pauli paramagnetism is temperature-dependent, $\chi_p^-(T) = \chi_p^-(0) + bT^2$, where $\chi_p^-(0) \sim N(E_F)$ and $b \sim \partial^2 N(E_F)/\partial E^2$ (Ref. 4), which gives rise to the experimentally observed temperature dependence of the susceptibility $\chi(y,T) = a(y) + b(y)T^2$ in the interval from 300 K to the onset of the order–disorder transition.

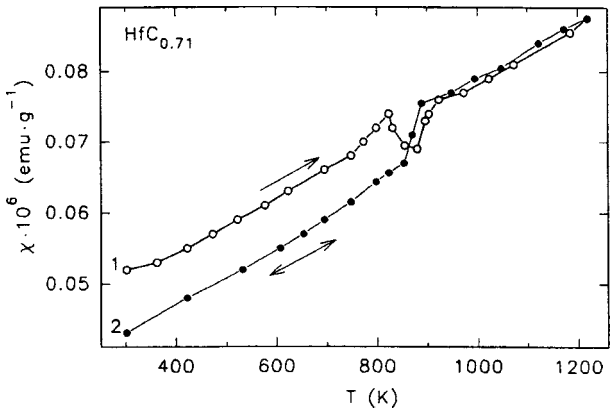

FIG. 2. Effect of ordering on the magnetic susceptibility χ of the carbide $HfC_{0.71}$: (○) variation of χ of the disordered carbide $HfC_{0.71}$ on heating, a nonequilibrium irreversible order–disorder transition at 835–860 K, and an equilibrium order–disorder transition at 890–910 K; (●) variation of χ of the carbide $HfC_{0.71}$ on cooling and an equilibrium disorder–order transition at temperature $900 \geqslant T_{\text{trans}} \geqslant 890$ K.

The susceptibility χ can decrease on ordering if $m^*_{\text{ord}} < m^*_{\text{disord}}$ or $N(E_F)_{\text{ord}} < N(E_F)_{\text{disord}}$. However, analysis of the effects due to ordering on the susceptibility of the carbides NbC_y and TaC_y (Ref. 2) showed that the change in the effective mass and the decrease in the electronic density of states at the Fermi level on ordering are too small to explain the observed decrease in χ. Therefore the most likely reason for the decrease in the susceptibility could be a change in the contribution of orbital paramagnetism as a result of the formation of superstructural short-range order,[2,5] which always arises on ordering.

The magnetic susceptibility of nonstoichiometric carbides with a $B1$ type basal structure is determined mainly by the electronic subsystem of the metal atoms. The symmetry of the nearest environment of the metal atoms in the ordered carbide is higher than in the disordered carbide, so that the contribution of the Van Vleck orbital paramagnetism to the susceptibility of the ordered carbide is smaller in magnitude than the analogous contribution to χ of the disordered carbide. The influence of the symmetry of the nearest environment on the value of χ is confirmed by a calculation of the short-range order parameters from the experimental data on the magnetic susceptibility by the method described in Ref. 2.

The crystal lattice of the nonstoichiometric carbide can be represented as a collection of clusters in the form of Dirichlet–Voronoĭ polyhedra (distorted rhombododecahedra in the case of the $B1$ type structure), which include a metal atom at the center, and six filled or vacant sites in the nonmetallic sublattice. Such clusters fill the entire volume of the crystal and they take account of all sites in the crystal lattice. The probability $P_i(y)$ of a cluster in the disordered carbide depends only on the composition y of the carbide, and it is determined by the binomial distribution. If the susceptibility $\chi(y,T) = a(y) + b(y)T^2$ of the disordered carbide is expressed in terms of the susceptibility $\chi_i = a_i + b_i T^2$ of the individual clusters as $\chi(y,T) = \Sigma \chi_i(T) \lambda_i P_i(y)$, then knowing the probability $P_i(y)$ and the experimental coefficients $a(y)$ and $b(y)$ for several disordered carbides with different carbon content, the coefficients a_i and b_i can be calculated for

each cluster (λ_i is the multiplicity of the ith configuration of the cluster). Next, using the experimental coefficients $a(y)$ and $b(y)$ for the ordered carbide, the values found for a_i and b_i and the normalization conditions $\Sigma\lambda_i P_i(y)=1$ and $\Sigma c_i\lambda_i P_i(y)=y$ (c_i is the fraction of the sites of a cluster with the ith configuration that are occupied by carbon atoms), we can calculate the probability $P_i^{\mathrm{ord}}(y)$ of clusters in the ordered carbide. We find the short-range order parameters α_1 and α_2 for the first and second coordination spheres of the carbon sublattice according to the formula

$$\alpha_j=1-(P_{\mathrm{C-\square}}^{\mathrm{ord}(j)})/(P_{\mathrm{C-\square}}^{\mathrm{bin}}), \tag{1}$$

where $P_{\mathrm{C-\square}}^{\mathrm{bin}}=\lambda_{\mathrm{C-\square}}y(1-y)$ is the binomial probability of the formation of carbon–vacancy pairs C–$\square$ ($\lambda_{\mathrm{C-\square}}=2$) that corresponds to the disordered state of the carbide MC_y and depends only on its composition. We determine the probability of the formation of C–$\square$ pairs in any jth coordination sphere of the nonmetallic sublattice of the ordered compound as

$$P_{\mathrm{C-\square}}^{\mathrm{ord}(j)}=\sum_i n_i^{(j)}\lambda_i P_i^{\mathrm{ord}}(y), \tag{2}$$

where $n_i^{(j)}$ is the relative fraction of the pairs C–$\square$ in the jth coordination sphere of a cluster with the ith configuration.

Comparing the computed values of α_1 and α_2 with the theoretical short-range order parameters[5] for all superstructures that can arise in carbides suggests the type and symmetry of the ordered phases of hafnium carbide HfC_y.

In the carbides $HfC_{0.71}$ and $HfC_{0.78}$ the parameters are $-0.21<\alpha_1<-0.13$ and $\alpha_2\cong 0$. This combination of α_1 and α_2 is possible only for an ordered phase of the type M_3C_2 with orthorhombic (space group *Immm*) or monoclinic (space group $P2$) structures. For the carbide MC_y, whose composition differs from the stoichiometric composition of the ordered phase ($y\neq y_{\mathrm{st}}$), the limiting value of the superstructural short-range order parameter in the jth coordination sphere[5] can be found from the formulas

$$\alpha_j(y,\eta_{\max})=\alpha_j(y_{\mathrm{st}},\eta_{\max})\{[y_{\mathrm{st}}(1-y)]/[y(1-y_{\mathrm{st}})]\}\ \text{ for }\ 1\geqslant y\geqslant y_{\mathrm{st}}, \tag{3}$$

$$\alpha_j(y,\eta_{\max})=\alpha_j(y_{\mathrm{st}},\eta_{\max})\{[y(1-y_{\mathrm{st}})]/[y_{\mathrm{st}}(1-y)]\}\ \text{ for }\ y_{\mathrm{st}}\geqslant y\geqslant 0. \tag{4}$$

For the carbides $HfC_{0.71}$ and $HfC_{0.78}$ upon formation of an M_3C_2 superstructure ($y_{\mathrm{st}}=2/3$) the maximum possible value of the long-range order parameter $\eta_{\max}$ is 0.87 and 0.66, respectively, and the limiting values of the superstructural short-range order parameters are $\alpha_1=-0.204$ and $\alpha_2=0$ for $HfC_{0.71}$ and $\alpha_1=-0.141$ and $\alpha_2=0$ for $HfC_{0.78}$. Comparing with them the parameters α_1 and α_2 calculated from the data on χ shows that the degree of long-range order in the carbide $HfC_{0.71}$ is close to maximum, and somewhat less than maximum in $HfC_{0.78}$.

In the carbide $HfC_{0.83}$ the parameters are $\alpha_1=-0.079$ and $\alpha_2=-0.023$. The relation $0>\alpha_2>\alpha_1$ is possible only for superstructures of the type M_6C_5 ($y_{\mathrm{st}}=2/3$). In the carbide $HfC_{0.83}$ with the maximum degree of order ($\eta_{\max}=0.995$) the parameters are $\alpha_1=\alpha_2=-0.195$. The parameters α_1 and α_2 found from the χ data are far from these values, so that the degree of ordering of the carbide $HfC_{0.83}$ is appreciably less than maximum.

The absence of any features in the temperature dependence $\chi(T)$ of the carbide $HfC_{0.83}$ (Fig. 1) probably signifies that with respect to its composition this carbide lies at the boundary of the regions of coexistence of the ordered phases Hf_3C_2 and Hg_6C_5 and therefore does not undergo ordering. To produce the possible short- or long-range order, $HfC_{0.80}$ powder was additionally annealed at 750 K for 20 h and studied by transmission electron microscopy using a JEM-200C microscope. The electron diffraction patterns of individual grains of the carbide $HfC_{0.80}$ showed only systems of point reflections from reciprocal-lattice planes of the cubic phase of HfC_y, while in the presence of short-range order periodic diffuse effects, corresponding to a complicated figure in the form of a sectioned octahedron, should appear.[6] We note that the electron diffraction patterns of $HfC_{0.80}$ did not show any indications of diffuse effects, either in the presence or absence of inelastic scattering in the form of Kikuchi lines. Thus electron diffraction analysis confirmed the absence of short- and long-range orders in the vacancy distribution in the carbide $HfC_{0.80}$.

Analysis of the data on χ and the estimates of the short-range order parameters show that a phase of the type Hf_3C_2 forms in the region of compositions from HfC_y ($0.62 < y < 0.71$) to $HfC_{0.78}$, while the existence region of the Hf_6C_5 phase is no wider than $0.80 < y < 0.87$. The temperatures of the equilibrium order–disorder transition $HfC_y - Hf_3C_2$ for the carbides $HfC_{0.71}$ and $HfC_{0.78}$ are 870–890 and 970–1000 K (Figs. 1 and 2) — these are approximately 100–110 and 220–230 K higher than the computed[3] temperatures of the order–disorder transition for $HfC_{0.71}$ and $HfC_{0.78}$.

On the whole, the investigation of the magnetic susceptibility revealed effects that are characteristic of disorder–order transitions and indicate ordering of the nonstoichiometric carbide HfC_y at temperatures below 1000 K. A calculation of the short-range order parameters confirms indirectly the formation of Hf_3C_2 and Hf_6C_5 superstructures. Judging from the data obtained, Hf_3C_2 is the main ordered phase of hafnium carbide.

This work was supported by the Russian Fund for Fundamental Research (Projects Nos. 95-02-03549a and 98-03-328565a).

*e-mail: gusev@chem.ural.ru and/or gusev@ihim.uran.ru

[1] A. I. Gusev and A. A. Rempel' *Structural Phase Transitions in Nonstoichiometric Compounds* [in Russian], Nauka, Moscow, 1988.
[2] A. A. Rempel', Usp. Fiz. Nauk **166**, 33 (1996).
[3] A. I. Gusev and A. A. Rempel, J. Phys. Chem. Solids **55**, 299 (1994); Phys. Status Solidi A **163**, 273 (1997).
[4] S. V. Vonsovskiĭ, *Magnetism*, Vols. 1 and 2, Wiley, New York, 1974 [Russian original, Nauka, Moscow, 1971].
[5] A. A. Rempel and A. I. Gusev, Phys. Status Solidi B **160**, 389 (1990).
[6] J. Billingham, P. S. Bell, and M. H. Lewis, Acta Crystallogr., Sect. A: Cryst. Phys., Diffr., Theor. Gen. Crystallogr. **28**, 602 (1972).

Translated by M. E. Alferieff

Magnetic-field-induced toroidal moment in the magnetoelectric Cr_2O_3

Yu. F. Popov,* A. M. Kadomtseva, D. V. Belov, and G. P. Vorob'ev
M. V. Lomonosov Moscow State University, 119899 Moscow, Russia

A. K. Zvezdin
Institute of General Physics, Russian Academy of Sciences, 117942 Moscow, Russia

(Submitted 18 January 1999)
Pis'ma Zh. Éksp. Teor. Fiz. **69**, No. 4, 302–306 (25 February 1999)

The appearance of a toroidal moment is observed in the magnetoelectric Cr_2O_3 in a strong magnetic field above the spin-flop transition field. This conclusion is based on the experimentally established fact that the off-diagonal components of the magnetoelectric susceptibility tensor of Cr_2O_3 contains an antisymmetric part that is dual to the toroidal moment. Therefore it has been shown that the magnetoelectric Cr_2O_3 in the spin-flop phase can be classified as a toroic. © *1999 American Institute of Physics.* [S0021-3640(99)00904-4]

PACS numbers: 75.80.+q, 75.30.Cr

It is well known that certain magnetic-symmetry point groups admit the existence of a toroidal moment **T** — a polar vector that changes sign under spatial inversion and time reversal.[1–3]

The existence of a toroidal moment is possible in many magnets possessing magnetoelectric (ME) structure with nonzero off-diagonal moments of the ME tensor.[4–6] In Ref. 7 materials admitting the existence of a toroidal moment were given the name ''toroics''. Although the problem of toroidal ordering in magnetically-ordered crystals with a definite symmetry has been discussed intensively in the scientific literature in the last ten years, experimental investigations for the purpose of observing a toroidal moment are only just beginning.[7,8]

In Ref. 8 it was proved on the basis of an experimentally established fact — the asymmetry of the off-diagonal components of the ME tensor — that a nonzero toroidal moment exists in the magnetic piezoelectric $GaFeO_3$. Using neutron diffraction data, the contributions of the magnetic and toroidal moments to the antisymmetric part of the ME tensor were distinguished and the toroidal moment was determined as $\mathbf{T} = (24,0,0)\mu_B$ Å per unit cell.

The symmetry of Cr_2O_3 also admits the existence of a toroidal moment, but it is difficult to observe because in Cr_2O_3 it can appear only in a strong magnetic field, above the spin-flop transition field. The problem is that in the absence of a field the spins in Cr_2O_3 are antiferromagnetically ordered along the *c* axis of the rhombohedral crystal. In this case the tensor of the linear ME effect contains only diagonal components, and the

 © 1999 American Institute of Physics

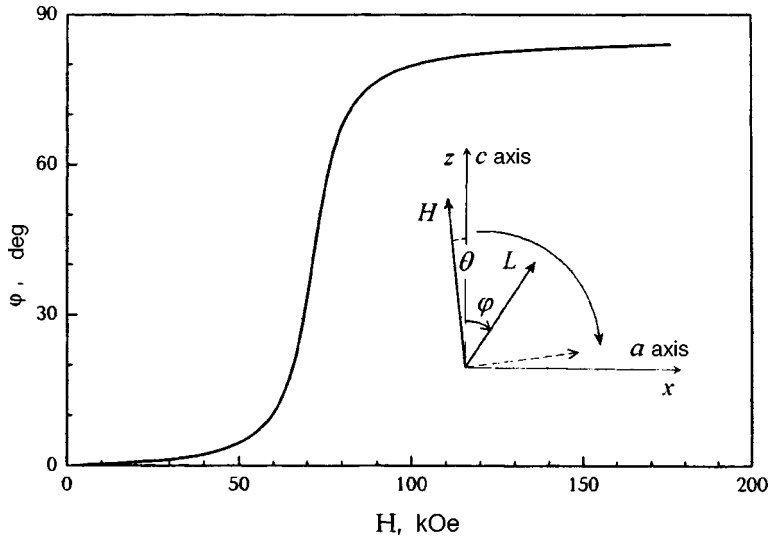

FIG. 1. Magnetic field dependence of the angle φ of the orientation of the antiferromagnetism vector **L** for $\theta=-5°$ at a temperature of 150 K.

toroidal moment of the unit cell is zero. In a sufficiently strong magnetic field $\mathbf{H}\|c$ axis the Cr^{3+} spins ''flop'' into the basal plane (spin-flop transition), and off-diagonal components of the ME tensor appear. The magnitudes and signs of these components can yield information about the existence of a toroidal moment.

The dependence of the electric polarization vector on the magnetic field **H** in the general case can be represented by the formula

$$\mathbf{P}=\hat{\alpha}\mathbf{H}, \tag{1}$$

where according to Ref. 9 the ME susceptibility tensor includes symmetric and antisymmetric parts

$$\hat{\alpha}=\hat{\alpha}^S+\hat{\alpha}^A. \tag{2}$$

The toroidal moment **T** is dual to the antisymmetric part of the matrix $\hat{\alpha}$ of the ME effect:

$$\alpha_{ij}-\alpha_{ji}=a\epsilon_{ijk}T_k, \tag{3}$$

where ϵ_{ijk} is the Levi-Civita symbol and a is a constant.

Our study of the linear ME effect in Cr_2O_3 crystals in the spin-flop phase made it possible to reveal the asymmetry of the off-diagonal components of the ME tensor and thereby to prove the existence of a toroidal moment induced by an external magnetic field.

Experimental results and discussion

The linear ME effect, induced by an external magnetic field up to 250 kOe, was investigated in Cr_2O_3 single crystals using the method described in Ref. 10. The measurements were performed on perfect crystals with no blocks. The samples were 3×3

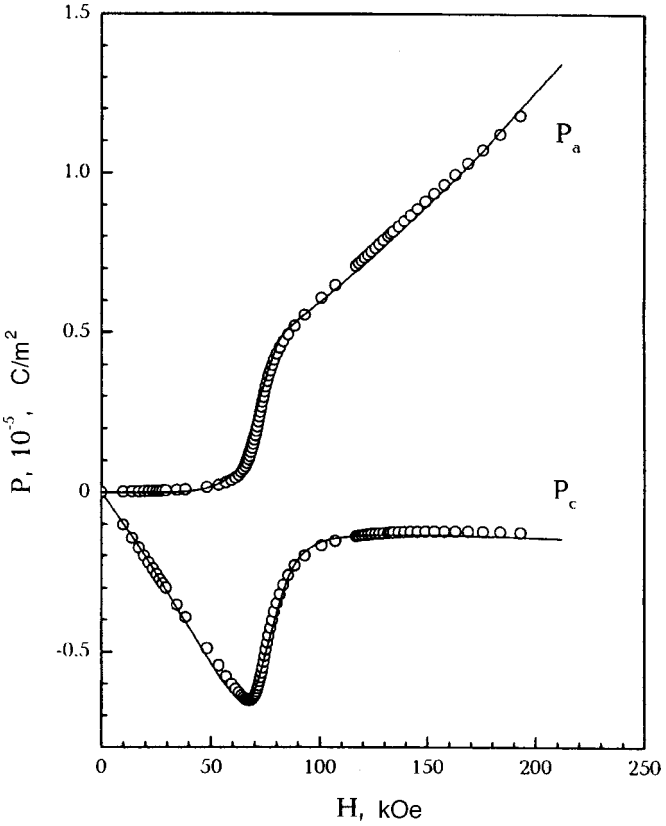

FIG. 2. Field dependence of the electric polarization P_l along the $a(x)$ and $c(z)$ axes for $\theta=-5°$ at a temperature of 150 K (solid lines — experiment, circlets — theory).

$\times 3$ mm cubes, whose edges coincided with the *a*, *b*, and *c* axes in an orthohexagonal coordinate system (*a* is one of the twofold axes in the basal plane perpendicular to the rhombohedral axis of the crystal). The crystal was oriented by the x-ray method to within 1°. The accuracy of the orientation of the field with respect to the rhombohedral *c* axis was $\pm 2°$. The electric polarization components $\mathbf{P}_a$ and $\mathbf{P}_c$ versus the pulsed magnetic field **H**, oriented at an angle $\theta=+5°(\theta=-5°)$ with respect to the *c* axis in the *ac* plane of the crystal, was measured. In this case, as the field increases, the antiferromagnetism vector **L** moves away from the *c* axis, remaining in the *ac* plane and asymptotically approaching a direction perpendicular to the field **H**, as shown in Fig. 1. This orientation of the field was chosen because for a strict orientation of the field along the *c* axis, i.e., when a pure spin-flop transition occurs, it is impossible to determine simultaneously the components α_{13} and α_{31} and to detect their symmetry associated with the existence of a toroidal moment.

The experimentally obtained dependences of the electric polarization along the *a* and *c* axes on the magnitude of the external field are presented in Fig. 2. For a prescribed orientation of the magnetic field the components of the electric polarization vector are determined by the formulas

$$P_a = \alpha_{11} H_a + \alpha_{13} H_c , \tag{4}$$

$$P_c = \alpha_{31} H_a + \alpha_{33} H_c . \tag{5}$$

One can see in Fig. 2 that as the field increases to $\sim$65 kOe the component P_a of the electric polarization increases slightly, and then in fields 65–85 kOe a sharp increase of the polarization is observed, followed by a transition to an essentially linear dependence $P_a(H)$. Such a field dependence of the electric polarization is explained by the fact that in a weak field the first term $\alpha_{11} H_a$, which makes a small contribution to the polarization because the projection of the field on the *a* axis is small, plays a determining role in the relation (4). The sharp increase of the polarization in fields 65–85 kOe is due to the ''flopping'' of the spins into the basal plane (more accurately, into a plane tilted 5° from the basal plane). The nearly linear dependence $P_c(H)$ in a weak field (the Cr^{3+} spins are almost parallel to the *c* axis) is due mainly to the first term in Eq. (5), and the sharp decrease of the polarization in fields 65–85 kOe is due to the vanishing of the component α_{33} of the ME tensor. At $H \sim 65$ kOe an off-diagonal component α_{31} (second term in Eq. (5)) appear, but its contribution is small because of the smallness of the projection of the magnetic field on the *a* axis. We note that for a given orientation of the magnetic field the rotation of the spins in a direction perpendicular to the field occurs with the field increasing not abruptly, as in the case of a strict spin-flop transition, but rather over the range 65–85 kOe.

Formula (3), which relates the toroidal moment to the antisymmetric part of the matrix $\hat{\alpha}$ of the ME effect, was used to prove the existence of a toroidal moment **T** in Cr_2O_3. The formulas for the components α_{ij} follow from the general formula for the electric polarization vector

$$\mathbf{P} = \hat{\alpha}\mathbf{H} = \chi_\perp [\mathbf{H} - (\mathbf{H}\cdot\mathbf{L})\mathbf{L}] \begin{vmatrix} \lambda_1 L_y + \lambda_3 L_z & \lambda_1 L_x & \lambda_2 L_x \\ \lambda_1 L_x & -\lambda_1 L_y + \lambda_3 L_x & \lambda_2 L_y \\ \lambda_4 L_x & \lambda_4 L_y & \lambda_5 L_z \end{vmatrix}$$
$$+ \chi_\parallel (\mathbf{H}\cdot\mathbf{L}) \begin{vmatrix} 2\lambda_1 L_x L_z + (\lambda_3 + \lambda_4) L_x L_y \\ \lambda_1 (L_x^2 - L_y^2) + (\lambda_3 + \lambda_4) L_y L_z \\ \lambda_2 (L_x^2 + L_y^2) + \lambda_5 L_z^2 \end{vmatrix} , \tag{6}$$

obtained in Ref. 11 from the thermodynamic potential[12] given by

$$\Phi_{\mathrm{ME}} = -\lambda_1 [m_x (L_x E_y + L_y E_x) + m_y (L_x E_x + L_y E_y) - \lambda_2 (L_x m_x + L_y m_y) E_z - \lambda_3 (m_x E_x + m_y E_y) L_z - \lambda_4 m_z (L_x E_x + L_y E_y) - \lambda_5 m_z L_z E_z . \tag{7}$$

In these formulas **E** and **H** are the electric and magnetic field intensities; **m** and **L** are the weak ferromagnetism and antiferromagnetism vectors; $\chi_\parallel$ and $\chi_\perp$ are the longitudinal and transverse magnetic susceptibilities; and, λ_k are constant coefficients. Specifically, the components α_{13} and α_{31} were calculated in this work. These components were used to estimate the component T_2 of the toroidal moment (the values 1, 2, and 3 of the index *i* correspond to the coordinate axes $x, y,$ and z in the direction of the crystallographic axes $a, b,$ and c). In our case these components are determined by the formulas

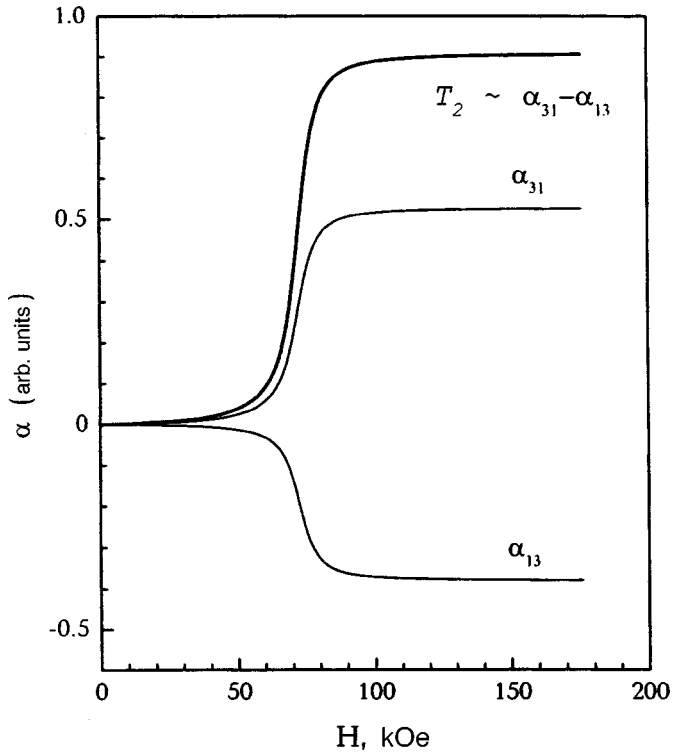

FIG. 3. Magnetic field dependence of the components of the ME susceptibility tensor α_{13}, α_{31}, and $T_2 \sim \alpha_{31} - \alpha_{13}$ in arbitrary units at a temperature of 150 K.

$$P_a = H[\sin\theta[\chi_\perp(\lambda_2-\lambda_5)\sin\varphi\cos^2\varphi + \chi_\parallel \sin\varphi(\lambda_2\sin^2\varphi + \lambda_5\cos^2\varphi) + \cos\theta[\chi_\perp(\lambda_5-\lambda_2)\cos\varphi\sin^2\varphi + \chi_\parallel\cos\varphi(\lambda_2\sin^2\varphi + \lambda_5\cos^2\varphi)]], \quad (8)$$

$$P_c = H[\sin\theta[\chi_\perp(\lambda_3\cos^3\varphi - \lambda_4\sin^2\varphi\cos\varphi) + \chi_\parallel(\lambda_3+\lambda_4)\sin^2\cos\varphi] + \cos\theta[\chi_\perp(-\lambda_3\sin\varphi\cos^2\varphi + \lambda_4\sin^3\varphi) + \chi_\parallel(\lambda_3+\lambda_4)\sin\varphi\cos^2\varphi]],$$

where φ is the angle between the vector **L** and the c axis, and θ is the angle between **H** and the c axis. The angle φ as a function of the field intensity H is given by[13]

$$H = H_P\sqrt{\sin 2\varphi/\sin 2(\varphi-\theta)}, \quad (9)$$

where H_P is the threshold field of the spin-flop transition with the field oriented strictly along the c axis ($\theta=0$). A plot of the function $\varphi(H)$ with $\theta=-5°$ and at temperature 150 K is presented in Fig. 1. The value $H_P=72$ kOe was taken from our experiments.

The theoretical curves of the field dependences $P_a(H)$ and $P_c(H)$, obtained from Eq. (8) with the use of relation (9) and the value $\chi_\perp/\chi_\parallel=3.1$ taken from Ref. 13, were compared with the corresponding experimental curves, and the coefficients λ_3 and λ_4 (from the $P_a(H)$ curves) and λ_2 and λ_5 (from the $P_c(H)$ curves) were determined, to within a constant factor, so as to obtain the best fit. The solid lines in Fig. 2 show the

experimental curves and the circlets show the theoretical results with the values found for λ_k. The good agreement between the experimental and theoretical results attests to the adequacy of the theoretical model adopted.

The magnetic field dependences of the matrix elements α_{31} and α_{13} and their difference $\alpha_{31}-\alpha_{13}\sim T_2$ (in arbitrary units) for the angle $\theta=-5°$ are represented in Fig. 3.[1)] It is evident from the figure that the nonzero antisymmetric part $(\alpha_{31}-\alpha_{13})$ and togetherwith it the component T_2 appear as soon as the spins depart from the *c* axis (this already follows from the fact that α_{13} and α_{31} have different signs) and remain right up to the spin-flop phase. This gives a basis for classifying the magnetoelectric Cr_2O_3 in the spin-flop phase as a toroic.

In summary, we have established on the basis of measurements in a strong magnetic field up to 250 kOe of the electric polarization of a Cr_2O_3 crystal along the *a* and *c* axes that the off-diagonal components α_{13} and α_{31} of the magnetoelectric susceptibility tensor have different signs. Asymmetry of the components of the ME susceptibility tensor of Cr_2O_3 in the spin-flop phase attests to the presence of a nonzero toroidal moment, admitted by the symmetry of these crystals.

We thank Yu. V. Kopaev for a helpful discussion and H. Schmid for his steady interest. This work was supported by the Russian Fund for Fundamental Research (Grants Nos. 98-02-16848 and 96-15-96429).

*e-mail: Popov@plms.phys.msu.su

[1)]We note that when the sign of the tilt angle of the field changes, $\theta\rightarrow-\theta$, so does the sign of the angle φ, and at the same time the signs of both components α_{13} and α_{31} also change, as one can see from Eq. (8). The relative difference of the signs of the components α_{13} and α_{31}, i.e., the asymmetry of the ME tensor is, of course, maintained.

[1] H. Schmid, Int. J. Magn. **4**, 337 (1973).
[2] V. M. Dubovik, S. S. Krotov, and V. V. Tugushev, Kristallografiya **32**, 540 (1987) [Sov. Phys. Crystallogr. **32**, 314 (1987)].
[3] E. Ascher, in *Magnetoelectric Interaction Phenomena in Crystals*, edited by A. Freeman and H. Schmid, New York, 1975, p. 69.
[4] Yu. I. Sirotin and M. P. Shaskol'skaya, *The Fundamentals of Crystallography*, Nauka, Moscow, 1975.
[5] V. L. Ginsburg, A. A. Gorbatsevich, Yu. V. Kopaev, and B. A. Volkov, Solid State Commun. **50**, 339 (1987).
[6] A. A. Gorbatsevich and Yu. V. Kopaev, Ferroelectrics **161**, 321 (1994).
[7] D. G. Sannikov and I. S. Zheludev, Fiz. Tverd. Tela (Leningrad) **27**, 1369 (1985) [Sov. Phys. Solid State **27**, 826 (1985)].
[8] Yu. F. Popov, A. K. Zvezdin, A. M. Kadomtseva *et al.*, Zh. Éksp. Teor. Fiz. **114**, 263 (1998) [JETP **87**, 146 (1998)].
[9] L. A. Shuvalov and N. V. Belov, Kristallografiya **7**, 162 (1962) [Sov. Phys. Crystallogr. **7**, 203 (1962)].
[10] Yu. F. Popov, A. K. Zvezdin, G. P. Vorob'ev, and A. M. Kadomtseva, JETP Lett. **57**, 69 (1993).
[11] D. V. Belov, G. P. Vorob'ev, A. M. Kadomtseva *et al.*, JETP Lett. **58**, 579 (1993).
[12] E. A. Turov, *Kinetic, Optical, and Acoustic Properties of Antiferromagnets* [in Russian], Sverdlovsk, 1990.
[13] S. Foner, Phys. Rev. **130**, 183 (1963).

Translated by M. E. Alferieff

Skin effect and response of semiconductor barrier structures*

M. N. Feĭginov[1)] and V. A. Volkov[2)]
Institute of Radio Engineering and Electronics, Russian Academy of Sciences, 103907 Moscow, Russia

(Submitted 19 January 1999)
Pis'ma Zh. Éksp. Teor. Fiz. **69**, No. 4, 307–312 (25 February 1999)

The problem of the skin effect in a finite-width barrier structure of the type conductor (metal or semiconductor) — barrier (specifically, tunneling) — conductor is solved. It is shown that the excitation of special ''barrier'' plasma polaritons (BPPs), which are localized in the barrier and the near-barrier region and possess a 2D spectrum, is possible in this regime. An analytical relation between the BPP spectrum and the linear dynamical impedance of the structure as well as its rectifying characteristics is found. The excitation of BPPs greatly increases the nonlinear response of the structure. It is shown that the linear and nonlinear response of the typical semiconductor tunneling structures in the THz frequency range is determined by the excitation of BPPs. © *1999 American Institute of Physics.* [S0021-3640(99)01004-X]

PACS numbers: 73.25.+i, 71.36.+c, 73.40.Gk

At high frequencies current is expelled from a conductor and flows along the surface in a skin layer. The solution of this problem is presented in textbooks.[1] Let us now consider a structure of the type conductor — poorly conducting barrier — finite-cross section conductor, through which a quite high-frequency current flows (across the barrier). It is obvious that far from the barrier the current is concentrated in the lateral skin layer. However, the spatial distribution of the current near the barrier is not understood, even qualitatively; specifically, it is not known whether or not the current flows along the barrier. This problem arises, for example, in the investigation of the impedance and nonlinear response of semiconductor tunneling structures at frequencies 100 GHz and higher. For definiteness, in the present letter we shall examine this specific situation. The problem is nontrivial because it is necessary to take account of the special gapless mode of surface plasmons,[2–5] which propagates along the barrier. Electromagnetic retardation is important under skin-effect conditions, so that we shall call this mode a barrier plasma polariton (BPP). Thus the initial aim of this work is to solve the problem of the skin effect for the above-indicated conducting structures with a barrier.

The BPP is the analog of an ordinary TEM mode in a flat, non-simply-connected waveguide (or a strip line[6]). In our case, however, the BPP fields penetrate into the conductor to a depth which is large compared with the barrier thickness. At the frequencies of interest to us, which are low compared with the volume plasma frequency ω_p of

 © 1999 American Institute of Physics

the conductor, the effective permittivity is large in absolute magnitude, and if the barrier thickness is sufficiently small, the BPP velocity is small compared with the velocity of light in the barrier material. Therefore it should be expected that the excitation of BBPs by an external source can become nonnegligible even at frequencies such that the wavelength of the source radiation is large compared with the dimensions of the structure.

The BPPs have a two-dimensional dispersion law $\omega(\mathbf{q})$, where $\mathbf{q}=(q_x,q_y,0)$ is the 2D wave vector in the barrier plane. They can be excited only under the influence of a lateral irregularity. In the situation under study, such an irregularity arises when the skin depth becomes less than the lateral dimensions of the structure.

This letter is organized as follows. First, the BPP spectrum in a semiconductor tunneling structure is derived and analyzed. Then the contribution of BPPs to the linear dynamical impedance is studied. Finally, the rectification coefficient due to the BPPs in the THz range is studied.

BPP spectrum. Consider a barrier ($z\leqslant d/2$) with differential conductance G and surrounded by a semiconductor ($z\geqslant d/2$). The conduction mechanism in the barrier can be arbitrary. For definiteness we shall assume that it is due to tunneling. Then, a smooth ($qd\ll 1$) fluctuation of the current $\mathbf{j}_T(x,y,t)=(0,0,j_T)$ through the barrier is related with G by Ohm's law

$$j_T(x,y,t)=-G[\xi(x,y,d/2+0,t)-\xi(x,y,-d/2-0,t)], \tag{1}$$

where $\xi(\mathbf{r},t)$ is the local electrochemical potential. We shall solve the linearized system of Maxwell's equations, containing the contribution (1), and the hydrodynamic equation of motion with the standard boundary conditions on the electromagnetic field and continuity of the current at the barrier. The BPP spectrum consists of two branches, in which the charge distribution is symmetric and antisymmetric relative to the central plane $z=0$. We shall confine our attention to the dispersion relation for the lowest-frequency (antisymmetric) mode:

$$(\omega+i\nu)(\omega+i\nu_T)\kappa=\omega_p^2\frac{d^*}{2}\left(\kappa^2-\frac{\omega_p^2}{c^{*2}}\frac{\omega}{(\omega+i\nu)}-\frac{\omega(\omega+i\nu_T)}{c^{*2}}\right),\quad \mathrm{Re}\ \kappa>0, \tag{2}$$

where $d^*=d+2r_{TF}$ is the effective barrier thickness, r_{TF} is the Thomas–Fermi screening length, $\nu_T=4\pi G d^*/\epsilon_l$ is the reciprocal of the RC tunneling relaxation time, ν is the reciprocal of the momentum relaxation time, ϵ_l is the lattice permittivity (it is assumed that $\epsilon_l(z)=\mathrm{const}$), $c^*=c/\sqrt{\epsilon_l}$ is the velocity of light in the barrier, $\epsilon_s=\epsilon_l[1-\omega_p^2/\omega(\omega+i\nu)]$ is the permittivity of the semiconductor in the Drude model, κ is the complex damping rate of the BPP fields into the interior of the semiconductor, and

$$\kappa^2=q^2-\epsilon_s\omega^2/c^2. \tag{3}$$

Equation (2) was derived under the conditions

$$\max\{|\nu_T|,\omega,\nu\}\ll\omega_p \quad \text{and} \quad q\ll\max\{1/d,1/r_{TF}\}. \tag{4}$$

We introduce the skin depth $l_s(\omega)$

$$\frac{1}{l_s}=\frac{\omega_p}{c^*}\mathrm{Re}\sqrt{\frac{\omega}{\omega+i\nu}}. \tag{5}$$

Analysis of Eq. (2) shows that the BPP velocity (ω/q) is indeed low compared with the velocity of light in the barrier (c^*), if $l_s(\omega) \gg d^*$. We shall present an asymptotic expression for the BPP spectrum and the damping rate κ:

a) In the long-wavelength limit ($|ql_s| \ll 1$)

$$q \approx \frac{\omega}{c^*}\sqrt{\frac{2c^*}{d^*\omega_p}}\left(\frac{\omega+i\nu}{\omega}\right)^{1/4}, \tag{6}$$

$$\kappa \approx \frac{\omega_p}{c^*}\sqrt{\frac{\omega}{\omega+i\nu}}. \tag{7}$$

An upper limit on ω follows from the condition of applicability of these expressions:

$$\left|\frac{\omega(\omega+i\nu)^3}{\nu^4}\right| \ll \left[\frac{\omega_p^2}{\nu^2}\frac{d^*\omega_p}{c^*}\right]^2. \tag{8}$$

This limit is characterized by a large retardation contribution to the BPP spectrum.

b) In the short-wavelength limit ($|ql_s| \gg 1$) $\kappa \approx q$, retardation is negligible and the dispersion relation

$$(\omega+i\nu)(\omega+i\nu_T)\kappa = \omega_p^2\frac{d^*}{2}|q| \tag{9}$$

agrees with the results obtained in Refs. 3 and 4.

Dynamic impedance. Let us consider the following structure: metal ($z \leqslant -L-d/2$) — semiconductor of finite dimensions ($2W$ along the x axis, ∞ along the y axis, and L along the z axis) — barrier ($|z| < d/2$) — semiconductor ($2W \times \infty \times L$) — metal ($z \geqslant L+d/2$). In the case of a strong skin effect ($l_s(\omega) \ll W, L$) the total impedance of the structure (per unit length along the y axis) has two contributions

$$Z = Z_s + Z_j. \tag{10}$$

Here Z_s is the ordinary impedance of the skin layer on the lateral surface of the semiconductor

$$Z_s = 4\pi i\kappa_s L/\omega\epsilon_s, \tag{11}$$

where $\kappa_s^2 = -\epsilon_s\omega^2/c^2$, and Z_j is the desired impedance of the near-barrier region ($|z| \lesssim d^*/2$).

Switching to calculations of the impedance Z_j of the tunneling junction, we note that the field and charge distributions near the barrier correspond to those in a BPP, since this is the only mode that can penetrate from the edge of the structure along the x axis to a depth greater than l_s. Therefore it is necessary to solve the problem of finding the BPP with a prescribed real frequency ω (the wave number of the BPP becomes complex $q(\omega) = q' + iq''$) and definite boundary conditions at $x = \pm W$. In the present case the charge distribution is symmetric relative to the $x = 0$ plane, so that as boundary conditions we take a definite value of the voltage drop across the barrier ($V = V(+W) = V(-W)$). Then the tunneling current density forms a standing wave

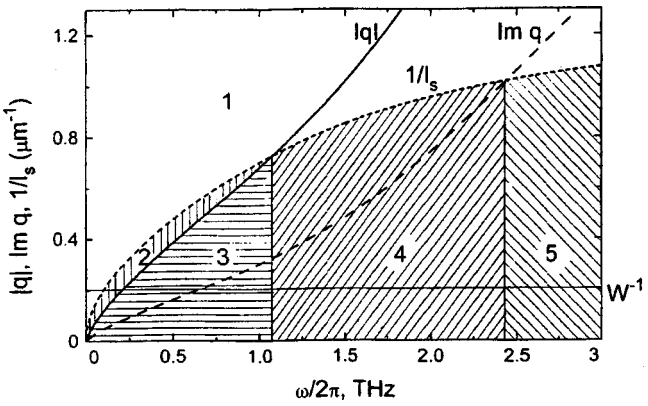

FIG. 1. Graphical determination of the regions *1–5* in which various BBP excitation regimes operate (the parameters are given in the text). The corresponding frequency ranges are determined by the intersection of these regions with the horizontal straight line $1/W=\text{const}$ (here the width of the structure $2W=10\mu\text{m}$).

$$j_T(x)=j_T(W)\frac{\cos(qx)}{\cos(qW)}. \tag{12}$$

From the preceding section we find the BPP current density $j_x(x,z)$ and match it with the total current J (per unit length on the y direction) flowing toward the barrier along the lateral surfaces with $x=\pm W$: $J/2=\int j_x(W,z)dz$. A calculation of the impedance gives the result

$$Z_j\equiv V/J=\frac{i}{C(\omega+i\nu_T)}\frac{qW}{\tan(qW)}, \tag{13}$$

where $C=\epsilon_l W/2\pi d^*$.

The frequency dependence $Z_j(\omega)$ is, generally speaking, of a multiresonance character. But at low frequencies, where $|qW|\ll 1$, expression (13) reduces to the standard expression for the impedance of a barrier:

$$Z_j=i/C(\omega+i\nu_T). \tag{14}$$

In the case of very high frequencies, where $q''W>1$, the expression for Z_j likewise simplifies

$$Z_j=\frac{2\pi q d^*}{(\omega+i\nu_T)\epsilon_l}. \tag{15}$$

In the case the function $\tan(qW)$ stops oscillating, and $Z_j(\omega)$ behaves monotonically.

There exists a definite range of values of the signal frequencies ω and the quantities W for which the nonuniform field distribution along the barrier must be taken into account and at the same time the results obtained are applicable. It is convenient to represent this region graphically using the plots $|q(\omega)|, q''(\omega)$, and $1/l_s(\omega)$ (see Fig. 1). The horizontal straight line $1/W=\text{const}$ can intersect five regions, each of which should satisfy the inequalities (4).

In region *1* (unshaded in Fig. 1) the skin depth l_s is large compared to W, and the field and current distributions in the barrier plane are uniform. In this region there is no skin effect and the standard Eq. (14) for the impedance of the junction can be used.

In region *2* (vertical hatching in Fig. 1) the skin effect is nonnegligible, but the field, current, and charge distributions at the semiconductor–barrier boundary are uniform, since

$$|q|W<1. \tag{16}$$

The current flows along the skin layer along the barrier. In this region BPPs are not excited, and the impedance is determined by expression (14).

In region *3* (horizontal hatching) the inequality (16) breaks down, and the excitation of BPPs plays the determining role. Expression (13) holds for the impedance. The currents in the near-barrier region are concentrated in the skin layer and along the barrier they penetrate to depth $1/q''$ from the lateral boundary of the structure.

In region *4* (oblique hatching with positive slope) the condition for a strong skin effect no longer holds (the BPP wavelength becomes less than the skin depth). BPP excitation by the current flowing in along the skin layer should be less efficient than in region *3*. BPPs should still be excited, but Eq. (13) is not valid. The penetration depth of the currents into the semiconductor from the barrier is $1/|q|$, and along the barrier currents penetrate to depth $1/q''$ from the sides of the structure.

In region *5* (oblique hatching with a negative slope) the current flowing up to the barrier along the lateral surface of the semiconductor along the skin layer does not penetrate along the barrier into the interior of the structure, since $l_s q''>1$. An accurate calculation is likewise difficult to perform in this region, but qualitatively the impedance should be described by Eq. (14), where l_s plays the role of W.

In this work specific calculations were performed for a structure based on *n*-GaAs ($n_0=3\times10^{18}$ cm^{-3}, $\epsilon_l=13.5$, mobility $\mu=2\times10^3$ cm^2/V·s) with a nonconducting barrier ($d=30$ nm, $\epsilon_l=13.5$). The thickness of the ''top'' semiconductor layer is assumed to be large compared with the thickness of the skin layer at frequencies such that BBPs determine the response of the structure.

Figure 2 shows the effect of BPP excitation on the impedance $Z_j(\omega)=Z_j'(\omega)+iZ_j''(\omega)$ of barrier structures with different widths. At THz frequencies the impedance differs qualitatively and quantitatively from the classical impedance of a capacitor (in the BPP approximation these impedances should be the same). As the width of the structure decreases, BPPs start to appear at higher frequencies, as expected (see Fig. 1).

The results can be easily extended to the case of structures with a Schottky barrier. Since a BPP is antisymmetric relative to the barrier center, the plane $z=0$ is an equipotential and it can be assumed to be ideally conducting. For this reason, the doubled impedance of the Schottky barrier (metal–barrier–semiconductor) equals the impedance of the structure considered above, but with a barrier whose thickness and resistance are two times greater than for a Schottky barrier.

Weak-signal nonlinear response. We shall now consider the effect of BPPs on the rectification of an ac current on a semiconductor structure with a barrier whose conduc-

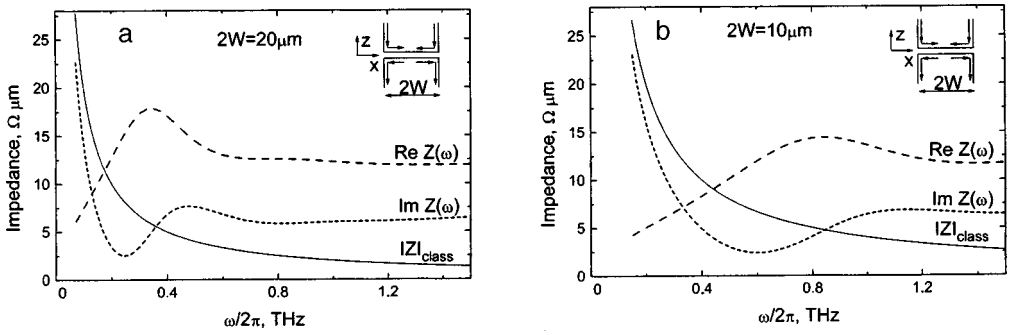

FIG. 2. Frequency dependence of the impedance (per unit length along the y axis) with BPP excitation taken into account, for barrier structures of width (along the x axis) 20 μm (a) and 10 μm (b). The parameters are given in the text. The impedance $i/\omega C$ of a classical capacitor is presented for comparison. Insets: Schematic diagram of the current distribution near the barrier.

tivity is weakly nonlinear. We give the dependence of the local voltage $V(x,t)$ across the barrier on the local current density $j_T(x,t)$ as

$$V(x,t)=j_T(x,t)/G+\alpha|j_T(x,t)|^2. \tag{17}$$

The smallness of the nonlinearity coefficient α makes it possible to use an iteration procedure to calculate the nonlinear contribution to $V(x,t)$. Using Eq. (12) and averaging expression (17) over t and x, we obtain the rectified voltage at zero frequency

$$\overline{V}=V_{\text{rect}}^{\text{classic}}(\omega)f[q(\omega)], \tag{18}$$

where

$$V_{\text{rect}}^{\text{classic}}(\omega)=\frac{1}{2}\frac{\alpha}{(2W)^2}|I|\left(1+\frac{\omega C}{2WG}\right)^{-1} \tag{19}$$

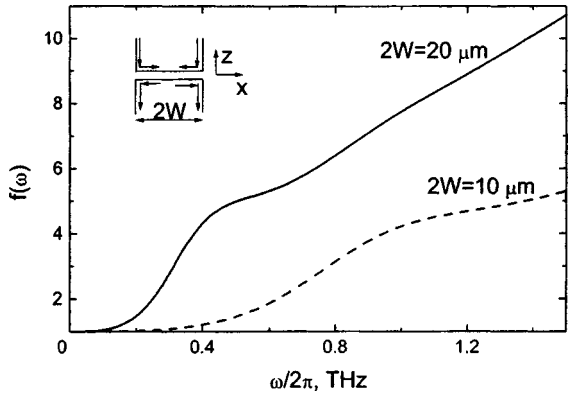

FIG. 3. Gain of the rectified voltage for two barrier structures differing in the width $2W$ (the parameters are given in the text).

is the standard expression for the rectified voltage neglecting BPPs; I is the amplitude of the rf current through the structure per unit length in the y direction. The factor

$$f(q)=\left|\frac{qW}{\sin(qW)}\right|^2\left[\frac{\sin(2q'W)}{4q'W}+\frac{\sinh(2q''W)}{4q''W}\right] \tag{20}$$

is the gain of the rectified voltage as a result of excitation of BPPs with a complex wave number. It follows from Fig. 3 that the factor $f(\omega)$ is different from 1 at high frequencies ($|q|W>1$), which for the parameters employed (see above) corresponds to THz range. The gain is progressively greater for wider structures and higher frequencies. BPP excitation can increase by an order of magnitude the rectified voltage on the barrier structure.

This work was partially supported by the Russian Fund for Fundamental Research (Project No. 99-02-17592), the INTAS–RFFI (Projects Nos. 95-0849 and 97-11475), and the Interdisciplinary Science and Technology Program ''Physics of Solid-State Nanostructures'' (No. 96-1019).

*This paper is dedicated to the celebration of the 70th birthday of V. B. Sandomirskiĭ, who was a teacher of one of the authors (V. V.).

[1)]e-mail: misha@mail.cplire.ru
[2)]e-mail: VoVa@mail.cplire.ru

[1] L. D. Landau and E. M. Lifshitz, *Electrodynamics of Continuous Media*, Pergamon Press, New York [Russian original, Nauka, Moscow, 1989].
[2] Z. Szentirmay, Prog. Quantum Electron. **15**, 175 (1991).
[3] V. I. Tal'yanskiĭ, Zh. Eksp. Teor. Fiz. **101,** 1846 (1992) [Sov. Phys. JETP **74**, 986 (1992)].
[4] S. A. Mikhaĭlov and V. A. Volkov, JETP Lett. **61**, 524 (1995).
[5] N. A. Savost'yanova and V. B. Sandomirsky, Semicond. Sci. Technol. **8**, 185 (1993).
[6] L. A. Vaĭnshteĭn, *Electromagnetic Waves* [in Russian], Radio i Svyaz', Moscow, 1988.

Translated by M. E. Alferieff

Observation of a hybridization gap in cyclotron resonance spectra of semimetallic InAs/GaSb quantum wells

Yu. B. Vasil'ev,* S. D. Suchalkin, S. V. Ivanov, P. S. Kop'ev, and B. Ya. Mel'tser
A. F. Ioffe Physicotechnical Institute, Russian Academy of Sciences, 194021 St. Petersburg, Russia

K. von Klitzing
Max-Planck-Institut für Festkörperforschung, 70569 Stuttgart, Germany

(Submitted 20 January 1999)
Pis'ma Zh. Éksp. Teor. Fiz. **69**, No. 4, 313–317 (25 February 1999)

Splitting of the cyclotron resonance (CR) line is observed in the electron CR spectra of InAs/GaSb heterostructures containing tunneling-coupled electron and hole layers. This splitting is interpreted to be a manifestation of a hybridization gap arising as a result of anticrossing of the Landau levels of electrons and holes when their wave functions overlap. The energy splitting of the CR lines is correlated with the magnitude of the overlap and agrees with theoretical estimates of the hybridization gap width. © *1999 American Institute of Physics.* [S0021-3640(99)01104-4]

PACS numbers: 76.40.+b, 73.40.Kp

Effects due to overlapping of the wave functions of the conduction-band states of InAs and valence-band states of GaSb are observed in InAs/GaSb quantum wells containing close-lying two-dimensional electronic (in the InAs) and hole (in the GaSb) layers.[1,2] Alterelli has shown[3] that a gap, called a hybridization gap, should appear in the energy spectrum of the system at places where the electron and hole dispersion curves intersect. In a perpendicular magnetic field, a hybridization gap will appear when the Landau energy levels of the electrons and holes for which resonance tunneling conditions are satisfied, are equal to each other.[4] Experimental confirmation of the presence of such a gap in the electron density of states in semimetallic InAs/GaSb quantum wells has been obtained recently in magnetotransport and magnetocapacitance measurements,[5,6] but there have been no published reports of the observation of a hybridization gap by optical methods. The present work is devoted to an investigation of the hybridization gap in the energy spectra of electrons in binary electron–hole systems by far-IR spectroscopy in a magnetic field.

The main experimental results were obtained for two samples (samples 1 and 2) in which strong oscillations of cyclotron absorption, attesting to hybridization of the conduction-band states of InAs and valence-band states of GaSb, were observed previously.[7] The samples, grown by molecular-beam epitaxy, consisted of a single InAs

 © 1999 American Institute of Physics

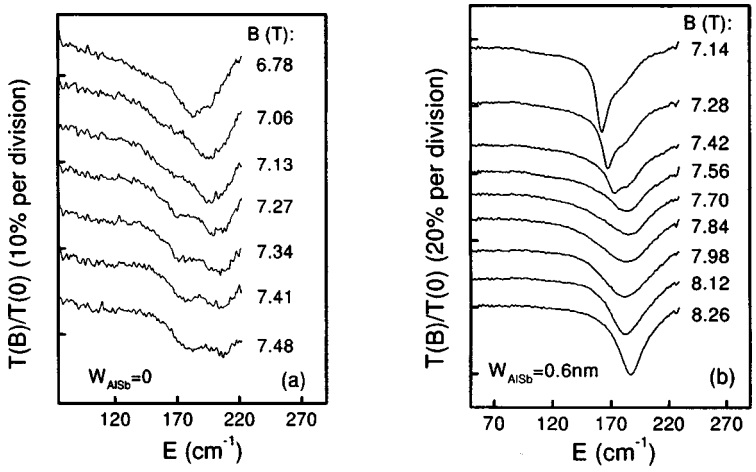

FIG. 1. Absorption spectrum of an InAs/AlSb/GaSb quantum well with different values of the magnetic field and two values of the AlSb barrier thickness: a) $b=0$ Å and b) $b=6$ Å.

quantum well 200 Å thick, placed between two GaSb layers. In sample 1 the InAs and GaSb layers directly adjoined one another. In sample 2 an AlSb barrier 6 Å thick was placed between the InAs and GaSb layers. The results obtained for two samples with barriers 20 Å and 100 Å thick (samples 3 and 4, respectively), which were previously shown not to exhibit hybridization effects,[7] were used for comparative analysis. The experiments were performed in a 2–10 T perpendicular magnetic field at temperature 2.2 K using a Fourier spectrometer.

Detailed investigations of the cyclotron resonance (CR) spectra of electrons in samples with tunneling-coupled electron–hole layers (samples 1 and 2) showed that together with strong cyclotron absorption oscillations, which were reported previously,[7] splitting of the CR line is also observed in a certain range of magnetic fields (Fig. 1). In sample 2 (Fig. 1b) an additional peak appears on the high-energy side of the main CR line and is seen only after the sample is illuminated with a red LED, which decreases the electron density in the well. In sample 1 an additional peak appears on the low-energy side of the main peak, and additional illumination with an LED does not affect the form of the spectra. We note that in both samples additional peaks appear in magnetic fields in which the electron CR lines are strongly broadened. Figure 2 shows the energy of the cyclotron absorption line versus the magnetic field. Strong oscillations of the position of the peak as a function of the magnetic field and the appearance of a second peak are observed more clearly in sample 1, even though the amplitude of the peak in this sample is much smaller. It is evident that in both samples oscillations of the effective cyclotron mass occur near $m=0.04m^*$. The smallest splitting of the CR line is approximately 3.5 meV for a sample with no barriers and 1.3 meV for a sample with a 6 Å barrier.

Splittings of the CR line are also observed in structures where the degree of admixing of the electron and hole states is negligible and hybridization effects do not appear. Figure 3 shows the magnetic field dependence of the energy of the CR peak for samples 3 and 4. In these samples the appearance of splittings of the CR line is periodic as a

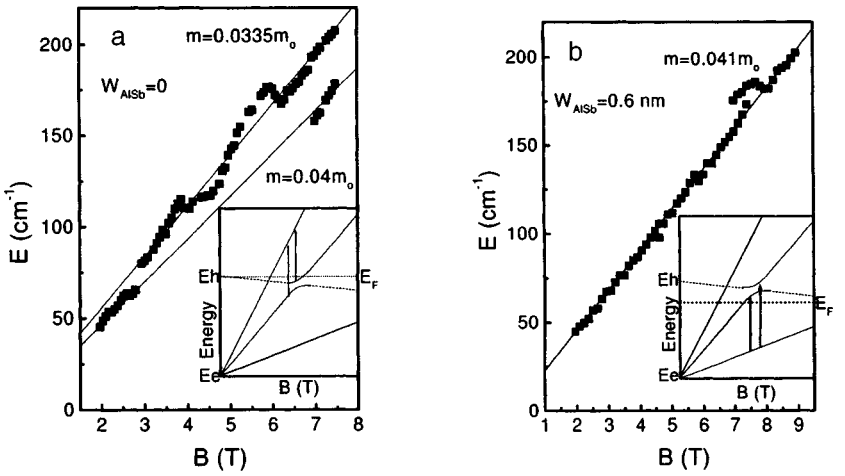

FIG. 2. Spectral positions of the CR lines measured for two samples with tunneling-transparent barriers: a) $b=0$ Å and b) $b=6$ Å. Inset: Qualitative behavior of electron (solid lines) and hole (dotted lines) Landau levels under electron–hole hybridization conditions (one level crossing is shown) and possible cyclotron transitions that can be used for observation of a hybridization gap.

function of the reciprocal of the magnetic field and is due to the filling of Landau levels, i.e., it is correlated with the position of the Fermi level.

To explain the difference in the character of the splitting of the CR lines for samples 1, 2 and 3, 4 it is necessary to examine the behavior of the Fermi level in both cases. When the layers are separated by barriers which have a substantial thickness (in our case 20 Å and more) and are not tunneling transparent, any interlayer carrier transitions and, correspondingly, changes in the carrier density in the layers produce a change in the interlayer electric field and an additional voltage drop across the barrier. As the magnetic field changes, the Landau energy levels change, which results in carrier redistribution between the layers. Estimates show that a negligible change in the density (in our samples, it does not exceed several percent of the carrier density in each layer) is suffi-

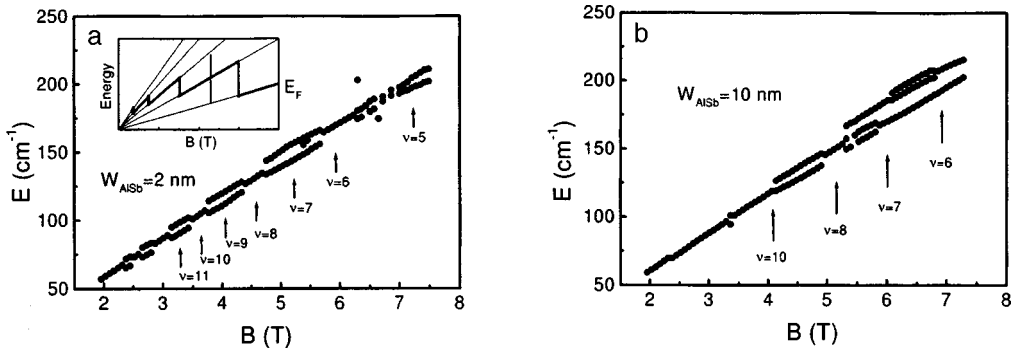

FIG. 3. Spectral positions of CR lines measured for two samples with no hybridization: a) $b=20$ Å and b) $b=100$ Å. Inset: Qualitative behavior of the Fermi level and possible cyclotron transitions.

cient to compensate, on account of the voltage drop across the barrier, the shift of the Landau levels relative to one another. This means that the upper filled Landau levels in neighboring layers become aligned, i.e., their energies coincide with one another and with the Fermi level irrespective of the magnitude of the magnetic field. Then, to a good approximation, the charge carrier density in the layers can be taken as constant. If there is no barrier between the layers (or if the barrier is tunneling-transparent), there can be no adjustment of the Landau levels in the neighboring layers on account of the voltage drop across the barrier. Then it is not the electron density in the well that is constant but rather the Fermi energy level relative to the well bottom. In this case, as the magnetic field varies, the electrons alternately escape from the well into the GaSb valence band and return back into the well as the Landau levels cross the Fermi level. On account of the high density of states in the valence band, the change in the carrier density accompanying interwell recombination results in a negligible relative change in the position of the Fermi level in the GaSb valence band and, correspondingly, in the InAs conduction band. Since the change in the Fermi energy is negligible against the background motion of the Landau levels of the electrons in the well, the Fermi level can taken as stationary.

The above-noted features in the dynamics of interlayer carrier transitions can account for the differences in the cyclotron resonance spectra. Cyclotron transitions in a system with a constant carrier density, as in samples 3 and 4, occur both from a partially filled level, which coincides with the Fermi level, and into this level (inset in Fig. 3a). If the nonparabolicity of the subband is large, as in the case of InAs, then splitting of the CR line can be observed. This splitting correlates with the position of the Fermi level: It exhibits features at integer-valued filling factors, which is observed for samples with 20 and 100 Å thick barriers (Fig. 3b). If the Fermi level is pinned, such splitting is very difficult to observe, since such transitions can occur only in a very narrow range of magnetic fields for which the Landau level passes through a stationary Fermi level. Indeed, the splitting of the CR line is of a different nature in the samples 1 and 2. In sample 1 an additional peak in sample 1 appears on the low-energy side of the CR line as the magnetic field increases. This cannot be explained by the nonparabolicity of the band. We prove below that the characteristic features observed in the CR spectra in samples 1 and 2 can be explained by the presence of a hybridization gap, formed as a result of mixing of electron and hole states, in the carrier spectrum.

A schematic diagram of the Landau levels of electrons and holes under conditions such that they are hybridized and cyclotron transitions leading to the observation of a hybridization gap are possible is shown in the inset in Fig. 2. Even though this scheme is qualitative, it can account for all the experimental results. First, the appearance of an additional peak in the CR spectrum is correlated with the broadening of the CR line and, correspondingly, it is associated with the anticrossing of electron and hole Landau levels, since the electronic CR line is broadened because of mixing of the states of high-mobility electrons with low-mobility holes as a result of their tunneling.[7] Second, the appearance of an additional peak in the CR spectrum (see Fig. 2, inset) depends on the position of the Fermi level relative to the hybridization gap. If the Fermi level lies inside the gap, then no additional peak will be present in the CR spectrum. If the Fermi level lies above (below) the hybridization gap, then an additional peak should appear on the low (high) energy side of the main CR line. In sample 1 an additional peak appears on the low-energy side, which suggests that in this case the Fermi level lies above the hybridization gap. In

sample 2 an additional peak is seen only after the sample is illuminated with a red LED. Since the illumination substantially decreases the electron density, such behavior agrees with a shift of the Fermi level as a result of illumination from a position inside the hybridization gap into a position below the gap. The third and strongest argument in favor of the interpretation of the observed splitting of the CR line as a hybridization gap is the agreement between the theoretical estimates of the hybridization gap width[3,8] and the energy splitting in a sample with no barriers. Moreover, measurements performed on two samples showed a substantial decrease in the gap width with increasing barrier thickness, in complete agreement with the expected change in the gap width with decreasing overlap of the wave functions. The energy splitting decreases from 3.5 to 1.3 meV as the barrier thickness increases from 0 to 6 Å .

It should be underscored that the diagram in the inset in Fig. 2 is of a qualitative character and does not reflect the real structure of the Landau levels. For example, the theoretical investigations in Ref. 4 showed that at the point of intersection the electron and hole Landau levels do not show pronounced anticrossing, but rather they are approximately parallel to one another. Indeed, as one can see from Fig. 2, the behavior of two CR modes near the anticrossing of the electron and hole Landau levels does not have the characteristic features typical of anticrossing.

In summary, in the present work we have made direct measurements of the energy gap formed as a result of the hybridization of states in binary electron–hole systems.

This work was supported by the Russian Fund for Fundamental Research.

*e-mail: Yu.Vasilyev@pop.ioffe.rssi.ru

[1] J. Kono *et al.*, Phys. Rev. B **50**, 12242 (1994); Phys. Rev. B **55**, 1617 (1997).
[2] R. J. Wagner *et al.*, Superlattices Microstruct. **21**, 95 (1997).
[3] M. Altarelli, Phys. Rev. B **28**, 842 (1983); A. Fasolino and M. Altarelli, Surf. Sci. **142**, 322 (1984); M. Altarelli *et al.*, Phys. Rev. B **35**, 9867 (1987).
[4] J.-C. Chiang *et al.*, Phys. Rev. Lett. **77**, 2053 (1996); S.-F. Tsay *et al.*, Phys. Rev. B **56**, 13242 (1997).
[5] M. J. Yang *et al.*, Phys. Rev. Lett. **78**, 4613 (1997).
[6] M. Lakrimi *et al.*, Phys. Rev. Lett. **79**, 3034 (1997).
[7] S. D. Suchalkin *et al.*, JETP Lett. **68**, 753 (1998).
[8] Y. Naveh and B. Laikhtman, Phys. Rev. Lett. **77**, 900 (1996).

Translated by M. E. Alferieff

Cherenkov trapping of waves and discreteness of 6π-kink motion in a long Josephson junction

A. S. Malishevskiĭ,[1)] V. P. Silin, and S. A. Uryupin
P. N. Lebedev Physics Institute, Russian Academy of Sciences, 117924 Moscow, Russia

(Submitted 14 January 1999; resubmitted 21 January 1999)
Pis'ma Zh. Éksp. Teor. Fiz. **69**, No. 4, 318–322 (25 February 1999)

The phenomenon of Cherenkov trapping of generalized Swihart waves by a moving vortex is established using an analytically solvable model. The quantization of the structure of the field of the trapped waves is manifested as quantization of the values of the velocity of the vortices.
© *1999 American Institute of Physics.* [S0021-3640(99)01204-9]

PACS numbers: 74.50.+r, 85.25.Cp

In the standard model description of vortices in steady-state motion in a long Josephson junction (JJ) on the basis of the nondissipative sine-Gordon equation, 6π kinks do not arise.[1] At the same time, experiments have long attracted theorists to search for multikink structures.[2] In this connection it is important to study vortices in a JJ on the basis of a theory in which the standard (for local Josephson electrodynamics) substitution of a delta function $\delta(z)$ for the Macdonald (modified Bessel) function $K_0(|z|/\lambda)$ is not made (see, for example, Ref. 3). The subject of the present letter is to take into account effects due to the finite value of the London length λ. An indication of the existence of a 6π kink in a JJ can be seen in the results of numerical investigations of a model with a ''sine'' nonlinearity, which, first, generalizes the sine-Gordon model by taking into account the fourth spatial derivative[4] and, second, takes into account the exact nonlocal kernel in the form of the Macdonald function $K_0(|z|/\lambda)$.[5] In those papers a monotonic 6π kink in steady-state motion with a definite velocity was obtained in Ref. 4, and, for a 6π kink depending monotonically on the coordinate, a plot of the velocity of the 6π kink as a function of λ was constructed in Ref. 5. In Ref. 5 the question of the existence of 6π kinks with a more complicated (nonmonotonic) structure was raised and left open. It is shown below that taking the finite value of λ into account, in the first place, yields a description of a set of 6π kinks in steady-state motion in a long JJ; in the second place, it makes it possible to show that the trapping of Cherenkov radiation by generalized Swihart waves plays a determining role; and, in the third place, it yields a relation between the discrete values of the kink velocity and, generally speaking, the nonmonotonic structure of 6π kinks.

We shall employ an equation for the phase difference of Cooper pairs on different sides of a JJ $\varphi(z,t)=\psi(z-vt)=\psi(\zeta)$ corresponding to a vortex structure traveling with constant velocity v[3,6,7]

 © 1999 American Institute of Physics

$$F(\psi)+\frac{v^2}{\omega_j^2}\frac{d^2\psi}{d\zeta^2}-\frac{l}{\pi}\frac{d}{d\zeta}\int_{-\infty}^{\infty}d\zeta' K_0\left(\frac{|\zeta-\zeta'|}{\lambda}\right)\frac{d\varphi}{d\zeta'}=0, \tag{1}$$

where ω_j is the Josephson frequency, $l=\lambda_j^2/\lambda$, and λ_j is the Josephson length. To establish the physical properties of 6π kinks, in contrast to Refs. 4 and 5, which employ $F(\psi)=\sin\psi$, we shall employ below the analytically solvable model of Refs. 8 and 9 and we shall assume that

$$F(\psi)=\psi(\zeta)-2\pi I\left[\frac{\psi(\zeta)}{2\pi}+\frac{1}{2}\right], \tag{2}$$

where $I[x]$ is the integer part of the number x. We note that such a dependence of the Josephson current density on the phase difference is possible at low temperatures (see Fig. 10 of Ref. 10).

Following the instructions given in Refs. 8 and 9 (see also Refs. 11 and 12), we take for the 6π kink: $\psi(-\infty)=0$, $\psi(-\zeta_1)=\pi$, $\psi(0)=3\pi$, $\psi(+\zeta_1)=5\pi$, $\psi(+\infty)=6\pi$. Then $I[(\psi/2\pi)+1/2]=\theta(\zeta+\zeta_1)+\theta(\zeta)+\theta(\zeta-\zeta_1)$, where $\theta(\zeta)=0$, $\zeta<0$; $\theta(0)=1/2$; $\theta(\zeta)=1$, $\zeta>0$. According to Refs. 8, 9, 11, and 12 Eq. (1) can be solved directly by Fourier transforming. We obtain

$$\begin{aligned}\psi(\zeta)=3\pi&+[\pi-f(\zeta+\zeta_1)]\operatorname{sign}(\zeta+\zeta_1)+[\pi-f(\zeta)]\operatorname{sign}\zeta\\&+[\pi-f(\zeta-\zeta_1)]\operatorname{sign}(\zeta-\zeta_1)+2C\{\cos[k_0(\zeta+\zeta_1)]\theta(-\zeta-\zeta_1)\\&+\cos[k_0\zeta]\theta(-\zeta)+\cos[k_0(\zeta-\zeta_1)]\theta(-\zeta+\zeta_1)\}.\end{aligned} \tag{3}$$

Here $\operatorname{sign}\zeta=+1$ for $\zeta>0$, 0 for $\zeta=0$, and -1 for $\zeta<0$, which corresponds to the properties of the Fourier transform, and

$$C=\frac{2(1+\lambda^2k_0^2)^{3/2}}{\lambda_j^2k_0^2[2(v/v_s)^2(1+\lambda^2k_0^2)^{3/2}-2-\lambda^2k_0^2]},$$

$$\begin{aligned}f(\zeta)=&\frac{2(1-\lambda^2k_1^2)^{3/2}\exp(-k_1|\zeta|)}{\lambda_j^2k_1^2[2-\lambda^2k_1^2-2(v/v_s)^2(1-\lambda^2k_1^2)^{3/2}]}\\&+\frac{2\lambda^2}{\lambda_j^2}\int_1^{\infty}\frac{drr\sqrt{r^2-1}\exp(-r|\zeta|/\lambda)}{r^4+(r^2-1)[(\lambda/\lambda_j)^2+(vr/v_s)^2]^2},\end{aligned}$$

where $v_s=\omega_j\lambda_j$ is the Swihart velocity. Finally, k_0 is the real root of the equation

$$\omega^2(k)=\omega_j^2[1+K(k)]\equiv\omega_j^2\left[1+\frac{lk^2}{\sqrt{k^2+\lambda^{-2}}}\right]=v^2k^2, \tag{4}$$

and k_1 is the modulus of the imaginary root of this equation. We underscore that Eq. (4) for real k is the condition for Cherenkov excitation of generalized Swihart waves with the spectrum $\omega(k)$ by a source moving uniformly with velocity v (see Refs. 13 and 14).

Bearing in mind the definition of the points $\zeta=0$ and $\zeta=\pm\zeta_1$ used above, we obtain from Eq. (3) the two conditions

$$\cos k_0\zeta_1 = -\frac{1}{2} \Rightarrow \zeta_1 = \pi\left(n+\frac{1}{2}+(-1)^n\frac{1}{6}\right)[k_0(v)]^{-1}, \quad n=0,1,2\ldots, \tag{5}$$

$$f(\zeta_1)+f(2\zeta_1)=C. \tag{6}$$

The last two equations determine a discrete spectrum $v(n)$ of velocities of 6π kinks and discrete values of $\zeta_1(n)$.

When Eq. (5) is taken into account, the term proportional to $2C$ in Eq. (3) assumes the form

$$C[Z_1(\zeta)\cos k_0\zeta+(-1)^n\sqrt{3}Z_2(\zeta)\sin k_0\zeta], \tag{7}$$

where $Z_1(\zeta)=-\theta(-\zeta-\zeta_1)+2\theta(-\zeta)-\theta(-\zeta+\zeta_1)$ and $Z_2(\zeta)=-\theta(-\zeta-\zeta_1)+\theta(-\zeta+\zeta_1)$. Expression (7) is nonzero in the region $-\zeta_1<\zeta<\zeta_1$. It describes the field of generalized Swihart waves emitted and trapped by a moving 6π kink. Both the size $2\zeta_1(n)$ of the trapping region and the wavelength $2\pi/k_0(v(n))$ of the trapped waves are determined by the number n of the corresponding mode of the 6π kink. The analytical relations obtained on the basis of Eqs. (5) and (6) for the motion of 6π kinks to a certain degree approximate the results of a numerical investigation of a discrete model,[15] which revealed the discreteness of the velocities of kinks in connection with their structure.

We shall now discuss some simple consequences of Eqs. (5) and (6). We shall assume that $\lambda \ll \lambda_j$. We examine first the case where the velocity v is close to the Swihart velocity, so that $\gamma^2=1-(v/v_s)^2 \ll 1$ and $k_0(v)=\lambda^{-1}[\gamma^2+\sqrt{\gamma^4+2\lambda^2/\lambda_j^2}]^{1/2}$ and $k_1(v)=\lambda^{-1}[-\gamma^2+\sqrt{\gamma^4+2\lambda^2/\lambda_j^2}]^{1/2}$. The equation (6) reduces to

$$x_n^2=\exp\left\{-2\pi\left(n+\frac{1}{2}+(-1)^n\frac{1}{6}\right)x_n\right\}+\exp\left\{-\pi\left(n+\frac{1}{2}+(-1)^n\frac{1}{6}\right)x_n\right\},$$

where $x_n \equiv k_1/k_0$. Correspondingly, we have for Eq. (3)

$$C=\frac{x_n^2}{1+x_n^2}, \quad k_0(v(n))=\frac{2^{1/4}}{\sqrt{x_n\lambda\lambda_j}}, \quad f_n(\zeta)=\frac{1}{1+x_n^2}\exp\left\{-|\zeta|\sqrt{\frac{\sqrt{2}x_n}{\lambda\lambda_j}}\right\}, \tag{8}$$

and for the discrete velocity $v(n)$ and width of the trapping region

$$\frac{v^2}{v_s^2}=\frac{v^2(n)}{v_s^2}=1-\frac{1-x_n^2}{\sqrt{2}x_n}\frac{\lambda}{\lambda_j}, \quad 2\zeta(n)=2^{3/4}\pi\left(n+\frac{1}{2}+(-1)^n\frac{1}{6}\right)\sqrt{x_n}\sqrt{\lambda\lambda_j}. \tag{9}$$

The characteristic scale of the spatial variation of the nonoscillatory part of the solution (3) is $\sim\sqrt{\lambda\lambda_j/x_n}$, and the period of the trapped waves is $\sim\sqrt{\lambda\lambda_j x_n}$. We have for the first few modes of a 6π kink $x_0=0.603$, $x_1=0.434$, $x_2=0.298$, $x_3=0.262$, $x_4=0.213$, and $x_5=0.196$ and for the high-order modes $(n\gg 1)x_n=(2\pi)[n+(1/2)+(-1)^n(1/6)]^{-1}\ln\{(\pi/2)[n+(1/2)+(-1)^n(1/6)]\}$. Therefore the trapping region for the high-order modes is large compared with the wavelength of the trapped waves.

In the limit of very high-order modes the velocity of a 6π kink differs substantially from v_s. We present the asymptotic results in the limit $n/\ln n \gg \lambda_j/\lambda$, so that $v \ll v_s$. Then $k_1=\lambda_j^{-1}$, $f(\zeta)=\exp(-|\zeta|/\lambda_j)$ and $C=2\lambda^2v^2(n)/\lambda_j^2v_s^2$. In this case

$$\frac{v^2}{v_s^2}=\frac{v^2(n)}{v_s^2}=\frac{\lambda_j}{\pi\lambda n}\ln\left(\frac{\pi\lambda_j n}{2\lambda}\right);\quad 2\zeta_1(n)=2\frac{\pi n\lambda v^2(n)}{v_s^2};\quad k_0(n)=\frac{1}{\lambda}\frac{v_s^2}{v^2(n)}. \quad (10)$$

As the mode number increases, the velocity of a 6π kink decreases, the wavelength $2\pi/k_0$ of the trapped waves decreases, and according to Eq. (10) the width $2\zeta_1(n)$ of the trapping region of the waves increases logarithmically. We note that the highest velocity of a freely moving 6π kink is given by Eq. (9) with $n=0$, i.e., $v_{\max}=v_s[1-0.746(\lambda/\lambda_j)]^{1/2}$.

With regard to the experimental realization of the predicted phenomenon of Cherenkov trapping of Swihart waves and the resulting discreteness of the motion of 6π kinks, we note first that the single condition we have imposed in this letter on the London and Josephson lengths has the form $\lambda\ll\lambda_j$ and is satisfied in JJs with critical Josephson current density less than 10^4 A/cm^2. Therefore the physical realization of our theoretical prediction is possible in most real JJs. However, for us it is important that the dynamics of vortices be determined by the capacitive and not the resistive influence in the JJ. This is our main condition. On this avenue of research there has been no significant progress in recent years for the case of a single long junction. We underscore that we are discussing the manifestation of nonlocality not in a pronounced nonlocal limit but rather in the standard limit for the electrodynamics of JJs, viz., for a characteristic scale of the nonuniformity of the vortex structures much greater than the London length. It is shown in this letter that under such conditions nonlocal electrodynamics is necessary for describing the short-wavelength excitations with wavelength greater than the London length but nonetheless very small compared with the Josephson length. The case of excitation and trapping of short-wavelength excitations which we considered comprises the fundamental essence of the phenomenon discussed in this letter. It is this advance of ours in the theory of moving Josephson vortices that is worth noting. Our new physical prediction of the trapping of Swihart waves is due to waves with wavelength $\sim\sqrt{\lambda\lambda_j}$, and the trapping region is distinct from the wavelength in terms of the number of trapped standing (but traveling together with the kink) waves that fit into it [see Eq. (7)].

We underscore once again that we are reporting in this letter the theoretical prediction of a new phenomenon due to short-wavelength excitations, emitted and trapped by vortices, that has not been studied for a long JJ. Nonlocal electrodynamics is required to describe such short-wavelength disturbances. However, the predicted phenomenon can be realized in standard Josephson junctions. According to Eq. (10) the large structure of a slowly moving vortex (moving with velocity much lower than the Swihart velocity) has a spatial scale $\sim\lambda_j$, and the wavelength of the Cherenkov-trapped waves is much shorter than the Josephson length.

We believe that our prediction can be realized by experimenters working with ordinary JJs. This refers both to the case of vortices traveling with velocities both close to and less than the Swihart velocity. The latter case requires a junction with low dissipation, both in the contact layer and due to the normal electrons in the superconductors. In this letter we are predicting a physical phenomenon that is ''in sight'' and will be discovered in ordinary JJs once the phenomenon attracts the attention of experimenters.

In closing, we underscore that the simple model of Refs. 8, 9, 11, and 12 has enabled us to establish the laws of discrete motion of 6π kinks in long dissipation-free JJs. We

have established the Cherenkov trapping of generalized Swihart waves moving together with a 6π kink. This phenomenon determines the form and velocity of the kink.

We shall report in a different journal the fact that this phenomenon determines the form and velocity of other types of kinks, for example, 4π and 8π kinks.

This work was supported by the Scientific Council on High-Temperature Superconductors (Project No. 99002), the Russian Fund for Fundamental Research, and the Government Program in Support of the Leading Scientific Schools (Project No. 96-15-96750).

[1)]e-mail: malish@sci.lebedev.ru

---

[1] A. Barone and G. Paterno, *Physics and Applications of the Josephson Effect*, Wiley, New York, 1982 [Russian translation, Mir, Moscow, 1984].
[2] B. Dueholm, O. A. Levring, J. Mygind *et al.*, Phys. Rev. Lett. **46**, 1299 (1981).
[3] Yu. M. Aliev and V. P. Silin, Zh. Éksp. Teor. Fiz. **104**, 2526 (1993) [JETP **77**, 142 (1993)].
[4] G. L. Alfimov, V. M. Eleonsky, N. E. Kulagin, and N. V. Mitzkevich, Chaos **3**, 405 (1993).
[5] G. L. Alfimov, V. M. Eleonsky, and L. M. Lerman, Chaos **8**, 257 (1998).
[6] I. O. Kulik and I. K. Yanson, *The Josephson Effect in Superconducting Tunneling Structures*, Coronet Books, 1971 [Russian original, Nauka, Moscow, 1970].
[7] A. Gurevich, Phys. Rev. B **46**, 3187 (1992).
[8] A. F. Volkov, Physica C **183**, 177 (1991).
[9] A. F. Volkov, Physica C **192**, 306 (1992).
[10] K. K. Likharev, Rev. Mod. Phys. **51**, 101 (1979).
[11] S. Aubry and P. J. Le Daeron, Physica D **7**, 240 (1983).
[12] S. Aubry, J. Phys. C **16**, 2497 (1983).
[13] R. G. Mints and I. B. Snapiro, Phys. Rev. B **52**, 9691 (1995).
[14] V. P. Silin and A. V. Studenov, Fiz. Tverd. Tela (St. Petersburg) **39**, 444 (1997) [Phys. Solid State **39**, 384 (1997)].
[15] M. Peyrard and M. D. Kruskal, Physica D **14**, 88 (1984).

Translated by M. E. Alferieff

Spin correlations and magnetonuclear cross-correlation in Sm(Sr)–Mn–O perovskites in the low-temperature phase

V. V. Runov,* G. P. Kopitsa, A. I. Okorokov, and M. K. Runova
St. Petersburg Institute of Nuclear Physics, Russian Academy of Sciences, 188350 Gatchina, Leningrad District, Russia

H. Glattli
SPEC, Saclay, CEA, France

(Submitted 26 January 1999)
Pis'ma Zh. Éksp. Teor. Fiz. **69**, No. 4, 323–328 (25 February 1999)

The results of measurements of spin correlations and magnetonuclear cross-correlations (MNCCs) in the system $^{154}Sm_{1-x}Sr_xMnO_3$ with the perovskite structure ($x=0.25,0.4$) in the low-temperature phase in magnetic fields $0<H<1$ kOe are presented. These are the first measurements performed by the small-angle polarized-neutron scattering method (SAPNS). It is shown that ferromagnetic correlations with a scale of 180–250 Å and MNCCs characterizing the intercoupling of the magnetic and lattice subsystems on this scale exist in the system. It is found that in the low-temperature phase the system exhibits spin-glass properties. © *1999 American Institute of Physics.*
[S0021-3640(99)01304-3]

PACS numbers: 75.50.Lk, 75.30.Vn, 61.12.Ex

Interest in the systems $(R^{3+}_{1-x}A^{2+}_x)MnO_3$ with the perovskite structure has increased in recent years in connection with the presence of colossal negative magnetoresistance (CMR) in these materials near the magnetic phase transition temperature and the possibility of technical applications of this phenomenon. Investigators have always called attention to the magnetic inhomogeneity of these systems (apparently first in Ref. 1) and have conjectured that magnetic inhomogeneities are an inherent and fundamental feature of these materials and give rise to the CMR (see, e.g., the review by Nagaev[2] and the paper by Goodenough and Zhou[3]). In recent years this has led to a growing number of investigations on small-angle neutron scattering in search of magnetic inhomogeneities due to phase separation according to the electrical conductivity, primarily, in La perovskites.[4–6]

In the present letter we report investigations of spin correlations and magnetonuclear cross-correlations (MNCCs) in the system $^{154}Sm_{1-x}Sr_xMnO_3$ by small-angle polarized-neutron scattering (SAPNS), which makes it possible to perform measurements of the magnetonuclear interference (MNI). The latter, in our view, is the most important advantage of using polarized neutrons to investigate systems with CMR, since it presents the experimental possibility of studying the intercoupling of the magnetic and lattice sub-

 © 1999 American Institute of Physics

systems on a scale of 10–1000 Å . The interference term, which is proportional to the product of the nuclear and magnetic scattering amplitudes, can be identified by analyzing the difference of the intensities of scattered neutrons polarized parallel and antiparallel to the magnetization vector of the sample. As was shown in Refs. 7 and 8, interference analysis makes it possible to study very weak magnetic effects (correspondingly, nuclear effects) in the presence of a dominant nuclear or magnetic term.

In the present letter it is shown that ferromagnetic correlations with a scale of 180–250 Å and MNCCs of the same scale exist in the Sm system at low temperatures. The intercoupling of the magnetic and lattice subsystems on this scale must be taken into account in the interpretation of the electronic and transport properties of the system.

1. Description of the experiment. The SAPNS measurements on the Sm system were performed using the small-angle polarized-neutron scattering setups Vektor[9] (VVRM-M reactor, Gatchina) and PAPOL[10] (LLB, Saclay, France). The Vektor setup has a working wavelength $\lambda = 9.2$ Å and $\Delta\lambda/\lambda = 0.25$; it is equipped with a multichannel analyzer, which makes it possible to measure the scattering and to perform a complete polarization analysis in the range of scattering wave numbers $0 < q < 3 \times 10^{-1}$ Å^{-1} in a slit geometry ($\mathbf{q} = \mathbf{k} - \mathbf{k}'$, where $\mathbf{k}$ and $\mathbf{k}'$ are the wave vectors of the incident and scattered neutrons, respectively); a sample with $x = 0.25$ was investigated in the temperature range $16 < T \leqslant 300$ K in magnetic fields $0 < H_z < 150$ Oe (the z axis is directed parallel to $\mathbf{k}$). For the PAPOL setup $\lambda = 8$ Å and $\Delta\lambda/\lambda = 0.1$; the neutron scattering is measured in a point geometry with the scattering detected with an X–Y detector; a sample with $x = 0.4$ was investigated at temperatures $T = 12.5$, 53, 85, 100, 150, and 300 K in magnetic fields $H_z \leqslant 1$ kOe. The measurements were performed in Displex (PAPOL) and RNK-100-300 (Vektor) cryorefrigerators with temperature stabilization $\simeq 0.1$ K. The samples were placed in an atmosphere of helium gas, which was used as the heat-transfer gas.

We studied powder samples of $^{154}Sm_{1-x}Sr_xMnO_3$ completely enriched with ^{154}Sm. The samples, with dimensions of 8×45 mm by 2 mm thick, were synthesized by ceramic technology. The grain size was 5–10 μm. The results of the structural investigations by neutron diffraction, and the investigations of the magnetic and transport properties of these samples are presented in Ref. 11. The neutron-diffraction measurements established that the system possesses a distorted perovskite structure. Refinement of the structural parameters showed that the sample with $x = 0.25$ is described better by a monoclinic structure ($P112_1/a, N14$), while for $x = 0.4$ an orthorhombic structure ($Pnma, N62$) gives a better description. According to the magnetic and neutron diffraction measurements, a transition into the magnetically ordered phase at $T = 110$–130 K is observed in the $x = 0.4$ sample and rapid growth of the magnetic susceptibility at $T = 90$–100 K, attesting to a change in the magnetic ordering, is observed in the $x = 0.25$ sample. Substantial broadening of the diffraction peaks was noted in Ref. 11. This broadening could be due to small nuclear or magnetic formations which are compared with the grain size. According to the data on the temperature dependences of the resistivity, the $x = 0.25$ sample does not transform into the ''metallic'' state at low temperatures, in contrast to the $x = 0.4$ sample in which a change in the type of conductivity to ''metallic'' is observed at $T \leqslant 125$ K. The magnetic and electric properties of the experimental samples correlate well with the properties of the Sm system described in Ref. 12.

2. Results of SAPNS measurements and discussion. Figure 1 shows the typical

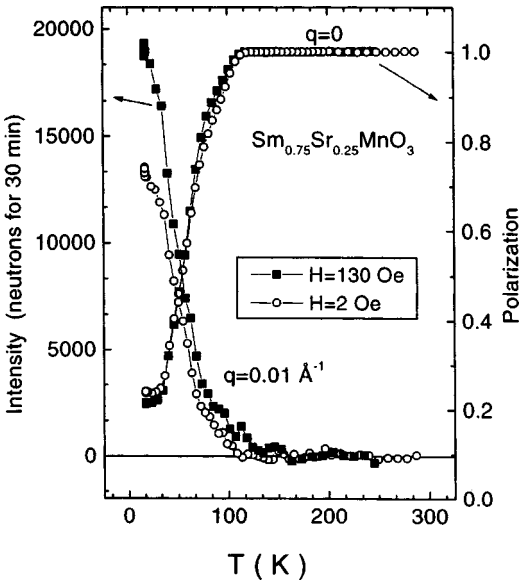

FIG. 1. Temperature dependence of the polarization and intensity of scattered neutrons in the sample $^{154}Sm_{0.75}Sr_{0.25}MnO_3$.

temperature dependence of the scattering intensity $I(T)$ and polarization $P(T)$ in the $x=0.25$ sample in the measured range of q for a weak guiding magnetic field $H\approx 2$ Oe, which ensures adiabatic motion of the polarization vector, and a field $H_z=130$ Oe. The background, for which measurements at $T=300$ K were used, was subtracted from the intensities $I(T)$. As one can see from Fig. 1, the transition starts at $T\simeq 115$ K (onset of variation of $P(T)$ and $I(T)$) and is extended in temperature. The magnetic field $H_z=130$ Oe does not promote homogenization of the system, as happens in magnetically soft materials,[13] but rather intensifies the inhomogeneity of the system. Moreover, as the temperature decreases, the polarization does not drop to zero but rather reaches a certain minimum level. At the same time, estimates show that when ferromagnetic ordering appears on the scale of a grain the polarization with $H\approx 0$ should equal zero for a given sample thickness.

Analysis of the dependences $I(q)$ at temperatures $T<115$ K showed that they are described well by the quadratic Lorentzian

$$I(q)=\frac{A}{(q^2+\kappa^2)^2}, \tag{1}$$

where A and $\kappa=1/R_c$ are free parameters and R_c is a characteristic correlation radius. In the coordinate representation the function (1) corresponds to scattering by the correlator of the spins S_i and S_j that decays exponentially with distance r

$$\langle S_i S_j\rangle \propto \exp(-r/R)_c. \tag{2}$$

The values of the parameters A and R_c obtained as the convolution of expression (1) with the resolution function of the setup are shown in Fig. 2. The figure also displays the

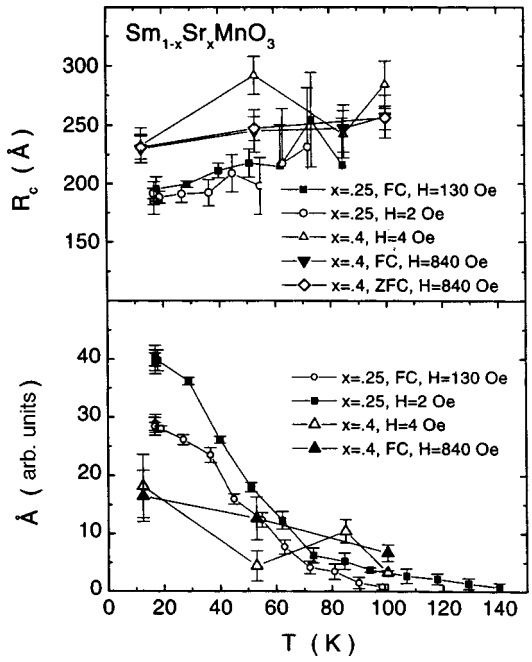

FIG. 2. Temperature dependence of the correlation radius R_c and the parameter A in Eq. (1) in the system $^{154}Sm_{1-x}Sr_xMnO_3$ under various measurement conditions.

values of the parameters for the $x=0.4$ sample for various measurement conditions. The scattering by this sample is likewise satisfactorily described by expression (1) at temperatures $T<130$ K.

Figures 3–5 shows the difference $\Delta I(q)=I^+(q)-I^-(q)$ of the scattering intensity for neutrons polarized parallel $(+)$ or antiparallel $(-)$ to the magnetic field as a function of T and H and the conditions of cooling of the sample (ZFC — cooling in a zero guiding magnetic field followed by the switching on of a field H, and FC — cooling and measurement in a field H). The typical three-dimensional plot of $\Delta I(q)$ is displayed in Fig. 3. Figure 5 displays data averaged over the radius with $q=$ const in the detector plane. In the experiment the relative magnitude $\Delta I/(I^+ + I^-)$ is of the order of 1%. As was shown in Ref. 7, $\Delta I(q)$ is proportional to two terms

$$\Delta I \propto 2\,\mathrm{Re}[\langle \psi_0 \psi^*{}_m \rangle + \langle \psi_n \psi^*{}_m \rangle], \tag{3}$$

$$\int \Delta I(q)\,dq = 0. \tag{4}$$

The condition (4) follows from the optical theorem. The first term in Eq. (3) corresponds to interference of the direct beam and magnetic scattering, while the second term corresponds to interference of the nuclear and magnetic scattering (ψ_0, ψ_n, and ψ_m are the wave functions of the neutrons that have not undergone scattering, the neutrons that have been scattered by the nuclear potential, and the neutrons that have been scattered by the magnetic potential, the sign of which depends on the orientation of the neutron polariza-

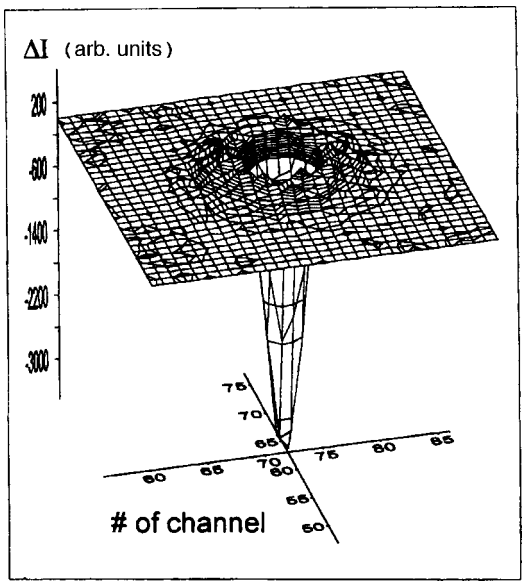

FIG. 3. Three-dimensional representation of $\Delta I(q)=I^{+}(q)-I^{-}(q)$ in a $^{154}Sm_{0.6}Sr_{0.4}MnO_3$ sample at $T=85$ K and $H=140$ Oe. The measurements were performed in the PAPOL setup with a position-sensitive X–Y detector with 128×128 channels. One detector channel corresponds to $q\approx0.001$ Å^{-1}.

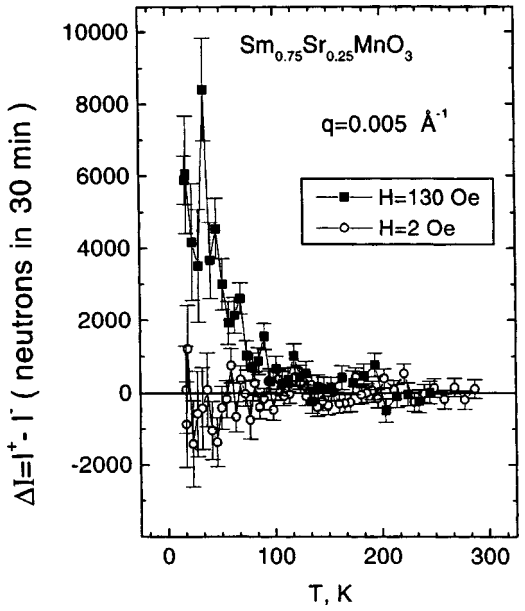

FIG. 4. Temperature dependence of $\Delta I(q)=I^{+}(q)-I^{-}(q)$ in a $^{154}Sm_{0.75}Sr_{0.25}MnO_3$ sample under different measurement conditions. The data are normalized to the polarization of the transmitted neutron beam.

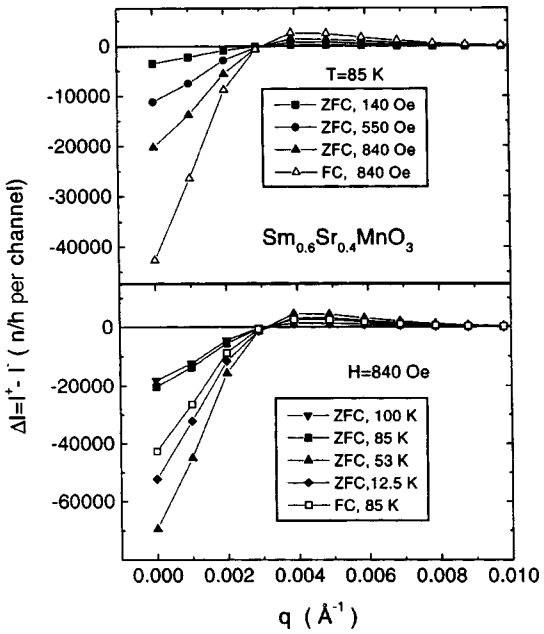

FIG. 5. Momentum dependence $\Delta I(q)=I^{+}(q)-I^{-}(q)$ (in units of neutrons per hour per channel) in a $^{154}Sm_{0.6}Sr_{0.4}MnO_3$ sample under various measurement conditions. The data are normalized to the polarization of the transmitted neutron beam.

tion relative to the field). It follows from Eq. (4) that the terms in expression (3) should have different signs, which is seen in the experiment (Figs. 3 and 5) as a different sign of $\Delta I(q)$ in the range $q<q_{\min}$ (i.e., in the region of the direct beam, where $q_{\min}$ is the limiting momentum resolution of the setup) and in the range $q>q_{\min}$ (in the region where scattering predominates).[7] It follows from the observation of a change in sign that the resolution of the setup makes it possible to distinguish scattering by MNCCs from the direct beam. This gives the upper limit on the characteristic correlation radius detected in the experiment: $R_{mn}\leqslant R_{\max}$, where $R_{\max}\approx 1/q_{\min}$, the limiting resolution of the setup. In the present experiment $R_{\max}\sim 400$ Å.

The magnetonuclear cross-correlation function $G_{mn}(\mathbf{r})$ can be written[7,14] as

$$G_{mn}(\mathbf{r})=\frac{1}{V}\int (\rho_m(\mathbf{r}')-\overline{\rho_m})(\rho_n(\mathbf{r}+r')-\overline{\rho_n})d\mathbf{r}', \tag{5}$$

where V is the sample volume and ρ_m and ρ_n are the magnetic and nuclear scattering length densities, respectively; ΔI_{mn}, due to MNI (second term in Eq. (3)), corresponds to the Fourier transform of $G_{mn}(\mathbf{r})$. Further analysis requires a model and measurements with a good data sample of $\Delta I(q)$ in order to distinguish and describe ΔI_{mn} (Ref. 7). In the present letter we confine our attention to estimates and qualitative conclusions. As one can see from Figs. 3–5, the interference effect is observed well in the low-temperature phase for both samples. It increases with the magnetic field and, on the

whole, with decreasing T. Moreover, it depends on the method of cooling — ZFC or FC. According to Eq. (5), the observed sign of ΔI_{mn} corresponds to a change of the magnetic and nuclear densities that is in-phase with respect to the sign.[7,14]

On the whole, the magnetic state of the Sm system with $x=0.25$ at temperatures $T<115$ K can evidently be characterized as an unsaturated ferromagnet in which ferromagnetic fluctuations of the form (2) are developed. The density of such fluctuations is proportional to the parameter A and increases quite strongly as T decreases, while the radius R_c most likely decreases somewhat with decreasing T (Fig. 2). This is also true of the $x=0.4$ sample, which, according to the neutron diffraction measurements, exhibits long-range magnetic order, apparently of the percolation type. The radius R_c in it is greater than for the $x=0.25$ sample, and the concentration does not depend as strongly on T. The MNI observed in the samples indicates a quite strong intercoupling of the magnetic and lattice subsystems on the scale $\sim R_c$. Rough estimates (estimates according to the minimum) show that to explain the observed interference in the $x=0.25$ sample the relative change in the density of the nuclear amplitude in synchronization with the magnetic amplitude in the correlated regions should be greater than 1%. (In making this estimate it was assumed that the size of the correlated regions $\sim R_c$, $\Delta I_{mn}\sim 4(\rho_m-\overline{\rho_m})(\rho_n-\overline{\rho_n}), I_m\propto(\rho_m-\overline{\rho_m})^2$, and $I_n(T=300\ \mathrm{K})\propto(\overline{\rho_n})^2$.) The statistical accuracy obtained for the correlation parameters (Fig. 2) does not permit analyzing them as a function of the cooling regimes (ZFC–FC), but a dependence on the magnetic history of the sample is observed in $\Delta I(q)$, and there is noticeable hysteresis in $P(T)$ for the $x=0.25$ sample, as is typical for spin-glass systems.[15] Our overall estimate of the low-temperature magnetic state of the Sm system agrees with the magnetic and neutron diffraction measurements, in which broadening of the diffraction peaks was observed.[11] However, to explain the magnetic properties of the experimental and similar systems and to understand the intercoupling of the magnetic and lattice subsystems, further investigations of the magnetic correlations in both Sm samples and other perovskites, preferably, in poly- or single-crystalline samples are required.

We thank V. A. Trunov for discussions and for kindly providing the samples, S. M. Dunaevskiĭ and D. Yu. Chernyshov for helpful discussions, and S. V. Grigor'ev and S. A. Klimko for assisting in the measurements and for discussions.

This work was supported by Russian Fund for Fundamental Research (Projects Nos. 98-02-17632 and L-EN-96-15-96775) and by the Government Scientific and Technical Program ''Neutron Studies of Condensed Matter.''

*e-mail: runov@hep486.pnpi.spb.ru

[1] E. O. Wollan and W. C. Koehler, Phys. Rev. **100**, 545 (1955).
[2] É. L. Nagaev, Usp. Fiz. Nauk **166**, 833 (1996).
[3] J. B. Goodenough and J. S. Zhou, Nature (London) **386**, 229 (1997).
[4] J. M. De Teresa, M. R. Ibarra, P. A. Algarabel *et al.*, Nature (London) **386**, 256 (1997).
[5] C. Ritter, M. R. Ibarra, J. M. De Teresa *et al.*, Phys. Rev. B **56**, 8902 (1997).
[6] M. Viret, H. Glattli, C. Fermon *et al.*, Europhys. Lett. **42**, 301 (1998); Physica B **241–243**, 430 (1998).
[7] G. Gordeyev, A. Okorokov, V. Runov *et al.*, Physica B **234–236**, 837 (1997); in *Proceedings of the International Seminar ''PNCMI-96,''* Dubna, June 18–20, 1996, p. 65.
[8] G. P. Kopitsa, V. V. Runov, and A. I. Okorokov, Fiz. Tverd. Tela (St. Petersburg) **40**, 23 (1998) [Phys. Solid State **40**, 19 (1998)].

[9] S. V. Grigor'ev, O. A. Gubin, G. P. Kopitsa *et al.*, Preprint PIYaF–2028 [in Russian], Gatchina, 1995.
[10] M. G. D. Van der Grinten, H. Glattli, and M. Pinot, Neutron News **6**, 18 (1995).
[11] S. M. Dunaevskiĭ, A. I. Kurbakov, V. A. Trunov *et al.*, Fiz. Tverd. Tela (St. Petersburg) **40**, 1271 (1998) [Phys. Solid State **40**, 1158 (1998)].
[12] F. Damay, N. Nguen, A. Maignan *et al.*, Solid State Commun. **98**, 997 (1996).
[13] A. I. Okorokov, A. G. Gukasov, V. V. Runov *et al.*, Zh. Éksp. Teor. Fiz. **81**,1462 (1981) [Sov. Phys. JETP **54**, 775 (1981)].
[14] S. Komura, T. Takeda, and Y. Endoh, J. Magn. Magn. Mater. **50**, 69 (1985).
[15] V. V. Runov, S. L. Ginzburg, B. P. Toperverg *et al.*, Zh. Éksp. Teor. Fiz. **94**, 325 (1988) [Sov. Phys. JETP **67**, 181 (1988)].

Translated by M. E. Alferieff

Comment on the paper ''Ground state instability in systems of strongly interacting fermions''

V. A. Khodel'
Kurchatov Institute Russian Science Center, 123182 Moscow, Russia

(Submitted 10 January 1999)
Pis'ma Zh. Éksp. Teor. Fiz. **69**, No. 4, 329–330 (25 February 1999)
[S0021-3640(99)01404-8]
PACS numbers: 05.30.Fk, 71.10.Ca

In a recent article by Artamonov, Pogorelov, and Shaginyan,[1] the restructuring of the quasiparticle distribution $n_{\mathbf{p}}$ at temperature $T=0$ was studied for the model ''Hartree–Fock'' energy functional

$$E(n_{\mathbf{p}})=\sum_{\mathbf{p}} \epsilon^0_{\mathbf{p}} n_{\mathbf{p}} + 1/2 \sum_{\mathbf{p}_1,\mathbf{p}_2} V(\mathbf{p}_1-\mathbf{p}_2) n_{\mathbf{p}_1} n_{\mathbf{p}_2}.$$

Fermion condensation (FC) — a phase transition associated with the nontrivial solutions of the equation of the minimum $\delta E/\delta n_{\mathbf{p}}=\mu$, where μ is the chemical potential, was also considered. The authors stated that when the operator V and all of its derivatives are continuous, solutions of the the equation of the minimum, having the form

$$\phi(\mathbf{p})=\int V(\mathbf{p}-\mathbf{p}_1) n_{\mathbf{p}_1} d\tau_1, \quad p_i<p<p_f, \tag{1}$$

where $\phi=\mu-\epsilon^0_{\mathbf{p}}$, do not exist, and therefore fermion condensation is forbidden. If their arguments were correct, the entire field of modern mathematics concerning the so-called ill-posed problems (see, for example, Ref. 2) would be closed. For this reason, the situation requires comment.

Equation (1) (written symbolically as $\phi=Vf$) is an example of the inverse-scattering problem, which is encountered in different fields of physics. For example, if p is a coordinate and n_p a density, then Eq. (1) is the equation of equilibrium of a system of particles with the interaction potential $V(r)$ in an external electric (or gravitational) field.

In all known models of fermion condensation the interaction V is singular, the inverse operator V^{-1} exists, and the solution of the inverse-scattering problem $f=V^{-1}\phi$ is stable against small perturbations. In the paper addressed here the operator V is completely continuous (i.e., the operator V^{-1} is singular!). The authors give the following arguments. The integral Vf and the function ϕ are identical on the segment $[p_i,p_f]$ if f is an exact solution of Eq. (1). If this is so, then by virtue of the continuity of V and its derivatives, the left and right sides of Eq. (1) must coincide on the entire straight line. But this is impossible, since the function $\phi\sim\epsilon^0_{\mathbf{p}}\sim p^2$ diverges as $p\to\infty$, while the integral Vf remains finite. Therefore solutions of Eq. (1) do not exist at all, and there is

 © 1999 American Institute of Physics

no fermion condensation. We note that by this token not only is fermion condensation impossible but, for example, the equilibrium of a nucleus in the field of an electronic shell is also impossible — after all, according to gauge theories a nucleon is an extended object and therefore the nucleon–nucleon potential $V(r)$ in Eq. (1) is completely continuous.

In reality the situation is completely different. Since the inverse operator V^{-1} is singular, the computed solutions of Eq. (1) are unstable against small perturbations. They are ''filled with noise.'' These components change sign and amplitude chaotically and therefore do not correspond to any physical reality — physical reality is described by quite smooth functions, because nature knows how to suppress noise. One noise suppression mechanism is this: In a real system there always exist fluctuations. Being a functional of $n_{\mathbf{p}}$, the interaction V also fluctuates — from one sample to another, from one experiment to another. These comparatively small variations of V fundamentally reshape the noise distribution without influencing the smooth components of the solutions. On averaging over the fluctuations of V, the noise in f is suppressed while the smooth component (called the quasisolution[2]) remains unchanged. On the segment under study the quasisolutions reproduce the left side of Eq. (1) with an error that is on the scale of the amplitude of the fluctuations in V, but outside this segment the discrepancy increases rapidly. In the fermion condensation problem, a smooth quasisolution describes the fermion condensate, provided, of course, that the Pauli principle $n_p<1$ is not violated. This is feasible if the coupling constant is sufficiently large.

To summarize, I think that in the near future the fermion condensate will be found even in the specific model with $V(p)\sim(p^2+p_0^2)^{-1}$, where in the opinion of the authors of Ref. 1 there can be no such states.

[1] S. A. Artamonov, Yu. G. Pogorelov, and V. R. Shaginyan, JETP Lett. **68**, 942 (1998).
[2] A. N. Tikhonov and V. Ya. Arsenin, *Solutions of Ill-Posed Problems*, Halsted Press, New York, 1977 [Russian original, Nauka, Moscow, 1974].

Translated by M. E. Alferieff

Reply to the comment by V. A. Khodel'

S. A. Artamonov, Yu. G. Pogorelov, and V. R. Shaginyan
St. Petersburg Institute of Nuclear Physics, Russian Academy of Sciences, 188350 Gatchina, Leningrad Region, Russia

(Submitted 20 January 1999)
Pis'ma Zh. Éksp. Teor. Fiz. **69**, No. 4, 331–332 (25 February 1999)

[S0021-3640(99)01504-2]

PACS numbers: 05.30.Fk, 71.10.Ca

In our article[1] commented on by V. A. Khodel', we showed for the example of a model energy functional that in certain cases there is no Fermi-condensate state. We shall discuss here a mathematical aspect of this question, following Ref. 1. For the reader's convenience we shall employ notations used in the comment, which are different from those adopted in our paper. Let us consider the equation

$$\phi(p)=\int V(p,p_1)n_{p1}p_1^2dp_1, \tag{1}$$

where $\phi=\mu-\varepsilon_p^0$, with μ being the chemical potential. In our case the kernel $V(p,p_1)$ is a symmetric analytic function of its two arguments in a strip Ω of finite width along the real axis of the complex momentum P plane. The kernel of Eq. (1) is positive-definite, $V(p,p_1)>0$, and acts on functions $0\leqslant n_p\leqslant 1$. It is easy to see that under these conditions the right-hand side of Eq. (1) is zero only if $n_p\equiv 0$, whence it follows that the equation

$$0=\int V(p,p_1)n_{p1}p_1^2dp_1 \tag{2}$$

does not have nontrivial solutions. Therefore Eq. (1) possesses a nonsingular inverse operator. This is not surprising: Eq. (1) is an example of an integral equation of the first kind, a class of equations which are closely related to integral transforms, e.g., the Fourier transform. As is well known, these transforms are given by nonsingular direct and inverse operators. The functions ϕ are representable in terms of the kernel V. Since the integration in Eq. (1) is over a finite interval and n_p possesses only a finite number of discontinuities, the functions ϕ, which are representable in terms of the kernel, are analytic functions in Ω and cannot be constant (just as any derivative of ϕ) in a finite interval, provided, of course, that the kernel is not constant, as is the case for the kernel studied in Ref. 1. However, the function describing a Fermi-condensate state certainly includes a region where ϕ (or some derivative of ϕ) is constant. We can now conclude that Eq. (1) does not admit Fermi-condensate states or, equivalently, the solutions can only be functions constructed from Fermi steps: $n_p=1.0$. We note that it does not at all follow hence that Eq. (1) does not have solutions that are stable against small disturbances: In Ref. 1 these solutions were found and determined to correspond to topological phase transitions. In truth, the class of these solutions is relatively sparse, but it should be

 © 1999 American Institute of Physics

kept in mind that we seek solutions satisfying the Pauli principle and corresponding to minimum energy. For example, we note that under these strict conditions Eq. (1) is not a linear equation: If n_p is a solution, then after it is multiplied by a constant it is no longer a solution.

It is *apropos* to recall that in Ref. 1 we underscored that the single-particle quasiparticle potential in a real system cannot be an analytic function, i.e., the right-hand side of Eq. (1) will not be an analytic function if V is a real effective interaction. Therefore in a real system the topological phase transitions will be ''absorbed'' by a Fermi-condensate transition. We have replied to all the remarks made in the omment, and we affirm the correctness of the results obtained in our paper.[1]

[1] S. A. Artamonov, Yu. G. Pogorelov, and V. R. Shaginyan, JETP Lett. **68**, 942 (1998).

Translated by M. E. Alferieff